

RICHTMYER-MESHKOV INSTABILITY WITH RESHOCK AND PARTICLE INTERACTIONS

A Thesis
Presented to
The Academic Faculty

by

Satoshi Ukai

In Partial Fulfillment
of the Requirements for the Degree
Master of Science in the
School of Aerospace Engineering

Georgia Institute of Technology
August 2010

RICHTMYER-MESHKOV INSTABILITY WITH RESHOCK AND PARTICLE INTERACTIONS

Approved by:

Professor Suresh Menon, Committee Chair
School of Aerospace Engineering
Georgia Institute of Technology

Professor Vigor Yang
School of Aerospace Engineering
Georgia Institute of Technology

Professor Lakshmi Sankar
School of Aerospace Engineering
Georgia Institute of Technology

Date Approved: June 25, 2010

ACKNOWLEDGEMENTS

I would like to express my gratitude to Prof. Suresh Menon for his dedicated support for the past three years. He provided opportunities to study various types of problems that I did not know anything about and trained me to think as a researcher. I appreciate his help and advice toward my MS degree. I would also like to thank the other members of my thesis committee, Prof. Vigor Yang and Prof. Lakshmi Sankar for the suggestions, comments and the critical examinations of my thesis.

I thank the Defense Threat Reduction Agency (DTRA) for the financial support. It was a great experience to attend the sponsor meeting as well.

The working environment and the members of the Computational Combustion Lab (CCL) are extraordinary. I especially would like to acknowledge, Dr. Franklin Génin, Dr. Kenji Miki, Dr. Baris Sen, Dr. Jung Choi, Dr. Srikant Srinivasan, Matthieu Masquelet and Kaushik Balakrishnan. I would not have been able to carry out my research without their support. I also thank Leandro Gryngartem, Engin Orcun Kozaka, Andy Smith, Kanlyana Gottiparthi, Bassem Girgis and Alpha Bah. I appreciate our time spent working day and night together in the CCL.

Finally, I appreciate my parents and sister for their support and understanding. They continually encourage me to pursue my dream.

TABLE OF CONTENTS

ACKNOWLEDGEMENTS	iii
LIST OF TABLES	vi
LIST OF FIGURES	vii
SUMMARY	ix
I INTRODUCTION	1
1.1 Review of RMI growth models	3
1.1.1 Single-mode RMI	3
1.1.2 Multi-mode RMI	4
1.1.3 Reshock RMI models	5
1.2 Multiphase RMI	8
1.2.1 Effect of particles on instabilities	8
1.2.2 Instabilities of a particle cloud	9
1.3 Objectives	10
1.4 Outline	11
II MATHEMATICAL FORMULATION AND MODELING	13
2.1 The Navier-Stokes Equations	13
2.2 Particle Tracking - Lagrangian Scheme	16
III NUMERICAL METHODS	18
3.1 Discretization of the governing equations	19
3.1.1 Finite volume method	19
3.1.2 Domain discretizations	21
3.1.3 Time Integration - McCormack scheme	21
3.2 Central Schemes	22
3.3 Flux-difference splitting method	23
3.3.1 MUSCL interface reconstruction	24
3.3.2 Riemann solvers	26

3.4	Switching criteria	32
3.5	Boundary conditions	33
3.6	Particle tracking	34
IV	RESHOCKED RICHTMYER-MESHKOV INSTABILITY	35
4.1	Simulation of Experimental Setups	35
4.2	Parametric Studies of Single-Mode RMI	42
4.3	Parametric Studies of Multi-Mode RMI	48
4.4	Conclusions of Reshocked RMI studies	53
V	MULTIPHASE RICHTMYER-MESHKOV INSTABILITY	57
5.1	Amplitude Growth Model of Multiphase RMI	57
5.2	Results	63
5.2.1	Results for Air/SF ₆ interface surrounded by particles	63
5.2.2	Results for perturbed shape particle cloud	73
5.3	Conclusions of Multiphase RMI studies	78
VI	CONCLUSIONS AND RECOMMENDATIONS	80
6.1	Conclusion	80
6.2	Recommendations for future work	82
	REFERENCES	84

LIST OF TABLES

1	List of existing reshock models.	7
2	List of order of accuracy of MUSCL scheme	24
3	List of parameters used to construct species interface perturbations. .	37
4	List of coefficients for Sadot-type models.	40
5	Growth rates before and after reshock, and model coefficients for each case. C and β are coefficients found from the formulations of Mikaelian's reshock model (Eqn. 5) and Charakhch'an's model (Eqn. 6), respectively, where $\Delta V_2 = 92.5$ m/s and $A^+ = 0.71$	42
6	Cases simulated for 2D and 3D single-mode RMI.	43
7	2D single-mode RMI for different a_r and λ	44
8	2D and 3D single-mode RMI with different incident Mach numbers. .	45
9	List of initial conditions and results for the 2D and 3D multi-mode RMI.	50
10	The empirical values for the Mikaelian's reshock model (C) extended for different interface configurations. Note that original model used $C = 0.28$ [62], and recent experimental study showed $C = 0.38$ for 3D multi-mode RMI [48]	56
11	List of parameters for the first study.	65
12	Results of growth rate obtained from the numerical simulation and theoretical models. Stokes number, St is computed based on the initial growth rate obtained from the numerical results, $v_{0,num}$. Thus, $St_1 = kv_{0,num}\tau_1$	66
13	Parameters and results of each case for the second kind of multiphase RMI. The results of Case P4.0-X and P8.0-X are not listed because the acceleration of the particles for these cases is not impulsive due to the high inertia of the particles, and ΔV could not be determined for the same reason.	74

LIST OF FIGURES

1	Bubble and spike definition for a RMI perturbation. The gray and white regions correspond to the heavy and light species, respectively.	2
2	Vorticity deposition over a species interface with heavy-light (left) and light-heavy (right) configurations.	2
3	The comparison of particle dispersion and deformation of SF_6 by shock.	9
4	HLLC configuration of the different waves at cell interfaces	27
5	HLLC configuration	28
6	Schematic of the RMI test configuration. For reshock, the shock reflects from the right wall and exits from the left.	36
7	Differences in the mixing layer estimate by different methods.	38
8	Grid sensitivity of single- and multi-mode RMI in 2D and 3D.	39
9	Comparison with the 2D RMI growth rate models.	41
10	Comparison with the 3D RMI growth rate models.	41
11	Comparisons of growth for each case. The straight-line represents the experimental slope of 23.1 m/s [48].	42
12	Mixing length growth with different initial geometries.	44
13	Amplitude of 2D RMI with different incident Mach numbers.	45
14	Correlation between mixing length growth rate and ΔV_2 . The regression line shows that the slope is 0.39 in 2D and 0.60 in 3D.	46
15	RMI interface shape colored by mass fraction of SF_6 (Case S2).	47
16	RMI interface shapes colored by mass fraction of SF_6	48
17	Iso-surfaces of species interface with different mass fractions of SF_6 (Blue-10%, Green-50%, Orange-90%).	49
18	Mixing length growth of 2D (a) and 3D (b) multi-mode RMI with different initial conditions.	52
19	Side view of interface evolution. Top - Case M2, Bottom - Case M4.	54
20	Side view of interface with different mass fraction of SF_6 (Blue-10%, Green-50%, Orange-90%). Top - Case 3DM7, Bottom - Case 3DM5.	55
21	Initial configuration of Rayleigh-Taylor instability. Specie 2 (heavy gas) is on the top of species 1 (light gas) to initiate the instability . . .	58

22	Initial configuration of RMI in a perturbed species interface surrounded by a cloud of solid particles. The grey region denotes the region filled with the gas-particle mixture.	64
23	Comparison of the effect of the assigned number of parcels to the amplitude growth. ‘64 Grid’ and ‘128 Grid’ corresponds to the grid size in the y -direction. The legend ‘64 Parcel’ indicates the case with 64 parcels initialized in the y -direction (i.e., initially one parcel per cell), and ‘128 Parcel’ uses 128 parcels in the y -direction, with the distance between parcels being half of the ‘64 Parcel’ case (i.e., 128 corresponds to four parcels per cell initially.)	67
24	Contour of mass fraction of SF_6 with particle distribution (white dots). The first row corresponds to $St \ll 1.0$ (Case 0.5-1), the second row to $St \approx 1.0$ (Case 4.0-1), and the third row to $St \gg 1.0$ (Case 64.0-1).	68
25	Amplitude growth for small particles with different mass loadings (Case 0.5-X) and the ‘No particle’ case.	70
26	Normalized amplitudes for Case 0.5-X and the ‘No particle’ cases. The x -axis is normalized by the multiphase Richtmyer velocity.	71
27	Amplitude growth for large particles with different mass loadings (Case 64.0-X).	72
28	Normalized amplitudes for Case 64.0-X and the ‘No particle’ cases. The x -axis is normalized by the singlephase Richtmyer velocity.	72
29	Initial configuration of RMI of the perturbed shape particle clouds. The grey region denotes the region filled with the gas-particle mixture.	73
30	Comparison of the effect of number of parcels to the amplitude growth for the second kind of RMI under study for Case P0.5-1. In the legend, ‘64 Parcel’, ‘128 Parcel’ and ‘256 Parcel’ denote the number of parcels used in the y -direction, respectively, with the corresponding inter-parcel distance applied also in the x -direction.	75
31	Growth of particle perturbation at different times for the second kind of RMI.	75
32	Amplitude growth of perturbed shape particle clouds with different initial particle mass loading for Case P0.5-X ($X = 1, 2, 3$ & 4).	76
33	Normalized amplitude of perturbed shape particle clouds for Cases P0.5-X ($X = 1, 2, 3$ & 4).	77
34	Changes in the behavior of the amplitude growth for different particle sizes.	78

SUMMARY

Richtmyer-Meshkov instability (RMI) occurs when an interface of two fluids with different densities is impulsively accelerated. The main interest in RMI is to understand the growth of perturbations, and numerous theoretical models have been developed and validated against experimental/numerical studies. However, most of the studies assume very simple initial conditions. Recently, more complex RMI has been studied, and this study focuses on two cases: reshocked RMI and multiphase RMI.

It is well known that reshock to the species interface causes rapid growth of interface perturbation amplitude. However, the growth rates after reshock are not well understood, and there are no practical theoretical models yet due to its complex interface conditions at reshock. A couple of empirical expressions have been derived from experimental and numerical studies, but these models are limited to certain interface conditions. This study performs parametric numerical studies on various interface conditions, and the empirical models on the reshocked RMI are derived for each case. It is shown that the empirical models can be applied to a wide range of initial conditions by choosing appropriate values of the coefficient.

The second part of the study analyzes the flow physics of multiphase RMI. The linear growth model for multiphase RMI is derived, and it is shown that the growth rates depend on two nondimensional parameters: the mass loading of the particles and the Stokes number. The model is compared to the numerical predictions under two types of conditions: a shock wave hitting (1) a perturbed species interface surrounded by particles, and (2) a perturbed particle cloud. In the first type of the problem, the growth rates obtained by the numerical simulations are in agreement with the

multiphase RMI growth model when Stokes number is small. However, when the Stokes number is very large, the RMI motion follows the single-phase RMI growth model since the particles do not rapidly respond while the RMI instability grows. The second type of study also shows that the multiphase RMI model is applicable if Stokes number is small. Since the particles themselves characterize the interface, the range of applicable Stokes number is smaller than the first study. If the Stokes number is in the order of one or larger, the interface experiences continuous acceleration and shows the growth profile similar to a Rayleigh-Taylor instability.

CHAPTER I

INTRODUCTION

Richtmyer-Meshkov instability (RMI) occurs when an interface between two media of different densities is impulsively accelerated, for instance by a shock wave. This phenomenon was first theoretically proven by Richtmyer [79], and later experimentally verified by Meshkov [58]. RMI occurs in various natural and engineering situations such as supernovae explosions [4], deflagration-to-detonation transition [70], confinement fusion [50], and fuel mixing in a scramjet [95]. The RMI evolution can be characterized by the inviscid, compressible vorticity equation [96]:

$$\frac{D\boldsymbol{\omega}}{Dt} = \underbrace{\frac{\nabla\rho \times \nabla p}{\rho^2}}_{\text{baroclinic production}} + \underbrace{\boldsymbol{\omega} \cdot \nabla \mathbf{u}}_{\text{vortex stretching}} - \underbrace{\boldsymbol{\omega}(\nabla \cdot \mathbf{u})}_{\text{vortex dilatation}}, \quad (1)$$

where p denotes the pressure, ρ is the density, \mathbf{u} is the velocity, $\boldsymbol{\omega} = \nabla \times \mathbf{u}$ is the vorticity, and $D/Dt = \partial/\partial t + \mathbf{u} \cdot \nabla$. A driving mechanism of RMI is the baroclinic torque vorticity production term that is caused by a misalignment of the pressure and density gradients. When a shock interacts with the perturbed interface, vorticity is deposited by this baroclinic term, and the interface is subsequently accelerated based on the direction of vorticity. This interface perturbation can be considered as a combination of a bubble and a spike [11], where a bubble is the region where the lighter fluid penetrates into the heavier fluid, and a spike is the region where the heavier fluid penetrates into the lighter fluid as shown in a schematic presented in Fig. 1. To quantify RMI evolution, one can define the mixing length, h , as the distance between the spike and the bubble tips, a mean amplitude, $a = h/2$, and the amplitudes, a_b and a_s , as the distance from the unperturbed interface location to bubble or spike tip, respectively.

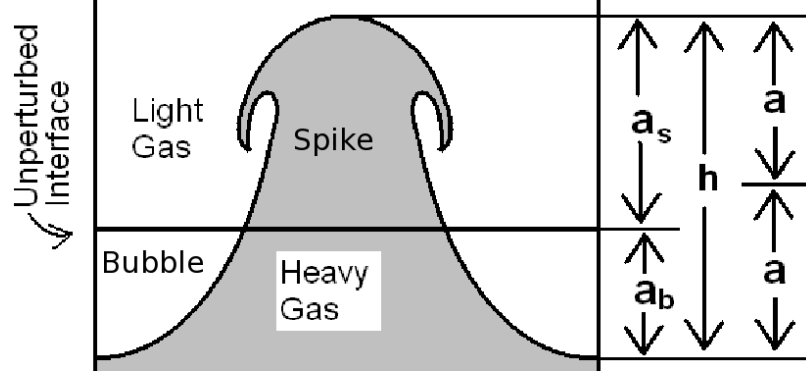


Figure 1: Bubble and spike definition for a RMI perturbation. The gray and white regions correspond to the heavy and light species, respectively.

Unlike the Rayleigh-Taylor instability (RTI) [88], which is driven by a continuous acceleration, RMI is unstable in either a light-heavy or a heavy-light configuration as shown in Fig. 2 [96]. A shock propagating from the light gas side (light-heavy configuration) deposits vorticity that can amplify the original perturbation. On the other hand, if the shock is approaching from the heavy gas side (heavy-light configuration), the vorticity causes interface motion initially to reduce the perturbation, and spikes and bubbles are eventually inverted and grow in opposite directions [96].

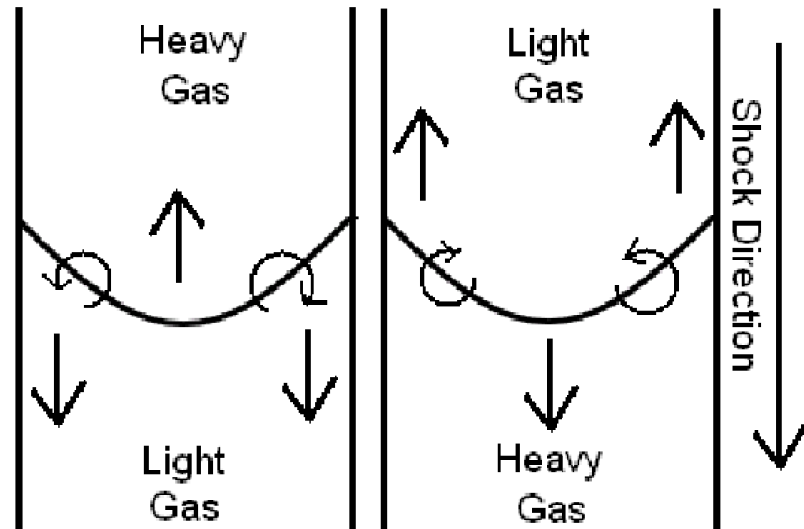


Figure 2: Vorticity deposition over a species interface with heavy-light (left) and light-heavy (right) configurations.

Numerous theoretical/empirical growth models of single-mode perturbation have been proposed in the past and have been validated against experimental and numerical studies [13, 19, 42, 46]. RMI occurring in natural and engineering environments are generally more complex. Therefore, many studies have been performed to investigate RMI with more complex interface conditions such as a multi-mode interface [2], with a reshock [48, 91, 93], in cylindrical geometries [52], and in spherical explosions [7]. However, most of these past studies only focus on single-phase flow, and RMI analysis in multiphase flows is still in its infancy, even though particles might implicitly play important role in many cases, such as explosions with reactive metal particles [7], chondrules concentration in a nebula [21] and possibly other multiphase systems involving shock waves.

1.1 Review of RMI growth models

Growth rates of single-mode RMI have been studied for over fifty years. This section explains past development of RMI growth rate studies under different conditions.

1.1.1 Single-mode RMI

Richtmyer [79] originally developed a linear growth model of the amplitude, $a(t)$ based on an impulsive model:

$$a(t) = a_0 + v_0 t, \quad (2)$$

where a_0 is the initial amplitude, v_0 is the Richtmyer velocity defined as $v_0 = ka_0 A \Delta V_1$, k is the wavenumber given as $k = 2\pi/\lambda$, λ is the wavelength, A is the Atwood number defined as $A = (\rho_2 - \rho_1)/(\rho_2 + \rho_1)$, and ΔV_1 is the change in the speed of the interface due to an incident shock. Here, ρ_1 and ρ_2 denote, respectively, the density of the light and the heavy fluid. The impulsive model is only applicable in the linear-regime where $ka < 0.3$ [19]. Therefore, non-linear models have been developed to predict the late time growth rates. A potential flow model for RTI [47] was extended to RMI [39, 63], but such models were limited to $A=1$ (fluid-vacuum

interface) and were only applicable to obtain the initial and the asymptotic (time $\rightarrow \infty$) growth rates [39, 63, 97]. To deal with the constraints of potential flow models, several Padé approximation based models have been developed [55, 92, 98] to numerically obtain the time-dependent solution with an arbitrary Atwood number. However, these approximation methods were not very successful [42] because even very high order approximations depart from the solution of the models at late times. More recently, Goncharov [35] developed a potential flow model for an arbitrary Atwood number, and Mikaelian [64] extended Goncharov’s work to obtain an explicit time-dependent expression. Sadot et al. [80] obtained an empirical expression to link the initial and asymptotic solution of the potential flow model [39]. The advantage of this empirical model is that the coefficients can be modified to adapt to different analytical models [42]. Past studies have employed 2D [19, 42, 46, 69] and 3D [13, 53] single-mode RMI experiments and numerical analysis to evaluate and identify the domain of applicability of these models.

1.1.2 Multi-mode RMI

Although the growth models for single-mode RMI are well established, growth models for multi-mode or random perturbation are not yet fully developed. Multi-mode growth is more practically relevant since the interface shape is most likely to be random in realistic systems. Mikaelian [65] recently developed a technique to describe the development of arbitrary interface shapes in the linear-regime by using Fourier expansion. However, non-linear interactions of bubbles and spikes make the interface shape very unpredictable at the late-time. Moreover, the exact shape of the initial interface is not usually prescribed or well defined. If the mixing zone is assumed to be filled with turbulence, the growth of the mixing zone can be interpreted as the evolution of a turbulent layer that follows a power law [11] such as:

$$h(t) \approx t^\theta, \tag{3}$$

where the value of θ is found based on different assumptions. Barenblatt [9] derived $\theta < 2/3$ for the turbulent plane layer with Kolmogorov similarity hypothesis. Clark & Zhou [16] assumed that a shock causes only weakly anisotropic turbulence and found $2/7 < \theta < 1/2$. However, this approach cannot include the effect of Atwood number, which is concluded to be a very important factor [22].

Models based on the time-dependent average wavelength growth have also been developed. Alon et al. [1, 2] applied the two-dimensional statistical bubble merger model, and obtained the power law for bubble and spike individually:

$$h_{b/s}(t) \approx t^{\theta_{b/s}}, \quad (4)$$

where the subscripts b and s denote bubble and spike. A value of $\theta_b = 0.4$ for any Atwood number and $0.4 < \theta_s < 1.0$ as function of Atwood number were obtained in this analysis. However, experimental results [22] showed that θ_b and θ_s are smaller than proposed values. Oron et al. [71] pointed out that the dimensionality of the flow changes the merging process, and that both θ_b and θ_s in 3D are about half the values of the flow in 2D model ($\theta_b = 0.25$ and $0.2 < \theta_s < 1.0$).

1.1.3 Reshock RMI models

Recently, the Richtmyer-Meshkov instability involving multiple shocks has been studied. The RMI with multiple shocks is seen in many confined systems such as shock tubes [3, 48, 93] and blast waves [6, 7], and it has been shown that the impulsive acceleration of the evolving interface demonstrates different growth behaviors. For example, RMI with a second shock (often termed as a reshock) has been shown to cause a rapid increase of growth rates and thereby enhance the amount of mixing [3, 48, 93].

Even though the growth models of single-mode RMI are well established, the post-reshock models are still in their infancy. The change in the growth rate due to reshock was first analytically studied by Mikaelian [61] by applying the potential flow model

of the single-mode RMI to a growing perturbation; the criteria to determine whether the second shock accelerates, decelerates, freezes out, or inverts the perturbation were analyzed. Brouillette & Sturtevant [12] extended the original Richtmyer’s model to multiple shock systems. However, both these models are a function of the wavelength and amplitude at reshock, a_r , and they are only applicable when the amplitude at the second shock is very small ($a_r \ll k$) as originally assumed in Richtmyer’s model (Eqn. 2). Due to the very complex interface shapes at reshock, it is difficult to construct analytic models, and so two empirical models applicable to specific interface configurations have been developed. The first model is Mikaelian’s reshock model [62] developed for the multi-mode 3D perturbation, and is the linear correlation:

$$\frac{dh_2}{dt} = C\Delta V_2 A^+, \quad (5)$$

where $\frac{dh_2}{dt}$ is the growth rate after reshock, ΔV_2 is the velocity jump caused by the second shock, A^+ is post-reshock Atwood number, and $C = 0.28$ is an empirically determined constant from experimental RTI studies [78]. The second model is Charakhch’an’s model [14] that is obtained from the numerical studies of single-mode 2D RMI with reshock; it was found that the growth rate is only a weak function of a_r and k at the second shock. The following empirical expression was derived [14]:

$$\frac{dh_2}{dt} = \beta\Delta V_2 A - \frac{dh_1}{dt}, \quad (6)$$

where $\frac{dh_1}{dt}$ is the growth rate immediately before the reshock, and $\beta = 2.5$ from multiple numerical results. Note that $\frac{dh_1}{dt}$ and $\frac{dh_2}{dt}$ have opposite signs as they correspond to perturbation growth in opposite directions. Limitations and applicable ranges of these reshock models are summarized in Table 1.

Charakhch’an’s model and Mikaelian’s reshock model agree with the assumption that the reshock growth rate is not a function of k or a_r . In fact, past experiments have indicated that the growth rate after a reshock is independent of the interface

shape [26, 48, 93] for 3D multi-mode RMI. Vetter and Sturtevant [93] performed RMI with reshock and found that the post-reshock growth rates follow the Mikaelian’s reshock model. Later, Erez et al. [26] showed that the initial membrane thickness does not influence the post-reshock growth rate, although it affects the growth rate after the incident shock. More recently, Leinov et al. [48] performed experiments of RMI with reshock for different wall distances and reshock Mach numbers, and found that the reshock growth follows the Milaelian’s reshock model with slightly larger coefficient, i.e., $C \approx 0.38$. These experimental results clearly indicate that the post-reshock growth rate is not a function of the interface condition at reshock.

Since most of the experimental studies are performed in shock tubes with a flat membrane separating two gases [41, 48, 75, 93], it is hard to obtain the exact initial perturbation shapes for numerical simulation. This is a serious issue since the initial interface shape can be very critical for RMI because the vorticity is deposited only when a shock hits the interface. Past numerical attempts approximated the initial conditions from a configuration of a wire mesh used to support a membrane. For instance, numerical studies undertaken by [17, 37, 40, 83] used an egg-carton type perturbation to model the RMI experiments with the membrane supported by a cross wired mesh [93]. Moreover, Schilling & Latini [83] investigated the effect of the magnitude of the random noise on the late time growth rates and also compared it with Mikaelian’s model. Mügler & Gauthier [66] performed a 2D numerical study of the experiments by Poggi et al. [75], with initial conditions defined as a combination

Table 1: List of existing reshock models.

	Interface Geometry	Function	Limitation
Mikaelian’s potential model [61]	2D single-mode	$a_r, k, \Delta V_2$	$a_r \ll k$
Brouillette & Sturtevant model [12]	2D single-mode	$a_r, k, \Delta V_2$	$a_r \ll k$
Charakhch’an’s model [14]	2D single-mode	ΔV_2	
Mikaelian’s reshock model [62]	3D multi-mode	ΔV_2	

of sinusoidal waves with eight different wavelengths that are in the same order of the wire mesh spacing. Although these wire based initializations provide a good approximation for the wavelength, the estimation of the initial amplitude is still ambiguous because it is difficult to precisely measure how much the membrane is pushed into the wire mesh before it ruptures. Therefore, Leinov et al. [48] neglected the wire mesh supports, and simply modeled the initial perturbation as a summation of sinusoidal planes with different wavelengths and amplitudes.

Apart from the flat membrane settings, Schilling et al. [84] briefly analyzed the post-reshock growth rates of 2D single-mode RMI based on the membrane-less experiment performed by Collins & Jacobs [19].

1.2 Multiphase RMI

RMI in multiphase environments has not been studied yet to the extent of the author's knowledge. Therefore, this section summarizes the past studies on multiphase instability and particle dispersions by shock.

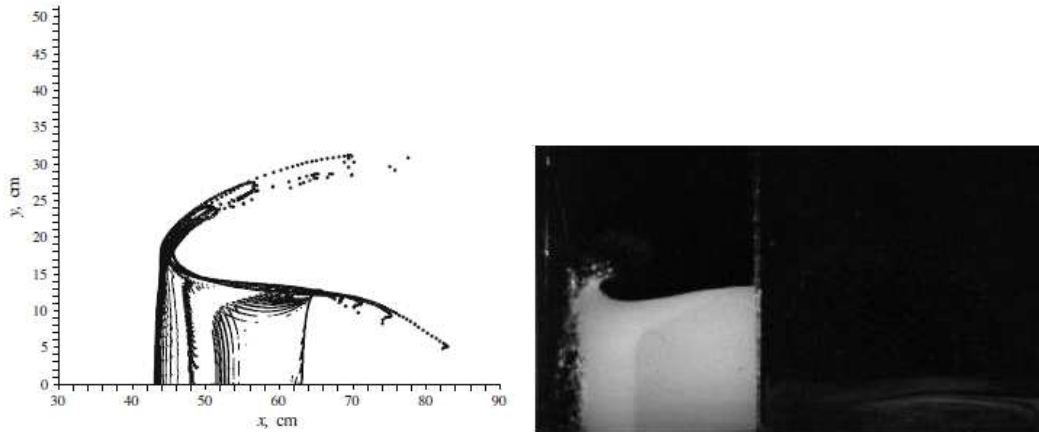
1.2.1 Effect of particles on instabilities

In general, particles in a flow field are known to effect the instability of the gas-phase. For example, it has been shown in the past that particles modify the Orr-Sommerfeld equation and stabilize or de-stabilize the transition to turbulence depending on the particle size [81]. In another study, the amplitude growth of multiphase Kelvin-Helmholtz instability (KHI) [60] was reduced due to particles in the vicinity of the interface. The interaction of a RMI with particle clouds has never been studied to the best of the authors' knowledge, and the present investigation attempts to establish the growth model of multiphase RMI by applying the dusty gas formulation [81] with the assumption that a cloud of a large number of particles behaves as a pseudo-fluid. Various kinds of instabilities in multiphase flows have been investigated in the past with regard to the Orr-Sommerfeld equation [81], Poiseuille flow [59] and KHI [60]

by performing a linear perturbation analysis on the dusty gas formulation. However, the growth models of multiphase RMI have not yet been developed and analyzed.

1.2.2 Instabilities of a particle cloud

There are various studies of deformation of particle clouds by shocks with different shapes of particle clustering [10, 43, 44], but none of them are analyzed in terms of RMI. Since the idea of the dusty gas formulation suggests that a particle cloud itself can be treated as a different gas, a region filled with particles can be treated as a dense gas, and the RMI growth model is explored under certain conditions. For example, Ota et al. [72] observed the deformation of a half-height dense gas caused by a shock wave, and Kiselev et al. [44] performed numerical simulations with a similar setup but having particle clouds instead of a heavy gas. Their results showed qualitatively that particle dispersion shapes are very similar to the deformation of a dense gas. Moreover, past numerical studies [74, 86] investigated the clouds of heavy particles falling into a light fluid, and reported the formation of structures similar to the Rayleigh-Taylor instability (RTI). Thus, this study compares the shock accelerated perturbed particle clouds against the classical RMI.



(a) The numerical simulation of the deformation of the square particle clouds (b) The experimental results of the deformation of SF_6 cube

Figure 3: The comparison of particle dispersion and deformation of SF_6 by shock.

1.3 Objectives

The primary objectives of the thesis are to study the Richtmyer-Meshkov instability under complex situation such as reshock and multiphase.

1. Investigate the RMI interface growth after reshock and develop a model applicable to the wide ranges of initial conditions.

Charakhch'an's [14, 15] and Mikaelian's [62] reshock models are only appropriate for a specific regime of RMI and cannot be applied to the same RMI configuration. For example, if dh_1/dt is very small, Charakhch'an's model and Mikaelian's reshock model have the same equation with different values of the coefficient. Furthermore, since there is serious scarcity of data about the single-mode RMI after reshock, Charakhch'an's model is not yet fully validated. Therefore, a re-investigation of the coefficient is performed in the present work.

Past numerical studies have tested a limited type of initial perturbation shape, and the effect of initial is not fully understood yet. Given these observations, it is clear that there still remains some uncertainty about RMI growth after reshock. Therefore, the present work investigates reshocked RMI for four different combinations of initial interface geometry and perturbation: 2D single-mode, 3D single-mode, 2D multi-mode and 3D multi-mode, and investigates the differences in the ensuing growth rates. Since the experimental validations of the post-reshock growth rates are only available for 3D multi-mode RMI, the latest reshocked RMI experiments by Leinov et al. [48] are chosen as a base configuration, and the other types of perturbation shapes are examined under the same conditions. Then, parametric studies of each type of initial interface shapes are performed to investigate the controlling factors of the reshocked RMI growth rates.

2. Establish a basic understanding of the behavior of RMI interactions involving dilute particle clouds and draw useful insights.

Almost all the RMI studies only consider single-phase flows, even though the effect of particles on RMI growth can be significant. However, detailed analysis of RMI involving particle interactions has not been performed yet. Thus, this study attempts to establish a linear growth model of multiphase RMI using the dusty gas formulation and compares the model with the numerical predictions under two types of conditions. The first type involves the impulsive acceleration of a perturbed species interface of air/ SF_6 surrounded by a uniformly distributed cloud of particles as often considered as the multiphase instability studies. The range of applicability of the multiphase RMI growth model is evaluated by simulating for a wide range of parametric. The second type of RMI study undertaken here is the shock wave induced dispersion of a particle cloud with a perturbed shape within a uniform gas. Since shock-particle interactions are not considered as RMI in general, this study aims to examine whether the amplitude growth follows RMI-type growth rates by performing again a detailed parametric study.

1.4 Outline

This thesis is organized as follows. Chapter 2 describes the governing equations used to simulate gas-phase and particle tracking scheme. The compressible Navier-stokes equations for multi-species and multiphase flows are presented, and the Lagrangian method used for the particle tracking is discussed. Chapter 3 presents numerical schemes used to solve the governing equations. The results of reshock studies are described in Chapter 4. The parametric studies of single-/multi-RMI are performed in two- and three-dimensional domains. The multiphase RMI is discussed in Chapter 5. First, the growth model for the multiphase RMI is derived, and then it is compared to the numerical predictions with two types of configurations such as the species

interface surrounded by the particles and the interface characterized by the particles itself. Finally, conclusions and recommendations for future work are given in Chapter 6.

CHAPTER II

MATHEMATICAL FORMULATION AND MODELING

This chapter presents the governing equations of the compressible Navier-Stokes equations and the particle tracking schemes.

2.1 The Navier-Stokes Equations

The compressible Navier Stokes equations for multi-species and multiphase flows under the dilute limit (negligible solid volume fraction) are [7]:

$$\frac{\partial \rho}{\partial t} + \frac{\partial \rho u_i}{\partial x_i} = \dot{\rho}_p, \quad (7)$$

$$\frac{\partial \rho u_i}{\partial t} + \frac{\partial}{\partial x_j} [\rho u_i u_j + p \delta_{ij} - \tau_{ij}] = \dot{F}_{p,i}, \quad (8)$$

$$\frac{\partial \rho E}{\partial t} + \frac{\partial}{\partial x_i} [(\rho E + p) u_i + q_i - u_j \tau_{ij}] = \dot{Q}_p + \dot{W}_p, \quad (9)$$

$$\frac{\partial \rho Y_k}{\partial t} + \frac{\partial}{\partial x_i} [\rho Y_k u_i + J_{i,k}] = \dot{S}_{p,k} \quad k = 1, \dots, N_s. \quad (10)$$

Here, ρ is the density, $(u_i)_{i=1,2,3}$ is the velocity vector in Cartesian coordinates, P is the pressure, E is the total energy, Y_k is the mass fraction for species k , τ_{ij} is shear stress tensor, q_i is the rate of heat transfer, $J_{i,k}$ is the diffusion flux, and N_s is the total number of species in the flow. Here, $\dot{\rho}_p$, $\dot{F}_{p,i}$, $\dot{Q}_{p,i}$, $\dot{W}_{p,i}$ and $\dot{S}_{p,k}$ are respectively, the source terms of mass, momentum, heat, work and species due to the presence of particles. The current study assumes that the particle loading is dilute, so that volume occupied by particles is considered to be negligible. Also in this study, only momentum exchange is considered, hence, only $\dot{F}_{p,i} \neq 0$. The total energy, E is defined as:

$$E = e + \frac{1}{2} u_k u_k, \quad (11)$$

where e is the internal energy given as:

$$e = \sum_{k=1}^{N_s} Y_k h_k - \frac{P}{\rho}, \quad (12)$$

and the sensible enthalpy of k -th species, h_k is found as:

$$h_k(T) = \Delta h_{f,k}^0 + \int_{T_0}^T c_{P,k}(T') dT', \quad (13)$$

where T is the temperature, T_0 is the reference temperature, $\Delta h_{f,k}^0$ is the enthalpy formation at the reference temperature and pressure, and $c_{P,k}$ is the specific heat at the constant pressure. Thermodynamic variables are computed by the equation of state for a calorically perfect gas:

$$P = \rho RT, \quad (14)$$

$$R = \sum_{k=1}^{N_s} Y_k \frac{R_u}{MW_k}, \quad (15)$$

where R_u is the universal gas constant and MW_k is the molecular weight of the k -th species.

Assuming the Newtonian fluids, the shear stress tensor, τ_{ij} is proportional to the rate of strain defined as:

$$\tau_{ij} = \mu \left(\frac{\partial u_i}{\partial x_j} - \frac{\partial u_j}{\partial x_i} \right) - \frac{2}{3} \delta_{ij} \mu \frac{\partial u_k}{\partial x_k}, \quad (16)$$

where μ is the molecular viscosity coefficient. The rate of heat transfer is computed by the Fourier's law that assumes the rate of heat conduction is proportional to the local temperature gradient. Also, the enthalpy changes caused by the species diffusion must be considered as well. Thus, the heat flux is given as:

$$q_i = -\kappa \frac{\partial T}{\partial x_i} + \rho \sum_{k=1}^{N_s} Y_k h_k V_{i,k}. \quad (17)$$

There are various models to compute the diffusion velocities. The present study uses the mixture averaged formulation [76] given as:

$$V_{i,k} = -\frac{1}{X_k} D_{km} \frac{\partial X_k}{\partial x_i}, \quad (18)$$

where $V_{i,k}$ is the diffusion velocity, X_k is the mole fraction of the k -th species and D_{km} is the mixture diffusion coefficient for the k th species defined as:

$$D_{km} = \frac{\sum_{j \neq k}^{N_s} X_j MW_j}{MW_m \sum_{j \neq k}^{N_s} X_j / \mathcal{D}_{jk}}, \quad (19)$$

However, the diffusion velocity does not satisfy the mass conservation $\left(\sum_{k=1}^{N_s} V_{ik} Y_k \neq 0\right)$, so that the correction velocity must be used to adjust the mass flow such as:

$$V_i^c = -\sum_{k=1}^{N_s} Y_k \left(\frac{1}{X_k} D_{km} \frac{\partial X_k}{\partial x_i} \right). \quad (20)$$

Thus, the diffusion flux of k -th species is given as:

$$J_{i,k} = \rho Y_k (V_{ik} + V_i^c). \quad (21)$$

The molecular viscosity coefficient in the mixture of multiple fluids is given by the Wilke's formula [77, 94]:

$$\mu = \sum_{k=1}^{N_s} \frac{X_k \eta_k}{\sum_{j=k}^{N_s} X_j \Phi_{kj}}, \quad (22)$$

where

$$\Phi_{kj} = \frac{1}{\sqrt{8}} \left(1 + \frac{W_k}{W_j} \right)^{-\frac{1}{2}} \left(1 + \left(\frac{\eta_k}{\eta_j} \right)^{\frac{1}{2}} \left(\frac{W_j}{W_k} \right)^{\frac{1}{4}} \right)^2, \quad (23)$$

and the η_i in this formulation represents the i -th species viscosity. The thermal conductivity is similarly calculated by using the following formula:

$$\kappa = \frac{1}{2} \left(\sum_{k=1}^{N_s} X_k \lambda_k + \frac{1}{\sum_{k=1}^{N_s} X_k / \lambda_k} \right). \quad (24)$$

where λ_k is the pure species conductivity of k th species.

2.2 Particle Tracking - Lagrangian Scheme

There are multiple methods to compute the dynamics of the multiphase flow depending on the purposes and flow conditions [5, 54]. The Eulerian and Lagrangian scheme are the most well known schemes. The Eulerian scheme treats particles as continuum media, so that it is suited to handle a large number of particles. However, the disadvantage of the scheme is that the diffusion term is somewhat artificial [54]. Also, the boundary conditions of the pseudo-fluid, for example at wall, are not well defined. On the other hand, the Lagrangian scheme tracks the velocity and location of point-particles. The advantages of the Lagrangian scheme are that the detailed information and statistics of each particle can be obtained. Also, the Lagrangian scheme does not require the artificial diffusive models used in the Eulerian schemes. Moreover, it is easier to define the boundary conditions. Therefore, the Lagrangian scheme is used for the present study. However, the drawback of the Lagrangian scheme is that it can be very costly if a large number of particles are used in the computational domain. Thus, the present study applies the concept of “parcel” that consists of multiple particles with the same characteristics such as positions, velocity and radius. It is possible to reduce the computational load by substituting particles by parcels.

The assumptions of the particle tracking scheme are summarized as follows [27]:

1. The volume fraction of the particles are small, so that interactions between particles is neglected.
2. The particle is spherical, so that the particle drag model is based in solid sphere data.
3. External forces such as gravity, Basset force and virtual mass effect are neglected

Under these assumptions, the governing equations of the particle trajectories are given as [57]:

$$\frac{dx_{p,i}}{dt} = v_i, \quad (25)$$

$$m_p \frac{dv_i}{dt} = \frac{\pi}{2} r_p^2 C_D \rho |u_i - v_i| (u_i - v_i), \quad (26)$$

where $x_{p,i}$ is the position of the particle, u_i is the local velocity of the gas at the location of the particle, v_i is the velocity of the particle, r_p is the particle radius, ρ is density of gas, m_p is the particle mass and C_D is the drag coefficient. The drag coefficient is generally expressed as a function of the particle Reynolds number, $Re_d = \frac{2r_p \rho |u - v|}{\mu}$, where μ is the viscosity of the gas. Eqn. (26) typically contains other terms on the right hand side to include the effect of pressure gradient, the Basset term, the Saffman lift and the Magnus lift [56]. For this dilute study, all these effects are neglected as a first approximation. Assuming spherical particles, the drag coefficient, C_D is obtained from the empirical relations [20] as:

$$C_D = \begin{cases} \frac{24}{Re_d} \left(1 + \frac{1}{6} Re_d^{2/3}\right) & Re_d < 1000 \\ 0.424 & Re_d > 1000 \end{cases}. \quad (27)$$

It is shown that heat transfer between the fluid and the particles can affect shock-particle interactions [73]. However, heat transfer is neglected in the present study as also done in previous instability analysis [60, 81].

The momentum coupling term, $\dot{F}_{p,i}$ is given as [7]:

$$\dot{F}_{p,i} = \frac{1}{V} \sum_{n=1}^N n_{p,n} \left[\frac{\pi}{2} r_{p,n}^2 C_{D,n} \rho_n |u_{i,n} - v_{i,n}| (v_{i,n} - u_{i,n}) \right], \quad (28)$$

where $n_{p,n}$ is the number of particles per parcel and N is the number of parcel belong to the computational cell. The source terms of mass, energy and species transfer is not considered and not discussed in the present work. Descriptions of each term are available elsewhere [57].

CHAPTER III

NUMERICAL METHODS

The simulation of Richtmyer-Meshkov instability encounters large discontinuities near shocks and species interface. Therefore, upwinding schemes are often used for the RMI simulations [66]. However, such discontinuities exist only in a small portion of the domain, and it is preferable to apply high-order non-dissipative schemes within the smooth regions since the upwinding scheme is dissipative. Therefore, a hybrid scheme is used in the present study to accurately capture RMI structures with maintaining high-order solutions. Previous studies show that the hybrid schemes are very successful to simulate RMI. For example, Hill et al. [40] used a hybrid scheme with tuned-center difference (TCD) in the smooth region and WENO for shock capturing, to study RMI. Fryxell & Menon [29] also demonstrated hybrid scheme that used a fourth order scheme for smooth flow and Piecewise-Parabolic method (PPM) for the shock capturing method and apply it to study RMI. The present study applies the hybrid scheme developed by Génin & Menon [32, 33, 34] that has been successfully applied for various flows such as shock/turbulence interaction [34] and turbulent mixing in supersonic flows [33]. The hybrid scheme uses the fourth-order central schemes within the smooth region, but reverts to the flux difference splitting (FDS) method when the discontinuities are found. This chapter discusses the discretization of the governing equations, central scheme, flux difference splitting method, and the switching criteria. Then, the numerical schemes for the particle tracking is also explained. The numerical method and the validation of the scheme were reported elsewhere[30, 34].

3.1 Discretization of the governing equations

3.1.1 Finite volume method

The governing equations can be written in the following conservation form:

$$\frac{\partial \mathbf{Q}}{\partial t} + \frac{\partial \mathbf{F}_x}{\partial x} + \frac{\partial \mathbf{F}_y}{\partial y} + \frac{\partial \mathbf{F}_z}{\partial z} = \mathbf{S}, \quad (29)$$

where \mathbf{Q} is the state vector, \mathbf{F}_x , \mathbf{F}_y and \mathbf{F}_z is the flux in each direction, and \mathbf{S} is the source term, and each vector is given as:

$$\mathbf{Q} = \begin{pmatrix} \rho \\ \rho u \\ \rho v \\ \rho w \\ \rho E \\ \rho Y_k \end{pmatrix}, \quad (30)$$

$$\mathbf{F}_x = \begin{pmatrix} \rho u \\ \rho u u + P \\ \rho u v \\ \rho u w \\ \rho u (E + P) \\ \rho u Y_k \end{pmatrix} - \begin{pmatrix} 0 \\ \tau_{xx} \\ \tau_{xy} \\ \tau_{xz} \\ u\tau_{xx} + v\tau_{xy} + w\tau_{xz} - q_x \\ \rho Y_k V_{x,k} \end{pmatrix}, \quad (31)$$

$$\mathbf{F}_y = \begin{pmatrix} \rho v \\ \rho v u \\ \rho v v + P \\ \rho v w \\ \rho v (E + P) \\ \rho v Y_k \end{pmatrix} - \begin{pmatrix} 0 \\ \tau_{yx} \\ \tau_{yy} \\ \tau_{yz} \\ u\tau_{yx} + v\tau_{yy} + w\tau_{yz} - q_y \\ \rho Y_k V_{y,k} \end{pmatrix}, \quad (32)$$

$$\mathbf{F}_z = \left\{ \begin{array}{c} \rho w \\ \rho w u \\ \rho w v \\ \rho w w + P \\ \rho w(E + P) \\ \rho w Y_k \end{array} \right\} - \left\{ \begin{array}{c} 0 \\ \tau_{zx} \\ \tau_{zy} \\ \tau_{zz} \\ u\tau_{zx} + v\tau_{zy} + w\tau_{zz} - q_z \\ \rho Y_k V_{z,k} \end{array} \right\}, \quad (33)$$

$$\mathbf{S} = \left\{ \begin{array}{c} \dot{\rho}_p \\ \dot{F}_{p,x} \\ \dot{F}_{p,y} \\ \dot{F}_{p,z} \\ \dot{Q}_p \\ \dot{S}_{p,k} \end{array} \right\}. \quad (34)$$

The Navier-Stokes equations are solved with the finite volume method that applies the conservation principles on a control volume. The changes of the mass, momentum, energy and species within the control volume are determined by the net flux of each quantity and the source term. The integral form of the conservation form above can be described as following:

$$\iiint_V \frac{\partial \mathbf{Q}}{\partial t} dV + \iint_{\Sigma} (\mathbf{F}_x n_x + \mathbf{F}_y n_y + \mathbf{F}_z n_z) d\Sigma = \iiint_V \mathbf{S} dV, \quad (35)$$

where Σ represents the surface of a control volume and n_x , n_y and n_z is the x, y and z- components of the normal vector of the surface. The control volume consists of six surface elements for three-dimensional computation by using structured grid, so that the change of the state variables is represented as follows:

$$d\mathbf{Q} = -\frac{dt}{V} \sum_{l=1}^6 (\mathbf{F}_x n_x + \mathbf{F}_y n_y + \mathbf{F}_z n_z) \Sigma_l + \mathbf{S} dt, \quad (36)$$

where l indicates each surface element. The present study uses the cell-centered scheme that stores the state variables at the center of cell (i, j, k) .

3.1.2 Domain discretizations

The finite volume scheme assumes that the structured, three-dimensional Cartesian grid. Since cells are not rectangular and uniformly spaced all the time, a curvilinear physical domain (x, y, z) is transformed to the uniform computational domains (ξ, η, ζ) given as:

$$\begin{cases} \frac{\partial}{\partial x} = \xi_x \frac{\partial}{\partial \xi} + \eta_x \frac{\partial}{\partial \eta} + \zeta_x \frac{\partial}{\partial \zeta} \\ \frac{\partial}{\partial y} = \xi_y \frac{\partial}{\partial \xi} + \eta_y \frac{\partial}{\partial \eta} + \zeta_y \frac{\partial}{\partial \zeta} \\ \frac{\partial}{\partial z} = \xi_z \frac{\partial}{\partial \xi} + \eta_z \frac{\partial}{\partial \eta} + \zeta_z \frac{\partial}{\partial \zeta} \end{cases}, \quad (37)$$

where $\xi_x, \eta_x, \zeta_x, \xi_y, \eta_y, \zeta_y, \xi_z, \eta_z$ and ζ_z are the grid metrics.

Thus, the conservative form is transformed in the computational domain given as:

$$\frac{\partial \mathbf{Q}}{\partial t} + \frac{\partial \mathbf{F}'_x}{\partial \xi} + \frac{\partial \mathbf{F}'_y}{\partial \eta} + \frac{\partial \mathbf{F}'_z}{\partial \zeta} = S, \quad (38)$$

where,

$$\begin{cases} \mathbf{Q}' = \frac{1}{J} \mathbf{Q} \\ \mathbf{F}'_x = \frac{1}{J} (\xi_x \mathbf{F}_x + \xi_y \mathbf{F}_y + \xi_z \mathbf{F}_z) \\ \mathbf{F}'_y = \frac{1}{J} (\eta_x \mathbf{F}_x + \eta_y \mathbf{F}_y + \eta_z \mathbf{F}_z) \\ \mathbf{F}'_z = \frac{1}{J} (\zeta_x \mathbf{F}_x + \zeta_y \mathbf{F}_y + \zeta_z \mathbf{F}_z) \end{cases}, \quad (39)$$

and J is the grid Jacobian of three-dimensional grid transformation given as:

$$J = \frac{1}{\frac{\partial x}{\partial \xi} \frac{\partial y}{\partial \eta} \frac{\partial z}{\partial \zeta} + \frac{\partial x}{\partial \zeta} \frac{\partial y}{\partial \xi} \frac{\partial z}{\partial \eta} + \frac{\partial x}{\partial \eta} \frac{\partial y}{\partial \zeta} \frac{\partial z}{\partial \xi} - \frac{\partial x}{\partial \xi} \frac{\partial y}{\partial \zeta} \frac{\partial z}{\partial \eta} - \frac{\partial x}{\partial \eta} \frac{\partial y}{\partial \xi} \frac{\partial z}{\partial \zeta} - \frac{\partial x}{\partial \zeta} \frac{\partial y}{\partial \eta} \frac{\partial z}{\partial \xi}}. \quad (40)$$

3.1.3 Time Integration - McCormack scheme

The McCormack scheme is used to the time integration [34]. It is an explicit predictor-corrector scheme described as:

$$\begin{aligned} Q^{(*)} &= Q^{(n)} + dQ^{(n)} && \text{(Predictor)} \\ Q^{(n+1)} &= \frac{1}{2} [Q^{(n)} + Q^{(*)} + dQ^{(*)}] && \text{(Corrector)}, \end{aligned} \quad (41)$$

where $Q^{(*)}$ is computed based on the state variables and the change of state variables computed using the property at the time step n , and $Q^{(n+1)}$ is the state variables at the next time steps. The McCormack scheme ensures second-order time accuracy in time.

The time step is determined by the properties in the cell. The following equation is used to compute the time step in each cell:

$$\Delta t = \left[\frac{CFL}{\frac{|u|}{\Delta x} + \frac{|v|}{\Delta y} + \frac{|w|}{\Delta z} + a\sqrt{\frac{1}{(\Delta x)^2} + \frac{1}{(\Delta y)^2} + \frac{1}{(\Delta z)^2}} + \frac{2\gamma\nu}{\rho Pr} \left(\frac{1}{(\Delta x)^2} + \frac{1}{(\Delta y)^2} + \frac{1}{(\Delta z)^2} \right)} \right], \quad (42)$$

and the smallest Δt found in the computational domain is used as the global time step. $CFL = 0.5$ and $= 0.25$ are used for 2nd and 4th order-method respectively to keep the numerical scheme stable.

3.2 Central Schemes

A central scheme is used to compute flux in the smooth region since the scheme is not very dissipative. The flux at cell interface is computed from the state variables at the interface such as:

$$F_{i+\frac{1}{2}}^{\pm} = F \left(Q_{i+\frac{1}{2}}^{\pm} \right), \quad (43)$$

where $+$ and $-$ denote forward and backward differencing, and the directions are switched at for predictor and corrector to maintain the order of the scheme.

The original formulation of McCormack scheme that results 2nd-order accuracy in space is given as:

$$\begin{aligned} Q_{i+\frac{1}{2}}^+ &= Q_{i+1}, \\ Q_{i+\frac{1}{2}}^- &= Q_i, \end{aligned} \quad (44)$$

where $+$ and $-$ denote the forward and backward differencing, and the directions is switched at each iteration so as not to bias the solution by direction. Gottlieb & Turkel [36] extended McCormack scheme and obtain the fourth-order scheme given

as:

$$\begin{aligned} Q_{i+\frac{1}{2}}^+ &= \frac{1}{6} (7Q_{i+1} - Q_{i+2}), \\ Q_{i+\frac{1}{2}}^- &= \frac{1}{6} (7Q_i - Q_{i-1}). \end{aligned} \tag{45}$$

Later, Nelson [67, 68] pointed out the scheme of Gottlieb & Turkel is only third-order accurate in space, and developed a fourth-order scheme given as:

$$\begin{aligned} Q_{i+\frac{1}{2}}^+ &= \frac{1}{6} (2Q_i + 5Q_{i+1} - Q_{i+2}), \\ Q_{i+\frac{1}{2}}^- &= \frac{1}{6} (2Q_{i+1} + 5Q_i - Q_{i-1}). \end{aligned} \tag{46}$$

Derivatives are similarly computed by fourth-order scheme. ξ derivatives of the primitive variables at $i + 1/2$ interface are found as:

$$\begin{aligned} \frac{\partial u^+}{\partial \xi} &= \frac{1}{6} (-u_{i+2} + 8u_{i+1} - 7u_i), \\ \frac{\partial u^-}{\partial \xi} &= \frac{1}{6} (u_{i-1} + 8u_i - 7u_{i+1}). \end{aligned} \tag{47}$$

Similarly, the derivative transverse to the interface is computed by central differencing given as:

$$\frac{\partial u}{\partial \eta} = \frac{1}{12} (-u_{j+2} + 8(u_{j+1} - u_{j-1}) + u_{j-2}). \tag{48}$$

3.3 Flux-difference splitting method

Upwinding schemes are applied near discontinuities since central schemes tend to cause numerical oscillations. The present study uses the flux difference splitting (FDS) method that computes flux based on the wave propagation. Monotone Upstream Centered Scheme for Conservation Laws (MUSCL) re-construction is used to keep the high-order solutions, and flux is computed by HLLC/E [34]. Note that the FDS method is only applied to the inviscid flux and the viscous flux is still computed by a fourth-order central scheme.

3.3.1 MUSCL interface reconstruction

The MUSCL reconstruction evaluates the state variables at the left and right of the interface assuming a piecewise-linear function shown as following equations:

$$\begin{aligned} U_{i+1/2}^L &= U_i + \frac{\epsilon(1-\xi_i)}{4} [(1-\kappa)(U_i - U_{i-1}) + (1+\kappa)(U_{i+1} - U_i)], \\ U_{i+1/2}^R &= U_{i+1} - \frac{\epsilon(1-\xi_{i+1})}{4} [(1+\kappa)(U_{i+1} - U_i) + (1-\kappa)(U_{i+2} - U_{i+1})], \end{aligned} \quad (49)$$

where ξ is the flattening factor explained later, and the order of the scheme is determined by the value of ϵ and κ as shown in Table 2.

ϵ	0	1	1	1	1
κ	any	-1	1	1	1/3
Order	1st	2nd	2nd	2nd	3rd

Table 2: List of order of accuracy of MUSCL scheme

If the first-order method is used, the numerical scheme become very dissipative. However, the higher-order approximation in Eqn. (49) will over- and under-predict the state value so that numerical oscillations are generated. Therefore, the slope limiter function, $\phi(r)$, is introduced given as:

$$\begin{aligned} U_{i+1/2}^L &= U_i + \frac{\epsilon(1-\xi_i)}{4} \left[(1-\kappa)\phi(r_{i-1/2}^+)(U_i - U_{i-1}) + (1+\kappa)\phi(r_{i+1/2}^-)(U_{i+1} - U_i) \right], \\ U_{i+1/2}^R &= U_{i+1} - \frac{\epsilon(1-\xi_{i+1})}{4} \left[(1-\kappa)\phi(r_{i+3/2}^-)(U_{i+2} - U_{i+1}) + (1+\kappa)\phi(r_{i+1/2}^+)(U_{i+1} - U_i) \right], \end{aligned} \quad (50)$$

where r is defined as:

$$\begin{aligned} \Delta_{i+1/2}(U) &= U_{i+1} - U_i \\ \Delta_{i+1/2}^+(U) &= \Delta_{i+1/2}(U)\phi(r_{i+1/2}^+) & r_{i+1/2}^+ &= \frac{\Delta_{i+3/2}(U)}{\Delta_{i+1/2}(U)} \\ \Delta_{i+1/2}^-(U) &= \Delta_{i+1/2}(U)\phi(r_{i+1/2}^-) & r_{i+1/2}^- &= \frac{\Delta_{i-1/2}(U)}{\Delta_{i+1/2}(U)}, \end{aligned} \quad (51)$$

Various types of limiters have proposed in the past such as [49]:

- Minmod Limiter

$$\phi_{mm}(r) = \max[0, \min(r, 1)], \quad (52)$$

- Superbee Limiter

$$\phi_{sb}(r) = \max [0, \min(2r, 1), \min(r, 2)], \quad (53)$$

$$\begin{aligned} \phi_{\beta}(r) &= \max [0, \min(\beta r, 1), \min(r, \beta)], \\ 1 &\leq \beta \leq 2 \end{aligned} \quad (54)$$

- Monotonized Central Limiter

$$\phi_{mc}(r) = \max \left[0, \min(2r, 2, \frac{1+r}{2}) \right], \quad (55)$$

- Van Leer Limiter

$$\phi_{vl}(r) = \frac{|r| + r}{1 + r}, \quad (56)$$

- Van Albada Limiter

$$\phi_{va}(r) = \frac{r^2 + r}{1 + r^2}. \quad (57)$$

Since all the limiters introduced here hold symmetry defined as:

$$\frac{\phi(r)}{r} = \phi\left(\frac{1}{r}\right), \quad (58)$$

Eqn (50) can be simplified as:

$$\begin{aligned} U_{i+1/2}^L &= U_i + \frac{\epsilon(1-\xi_i)}{2} \phi(r_{i-1/2}^+) (U_i - U_{i-1}), \\ U_{i+1/2}^R &= U_{i+1} - \frac{\epsilon(1-\xi_{i+1})}{2} \phi(r_{i+3/2}^-) (U_{i+2} - U_{i+1}). \end{aligned} \quad (59)$$

The MUSCL reconstructions are applied to ρ , u_i , P , T and ρ_k . However, corrections on the species term are required since the result of the MUSCL reconstruction must also satisfy $\sum_{i=1}^{N_s} Y_i = 1.0$. Therefore, the present study limits the equations of interface construction as follows:

$$\begin{aligned} \rho_{k,i+\frac{1}{2}}^l &= \rho_{k,i} + \frac{\epsilon(1-\xi_i)}{2} \underbrace{\min}_{k=0..N_s} \left(\phi \left(r_{i-1/2}^+ (\rho_k) \right) \right) (\rho_{k,i} - \rho_{k,i-1}), \\ \rho_{k,i+\frac{1}{2}}^r &= \rho_{k,i+1} - \frac{\epsilon(1-\xi_{i+1})}{2} \underbrace{\min}_{k=0..N_s} \left(\phi \left(r_{i+3/2}^- (\rho_k) \right) \right) (\rho_{k,i+2} - \rho_{k,i+1}), \end{aligned} \quad (60)$$

where $k = 0$ indicate the total gas density.

The fluttering function is used to reduce the order of accuracy near the strong shock. The shock is detected by the velocity and pressure criteria given as [18]:

$$\begin{aligned} d_{P,i} &= \frac{|P_{i+1}-P_{i-1}|}{\min(P_{i+1},P_{i-1})} - \frac{1}{3} > 0, \\ d_{u,i} &= u_{i+1} - u_{i-1} < 0. \end{aligned} \tag{61}$$

If the shock is found, the fluttering factor is computed as following:

$$\begin{aligned} \tilde{\xi}_i &= \max \left[0, \min \left(1, 10 \left(\frac{P_{i+1}-P_{i-1}}{P_{i+2}-P_{i-2}} - 0.75 \right) \right) \right], \\ \xi_i &= \begin{cases} \max(\tilde{\xi}_i, \tilde{\xi}_{i+1}), & \text{if } (P_{i+1} - P_{i-1}) < 0 \\ \max(\tilde{\xi}_i, \tilde{\xi}_{i-1}). & \text{otherwise} \end{cases} \end{aligned} \tag{62}$$

3.3.2 Riemann solvers

The interface fluxes are calculated from U^L and U^R obtained by MUSCL scheme. There are various numerical methods to deal with the Riemann problem. This study applies a hybrid Riemann solver, HLLC/E [34, 33], that uses HLLE and HLLC depending on the flow conditions. The following sections give brief descriptions of HLLE, HLLC and the switching criteria of HLLC/E.

3.3.2.1 HLLE Riemann solver

HLL (Harten, Lax and Leer) Riemann solver [38] assumes two waves, left- and right-moving waves that characterize three regions of different solutions. The scheme is also called HLLE if the wave speed is determined by the Einfeldt's scheme [24, 25]. Assuming the control volume of $[X_l, X_r] \times [0, \Delta t]$ as shown in Fig. 4, the state variables after time step, Δt is described as:

$$\begin{aligned} \int_{X_l}^{X_r} U(x, \Delta t) dx - \left(\int_{X_l}^0 U(x, 0) dx + \int_0^{X_r} U(x, 0) dx \right) = \\ \int_0^{\Delta t} F(U(X_l, t)) dt - \int_0^{\Delta t} F(U(X_r, t)) dt. \end{aligned} \tag{63}$$

Eqn. (63) is simply integrated and simplified as:

$$\begin{aligned} U^*(S^R - S^L)\Delta t - (-U^L(S^L\Delta t) + U^R(S^R\Delta t)) \\ = F^L(\Delta t) - F^R(\Delta t), \end{aligned} \tag{64}$$

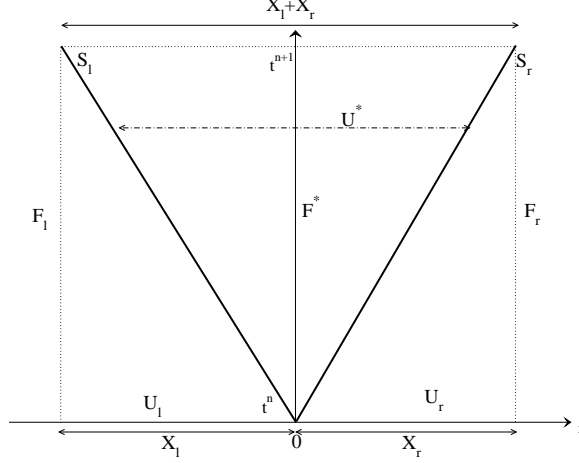


Figure 4: HLLC configuration of the different waves at cell interfaces

and U^* is found as:

$$U^* = \frac{F^L - S^L U^L - (F^R - S^R U^R)}{S^R - S^L}. \quad (65)$$

From U^* the flux at the interface, F^* need to be derived, but $F^* \neq F(U^*)$ to keep the conservation laws of the control volume. Therefore, F^* is found by analyzing left $[X_l, 0]$ and right $[0, X_r]$ portion of the control volume as performed in Eqn. (63) and obtain:

$$\begin{aligned} -(U^* - U^L)S^L \Delta t &= (F^L - F^*) \Delta t \quad (Left), \\ (U^* - U^R)S^R \Delta t &= (F^* - F^R) \Delta t \quad (Right), \end{aligned} \quad (66)$$

and so that F^* is determined as:

$$F^* = \frac{S^R F^L - S^L F^R + S^L S^R (U^R - U^L)}{S^R - S^L}. \quad (67)$$

Thus, the HLLC scheme is summarized as:

$$F_{i+1/2}^{HLLC} = \begin{cases} F^L & \text{if } 0 \leq S^L \\ F^* & \text{if } S^L \leq 0 \leq S^R \\ F^R & \text{if } S^R \leq 0 \end{cases} \quad (68)$$

3.3.2.2 HLLC Riemann solver

Toro et al. [89] improved HLL by adding a contact surface (HLLC). The control representation with the contact surface can be represented by the following conservative

law:

$$\left(\int_{X_l}^{X^*} U(x, \Delta t) dx + \int_{X^*}^{X_r} U(x, \Delta t) dx \right) - \left(\int_{X_l}^0 U(x, 0) dx + \int_0^{X_r} U(x, 0) dx \right) = \int_0^T F(U(X_l, t)) dt - \int_0^T F(U(X_r, t)) dt. \quad (69)$$

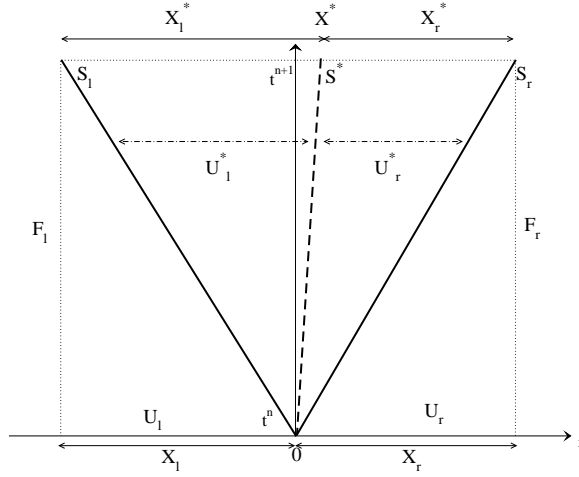


Figure 5: HLLC configuration

The integrated form of Eqn. (69) is given as:

$$(U^{L^*}(S^* - S^L)\Delta t + U^{R^*}(S^R - S^*)\Delta t) - (-U^L(S^L\Delta t) + U^R(S^R\Delta t)) = F^L(\Delta t) - F^R(\Delta t), \quad (70)$$

and Eqn. (70) is simplified as:

$$(S^* - S^L)U^{L^*} + (S^R - S^*)U^{R^*} = F^L - S^L U^L - (F^R - S^R U^R). \quad (71)$$

The control volume of each segment is analyzed, and the Rankin-Hugoniot condition are used to find:

$$\begin{aligned} F^{L^*} &= F^L + S^L (U^{L^*} - U^L), \\ F^{L^*} &= F^{R^*} + S^* (U^{L^*} - U^{R^*}), \\ F^{R^*} &= F^R + S^R (U^{R^*} - U^R), \end{aligned} \quad (72)$$

However, there are only three equations obtained for four unknown parameters (F^{L^*} , F^{R^*} , U^{L^*} and U^{R^*}), so that one more equation is derived from the interface conditions

expressed as following:

$$\begin{aligned}
(\vec{V}^{L^*} \cdot \vec{n} = q^{L^*}) &= (\vec{V}^{R^*} \cdot \vec{n} = q^{R^*}) = S^*, \\
P^{L^*} &= P^{R^*}, \\
\phi^{L^*} &= \phi^L, \quad \phi^{R^*} = \phi^R,
\end{aligned} \tag{73}$$

where ϕ represents the passive scalars.

To apply the interface conditions, the continuity and momentum equations of either right or left moving wave is shown as:

$$\underbrace{\begin{bmatrix} \rho^{k^*} S^* \\ \rho^{k^*} S^* u^{k^*} + P^{k^*} n_x \\ \rho^{k^*} S^* v^{k^*} + P^{k^*} n_y \\ \rho^{k^*} S^* w^{k^*} + P^{k^*} n_z \end{bmatrix}}_{F^{k^*}} = \underbrace{\begin{bmatrix} \rho^k q^k \\ \rho^k q^k u^k + P^k n_x \\ \rho^k q^k v^k + P^k n_y \\ \rho^k q^k w^k + P^k n_z \end{bmatrix}}_{F^k} + S^k \left(\underbrace{\begin{bmatrix} \rho^{k^*} \\ \rho^{k^*} u^{k^*} \\ \rho^{k^*} v^{k^*} \\ \rho^{k^*} w^{k^*} \end{bmatrix}}_{U^{k^*}} - \underbrace{\begin{bmatrix} \rho^k \\ \rho^k u^k \\ \rho^k v^k \\ \rho^k w^k \end{bmatrix}}_{U^k} \right). \tag{74}$$

The continuity equation shows that:

$$\rho^{k^*} = \rho^k \frac{S^k - q^k}{S^k - S^*}, \tag{75}$$

and similarly, the momentum equations obtains an expression of pressure such as:

$$P^{k^*} = P^k + \rho^k (q^k - S^k)(q^k - S^*). \tag{76}$$

Thus, U^{k^*} can be represented as

$$U^{k^*} = \alpha^k U^k + \begin{bmatrix} 0 \\ \rho^k \omega^k n_x \\ \rho^k \omega^k n_y \\ \rho^k \omega^k n_z \\ \frac{P^* S^* - P^k q^k}{(S^k - S^*)} \\ 0 \\ 0 \end{bmatrix}, \tag{77}$$

where,

$$\begin{aligned}\beta^k &= \frac{S^* - q^k}{S^k - S^*}, \\ \alpha^k &= \beta^k + 1, \\ \omega^k &= -\beta^k(q^k - S^k)\end{aligned}\tag{78}$$

Therefore, the interface flux determined by HLLC is given as:

$$F_{i+1/2}^{HLLC} = \begin{cases} F^L & \text{if } 0 \leq S^L \\ F^{L*} = F^L + S^L(U^{L*} - U^L) & \text{if } S^L \leq 0 \leq S^* \\ F^{R*} = F^R + S^R(U^{R*} - U^R) & \text{if } S^* \leq 0 \leq S^R \\ F^R & \text{if } S^R \leq 0 \end{cases}\tag{79}$$

3.3.2.3 Wave-speed estimation

There are various methods to estimate wave-speed, and Einfeldt's method [24, 25] is applied in the present study. He defined the left- and the right-moving wave as:

$$S^L = \min [q^L - c^L, \check{q} - \check{c}] \quad S^R = \max [q^R + c^R, \check{q} + \check{c}],\tag{80}$$

where \check{q} and \check{c} are the Roe-averaged contravariant velocity and speed of sounds respectively derived from the Roe-averaged variables are determined as:

$$\check{U} = \begin{bmatrix} \check{\rho} \\ \check{u} \\ \check{v} \\ \check{w} \\ \check{H} \\ \check{Y}_k \end{bmatrix} = \frac{1}{\sqrt{\rho^L} + \sqrt{\rho^R}} \left(\sqrt{\rho^L} \begin{bmatrix} \sqrt{\rho^L \rho^R} \\ u^L \\ v^L \\ w^L \\ H^L \\ Y_{k,l} \end{bmatrix} + \sqrt{\rho^R} \begin{bmatrix} \sqrt{\rho^L \rho^R} \\ u^R \\ v^R \\ w^R \\ H^R \\ Y_{k,r} \end{bmatrix} \right),\tag{81}$$

and \check{c} is computed from the Roe-averaged quantities, instead of taking Roe-average of c^L and c^R . The speed of the contact surface, S^* used in HLLC is found by applying the interface conditions (Eqn. 73). The mass and the momentum conservation at the contact surface are:

$$\begin{aligned}
& (S^* - S^L) \underbrace{\begin{bmatrix} \rho^{L^*} \\ \rho^{L^*} u^{L^*} \\ \rho^{L^*} v^{L^*} \\ \rho^{L^*} w^{L^*} \end{bmatrix}}^{U^{L^*}} + (S^R - S^*) \underbrace{\begin{bmatrix} \rho^{R^*} \\ \rho^{R^*} u^{R^*} \\ \rho^{R^*} v^{R^*} \\ \rho^{R^*} w^{R^*} \end{bmatrix}}^{U^{R^*}} = S^R \underbrace{\begin{bmatrix} \rho^R \\ \rho^R u^R \\ \rho^R v^R \\ \rho^R w^R \end{bmatrix}}^{U^R} - S^L \underbrace{\begin{bmatrix} \rho^L \\ \rho^L u^L \\ \rho^L v^L \\ \rho^L w^L \end{bmatrix}}^{U^L} + \\
& \underbrace{\begin{bmatrix} \rho^L q^L \\ \rho^L q^L u^L + P^L n_x \\ \rho^L q^L v^L + P^L n_y \\ \rho^L q^L w^L + P^L n_z \end{bmatrix}}_{F^L} - \underbrace{\begin{bmatrix} \rho^R q^R \\ \rho^R q^R u^R + P^R n_x \\ \rho^R q^R v^R + P^R n_y \\ \rho^R q^R w^R + P^R n_z \end{bmatrix}}_{F^R}.
\end{aligned} \tag{82}$$

Then, the two mass and vectorial momentum balance are given as:

$$\begin{aligned}
& \rho^{L^*}(S^* - S^L) + \rho^{R^*}(S^R - S^*) = \rho^R(S^R - q^R) - \rho^L(S^L - q^L), \\
& \underbrace{\left[\rho^{L^*}(S^* - S^L) + \rho^{R^*}(S^R - S^*) \right]}_{S^*} = P^L - P^R + \rho^R q^R (S^R - q^R) - \rho^L q^L (S^L - q^L).
\end{aligned} \tag{83}$$

Since the right-hand of mass conservation equation can substitute the under-braced term in the momentum balancing equation, S^* can be obtained as:

$$S^* = \frac{P^R - P^L + \rho^L q^L (S^L - q^L) - \rho^R q^R (S^R - q^R)}{\rho^L (S^L - q^L) - \rho^R (S^R - q^R)}. \tag{84}$$

3.3.2.4 HLLC/E

The purpose of the hybrid scheme is to use the HLLC since it is less diffusive, but to avoid the carbuncle effect induced by HLLC. Thus, HLLC/E detects shock location and uses HLLE transverse to the shock front within the shock region [31]. Therefore, the hybrid scheme HLLC/E uses switching based on the shock detection method Eqn.

(61) such as:

$$F_{i+1/2}^u = \begin{cases} F_{i+1/2}^{HLLLE} & \text{if } (d_{P,j} < 0 \text{ and } d_{u,j} < 0) \text{ or } (d_{P,k} < 0 \text{ and } d_{u,k} < 0) \\ F_{i+1/2}^{HLLC} & \text{otherwise} \end{cases} . \quad (85)$$

3.4 Switching criteria

The hybrid finite-volume formulation is used to integrate the conservative form of the equations so that both moving shocks and smooth flow maintains high-order solution. The numerical scheme uses a fourth-order central scheme, well adapted to turbulent simulations, in *smooth* regions. The flux evaluation, however, reverts to a high-order flux difference splitting method in regions of strong gradients. Thus,

$$F_{i+1/2} = \lambda_{i+1/2} F_{i+1/2}^s + (1 - \lambda_{i+1/2}) F_{i+1/2}^u. \quad (86)$$

where F^s is the flux obtained by the central scheme used for the smooth region, F^u is the flux computed by the FDS scheme applied near discontinuity, and λ is the switch variable. Although it is possible to have a smooth function of λ to blend F_u and F_s , the present study takes a Heavyside step function where only 0 or 1 can be taken.

Curvatures of the pressure and density are the criteria to detect the discontinuity.

The sensors are defined as:

$$S_{\phi,i} = \begin{cases} \frac{|\phi_{i+1} - 2\phi_i + \phi_{i-1}|}{|\phi_{i+1} - \phi_i| + |\phi_i - \phi_{i-1}|} - S_{\phi}^{th} & \text{if } |\phi_{i+1} - 2\phi_i + \phi_{i-1}| \geq \epsilon_{\phi} \phi_i \\ -S_{\phi}^{th} & \text{otherwise} \end{cases} , \quad (87)$$

where ϕ is the parameter used for sensor, and P and ρ are used in this study. $S_P^{th} = 0.4$, $S_{\rho}^{th} = 0.25$, $\epsilon_P = 0.005$ and $\epsilon_{\rho} = 0.1$ are used for the current study. More detailed descriptions of these scheme and validations are given in Génin [30].

$$\lambda_{i+1/2} = \begin{cases} 1 & \text{if } \max(S_{P,i}, S_{P,i+1}, S_{\rho,i}, S_{\rho,i+1}) \leq 0 \\ 0 & \text{otherwise} \end{cases} , \quad (88)$$

3.5 *Boundary conditions*

The boundary conditions (BC) are essential to solve the PDEs. In the present study, the BCs are enforced to choose the right parameters on ghost cells which are outside the computational domain and used to compute derivatives and fluxes on the boundary on the domain of interest. Following types of boundary conditions are used in this study.

- Slip Wall BC

The slip wall BC is a useful boundary condition to mimic the wall if small scale motions along the wall are not important. The slip wall requires to have no gradient of pressure ($\frac{dP}{dn} = 0$) and temperature if adiabatic ($\frac{dT}{dn} = 0$) where the n indicates the normal vector to the wall. Since it is slip wall, the gradient of the velocity tangential to the wall have any gradient to the wall as well, ($\frac{dV_t}{dn} = 0$). However, the the velocity component normal to the wall must be zero on the boundary. Thus, assuming $N + \frac{1}{2}$ represents the boundary and \mathbf{n}_n and \mathbf{n}_t are the normal and tangential components of the \mathbf{V}_N :

$$\begin{aligned} P_{N+1} &= P_N, & T_{N+1} &= T_N, \\ \mathbf{V}_{N+1} &= -\mathbf{V}_N \mathbf{n}_n + \mathbf{V}_N \mathbf{n}_t. \end{aligned} \tag{89}$$

- Periodic BC

In many types of RMI study, the periodic BC is often used to capture large scale motions. The periodic BC copies the solutions at each times steps. Assuming the $\frac{1}{2}$ and $N + \frac{1}{2}$ represents the domain boundaries:

$$\begin{aligned} N + \frac{1}{2} &: P_{N+1} = P_1, \quad T_{N+1} = T_1, \quad V_{N+1} = V_1, \\ \frac{1}{2} &: P_0 = P_N, \quad T_0 = T_N, \quad V_0 = V_N, \end{aligned} \tag{90}$$

- Supersonic outlet

The supersonic outlet BC only relies on the information in the domain. If $N + \frac{1}{2}$ is the supersonic outlet condition, the quantities of ghost cells are found as:

$$U_{N+1} = U_N. \quad (91)$$

3.6 Particle tracking

The Lagrangian particle tracking schemes solves a series of ODEs, and they are integrated by the 4th-order Runge-Kutta scheme. Runge-Kutta scheme uses the four-step approximation such that:

$$\begin{aligned} y_{n+1} &= y_n + \frac{1}{6}(k_1 + 2k_2 + 2k_3 + k_4), \\ t_{n+1} &= t_n + \Delta t^p, \end{aligned} \quad (92)$$

where k_1 , k_2 , k_3 and k_4 are defined as:

$$\begin{aligned} k_1 &= \Delta t^p f(t_n, y_n), \\ k_2 &= \Delta t^p f(t_n + \frac{1}{2}\Delta t^p, y_n + \frac{1}{2}k_1), \\ k_3 &= \Delta t^p f(t_n + \frac{1}{2}\Delta t^p, y_n + \frac{1}{2}k_2), \\ k_4 &= \Delta t^p f(t_n + \Delta t^p, y_n + k_3), \end{aligned} \quad (93)$$

where Δt^p is the time step for particle tracking, which may be different from the gas-phase time step [82]. The droplet velocity relaxation time, τ_{relax} is:

$$\tau_{relax} = [16\rho_d r_d^2 (C_D Re_d)^{-1}] / [3\rho_g \nu]. \quad (94)$$

The eddy-droplet interaction time, τ_{int} is:

$$\tau_{int} = \tau_{relax} \ln \left(1 - \frac{\Delta}{\tau_{relax} |u_i - u_{i,d}|} \right), \quad (95)$$

where Δ indicates grid size of the cell. Then, the time step of particles, Δt^p are determined as:

$$\Delta t^p = \min\{\tau_{relax}, \tau_{int}, \Delta t\}. \quad (96)$$

Thus, multiple time steps may be needed if the particle time scale is smaller than the fluid time step.

CHAPTER IV

RESHOCKED RICHTMYER-MESHKOV INSTABILITY

In this chapter, the growth rates after reshock under various initial interface shapes are analyzed. First, four types of different initial interface shapes are examined based on the experimental setup of Leinov et al. [48]. Then, parametric studies are performed to find out the important factors that determine the post-reshock growth rates.

4.1 Simulation of Experimental Setups

Based on the experimental setups of Leinov et al. [48], four initial conditions for RMI, i.e., 2D single-mode, 3D single-mode, 2D multi-mode and 3D multi-mode are simulated and are presented here. The computational domain in this study is taken from the recent experimental study of reshocked RMI performed by Leinov et al. [48], and is presented in Fig. 6. The streamwise length (L_x) is 16 cm, and the shock and the perturbed interface are located at 9 cm and 8 cm from the end wall, respectively. For 2D, the transverse length is 1 cm, and the simulation domain is discretized with a grid size of 2048×128 . For 3D, the cross sectional area is $1 \text{ cm} \times 1 \text{ cm}$, and the simulation domain is discretized with a 1024×64^2 grid. The effect of grid resolution is discussed later.

The incident shock Mach number is 1.2, and SF_6 and air are chosen as the species for the high and the low density fluid across the interface. The effect of initial conditions on the post-reshock growth rate has been addressed recently [37, 83]. However, these studies focused on a few limited cases and detailed parametric studies have not yet been performed. This study investigates four types of initial interface shapes such as 2D single-mode, 2D multi-mode, 3D single-mode and 3D multi-mode. The species interface is initialized with a thin diffusion layer using the function introduced by

Latini et al. [45] to make the initial conditions less sensitive to the grid geometry. For these initial conditions, the reshock hits the interface at around $t = 0.75$ ms and the expansion wave from the end wall reaches the interface at $t \approx 1.2$ ms. The parametric studies use these initial conditions as the baseline to analyze the effect of the different parameters for appropriate models.

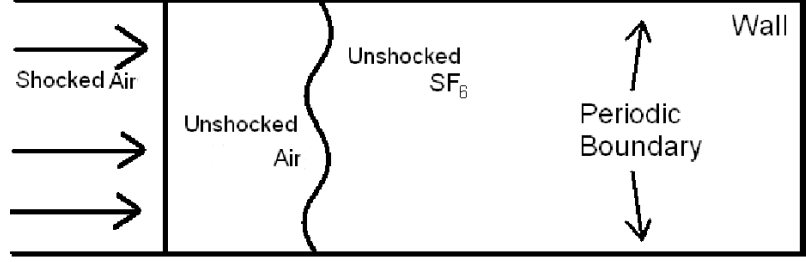


Figure 6: Schematic of the RMI test configuration. For reshock, the shock reflects from the right wall and exits from the left.

The initial conditions for single-mode RMI in 2D and 3D are defined as [13, 19]:

$$a(y) = a_0 \sin\left(\frac{2\pi}{\lambda}y\right) \quad (2D); \quad (97)$$

$$a(y, z) = a_0 \left[\sin\left(\frac{2\pi}{\lambda}y\right) + \sin\left(\frac{2\pi}{\lambda}z\right) \right] \quad (3D).$$

Similarly, multi-mode perturbation is defined as the superposition of multiple wavelengths (Eqn. 98) used by Leinov et al. [48] and Banerjee & Andrews [8].

$$a(y) = \frac{a_0}{\sigma} \sum_{k_y=1}^{k_{max}} \left[a_{1,k} \cos\left(\frac{2\pi k_y y}{L_y} + \alpha_{1,k}\right) + a_{2,k} \sin\left(\frac{2\pi k_y y}{L_y} + \alpha_{2,k}\right) \right] \quad (2D);$$

$$a(y, z) = \frac{a_0}{\sigma} \sum_{k_z=1}^{k_{max}} \sum_{k_y=1}^{k_{max}} \left[a_{1,k} \cos\left(\frac{2\pi k_y y}{L_y} + \alpha_{1,k}\right) \sin\left(\frac{2\pi k_z z}{L_z} + \beta_{1,k}\right) + \right. \\ \left. a_{2,k} \sin\left(\frac{2\pi k_y y}{L_y} + \alpha_{2,k}\right) \sin\left(\frac{2\pi k_z z}{L_z} + \beta_{2,k}\right) + \right. \\ \left. a_{3,k} \sin\left(\frac{2\pi k_y y}{L_y} + \alpha_{3,k}\right) \cos\left(\frac{2\pi k_z z}{L_z} + \beta_{3,k}\right) + \right. \\ \left. a_{4,k} \cos\left(\frac{2\pi k_y y}{L_y} + \alpha_{4,k}\right) \cos\left(\frac{2\pi k_z z}{L_z} + \beta_{4,k}\right) \right] \quad (3D). \quad (98)$$

Here, λ is the wavelength, k_y and k_z are respectively, the wavenumbers in y - and z -directions with values between 1 and k_{max} , $a_{i,k}$ are random coefficients between -1

and 1, $\alpha_{i,k}$ and $\beta_{i,k}$ are random coefficients between $-\pi$ and π , L_y and L_z are the domain sizes in y - and z -directions respectively, σ is the standard deviation of the summation part to normalize the fluctuation to be one, and the initial amplitude, a_0 determines the size of the perturbation. The parameters used for the simulation are summarized in Table 3.

Table 3: List of parameters used to construct species interface perturbations.

Case	k_{max}	a_0 (mm)	Grid Size
2D Single-mode		0.5	2048×128
2D Multi-mode	8	2.0	2048×128
3D Single-mode		1.0	1024×64 ²
3D Multi-mode	4	2.0	1024×64 ²

Grid sensitivity of the growth rate is checked for each of the simulation cases. 2D studies utilize 128 grids in the y -direction, and good agreement with a finer grid (4096×256) are seen in both single- and multi-mode RMI as a previous numerical study [46] suggests. These results are presented in Fig. 8: single-mode in (a) and multi-mode in (b). Similarly, 3D RMI with 64² cross-sectional grid shows good agreement with a finer grid (1546×96^2). Note that the amplitude growth deviate after $t = 1.2$ ms due to the reflected expansion wave, but this study is not focused on the time regimes.

Of interest in this study is to determine the mixing length growth behavior for different geometries and initial conditions. There are different methods to calculate the mixing length from the numerical results. One approach is the threshold method that defines the mixing length as the region where $\epsilon < \langle Y_{air} \rangle < 1 - \epsilon$, where $\langle Y_{air} \rangle$ denotes the line (2D) or planer (3D) average mass fraction of air, and ϵ is a small number [46, 17]; $\epsilon = 0.01$ is used in this study. The threshold measure is widely used for single and multi-mode studies, but the mixing length is influenced by the value of ϵ . Experimental studies usually utilize the threshold-type method by taking a picture

of the interface, but the definition of boundaries are not clearly defined in terms of the mass fraction. The other method is to measure the amplitude of the iso-contour of the mass fraction [12]. This iso-contour definition corresponds to theoretical values, and the diffusion thickness can be ignored, but is practically limited to single-mode studies only since it cannot account for well mixed regions. The difference between the threshold and iso-contour definition is shown in Fig. 7.

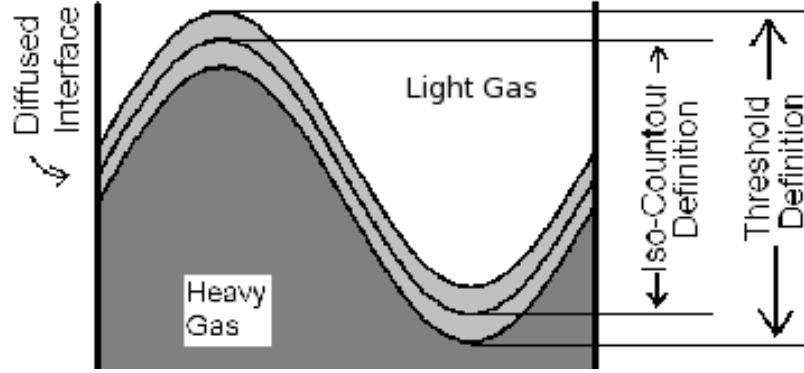


Figure 7: Differences in the mixing layer estimate by different methods.

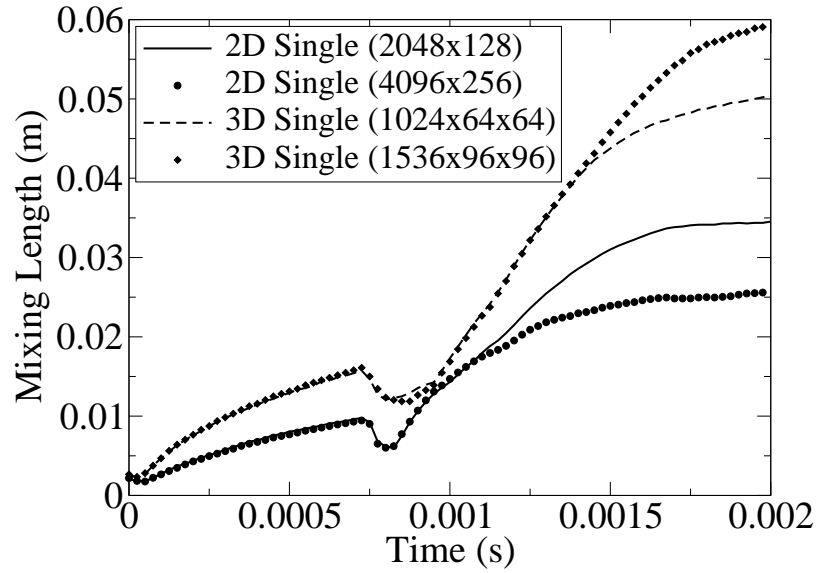
The pre-reshock growth rates of 2D and 3D single-mode RMI are also good measures to check the numerical schemes, since there are reliable theoretical and empirical models widely validated in the literature [13, 19, 42, 46, 53]. Sadot et al. [80] obtained the empirical model for the growth rate as:

$$a_{b/s}(t) = v_0 \frac{1 + v_0 kt}{1 + Dv_0 kt + Ev_0^2 k^2 t^2}. \quad (99)$$

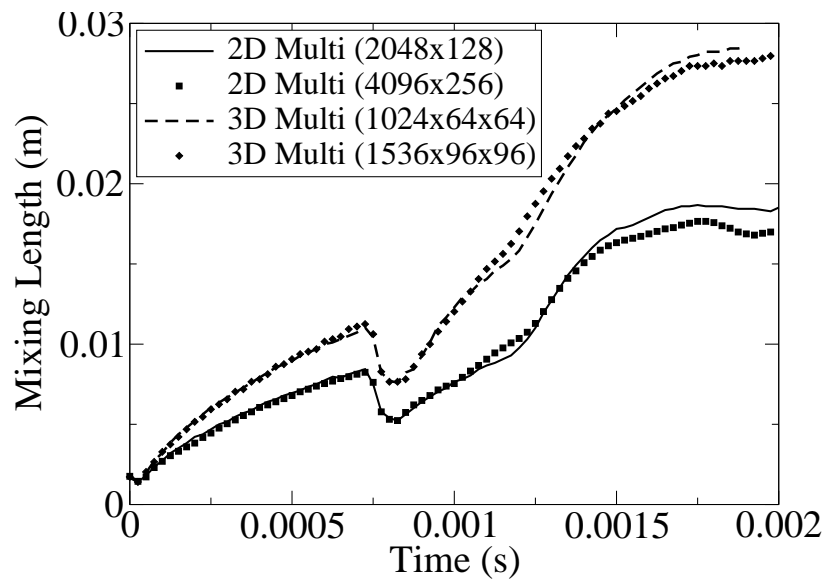
The coefficients D and E can be chosen based on different theories and are summarized in Table 4. Note that the \pm in Table 4 denotes the value used for the bubbles and spikes, respectively.

The theoretical explicit time-dependent expression obtained by Mikaelian [64] is:

$$ka_{b/s}(t) = \begin{cases} kv_0 t & \text{if } kv_0 t \leq a^*; \\ a^* + \frac{C}{1 \pm A} \ln \left[1 + \frac{1 \pm A}{C} (kv_0 t - ka^*) \right] & \text{if } kv_0 t > a^*, \end{cases} \quad (100)$$



(a)



(b)

Figure 8: Grid sensitivity of single- and multi-mode RMI in 2D and 3D.

Table 4: List of coefficients for Sadot-type models.

Model	Dimension	D	E
Sadot [80] (Original model)	2D	$1 \pm A$	$\frac{3(1 \pm A)}{2(1+A)}$
Niederhaus & Jacobs [69] (NJ)	2D	$1 \pm A$	$1 \pm A$
Goncharov [35] (G)	2D	$1 \pm A$	$\frac{3(1 \pm A)}{(3+A)}$
Sohn [87] (S)	2D	$1 \pm A$	$\frac{(2 \pm A)}{2}$
Chapman & Jacobs [13] (CJ)	3D	$1 \mp (0.01221A^3 + 0.69844A)$	$\frac{(1 \pm A)}{2}$

where $C = (3 \pm A)/3$ for 2D and $C = 2$ for 3D; a^* is the amplitude to reach non-linear growth rates, chosen as $a^* = \frac{1}{2k}$ for 2D and $a^* = \frac{1}{3k}$ for 3D. The comparisons between models and numerical simulations are shown in Figs. 9 and 10 for 2D and 3D, respectively. Note that the iso-contour definition is used to exclude diffusion thickness to be precisely comparable to models. The numerical result closely follows Sadot-Sohn model for 2D and Mikaelian for 3D, and this test exemplifies that the numerical predictions are in accordance with the theoretical models. Note that the validation study of multi-mode RMI has not been performed in this study since the growth models highly depends on the statistical approach and are not yet as established as the single-mode models.

The comparisons of growth rates for each of the simulation cases are shown in Fig. 11 and are summarized in Table 5. Each study shows distinctly different growth rates after reshock. 3D multi-mode RMI predicts the growth rate very close to the experimental value. However, 2D multi-mode RMI results very small growth rates compared to the 3D multi-mode RMI, as also observed by Gowardhan et al. [37]. The single-mode cases tend to have larger growth rates in 2D and 3D. From these results, single-mode and 3D tends to have larger growth rates than multi-mode and 2D. However, there are not enough data sets to argue the reasons for such differences. Therefore, parametric studies for each type of perturbations are performed in the following sub-sections to determine the importance of the various variables in the

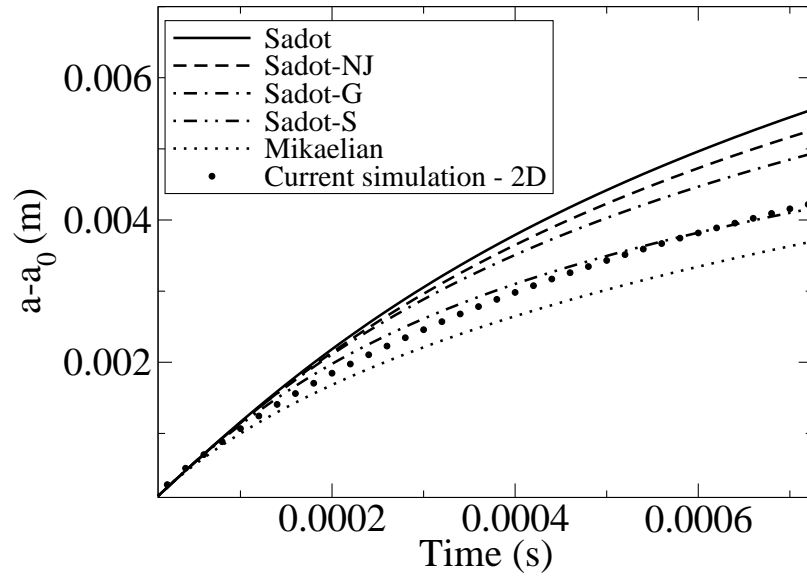


Figure 9: Comparison with the 2D RMI growth rate models.

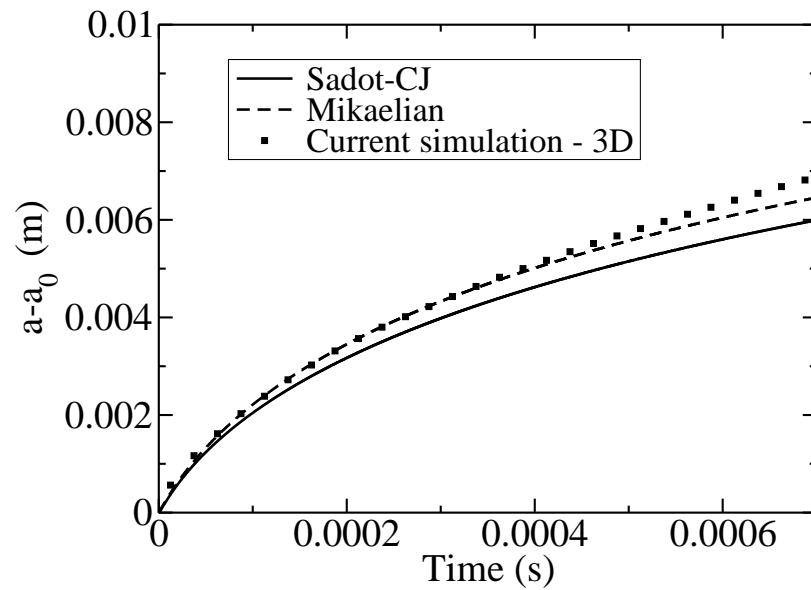


Figure 10: Comparison with the 3D RMI growth rate models.

prediction of the post-reshock growth rates.

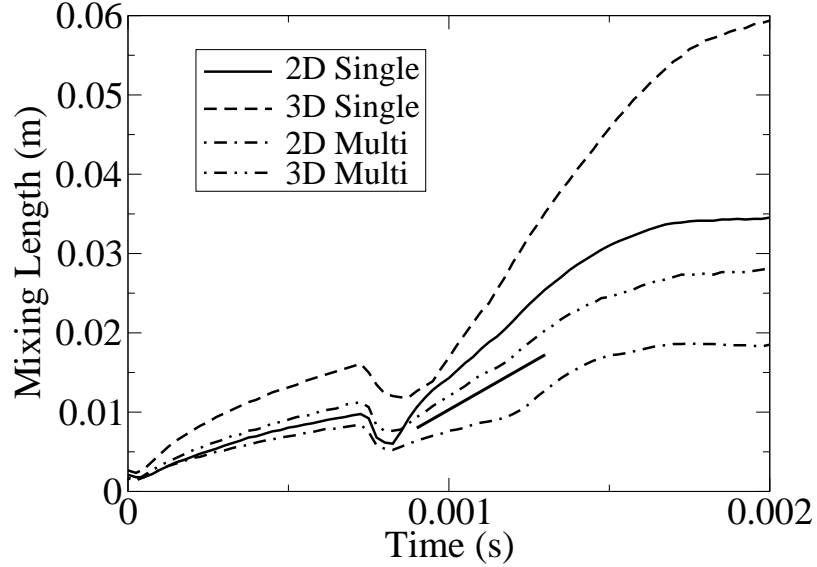


Figure 11: Comparisons of growth for each case. The straight-line represents the experimental slope of 23.1 m/s [48].

Table 5: Growth rates before and after reshock, and model coefficients for each case. C and β are coefficients found from the formulations of Mikaelian’s reshock model (Eqn. 5) and Charakhch’an’s model (Eqn. 6), respectively, where $\Delta V_2 = 92.5$ m/s and $A^+ = 0.71$.

Case	$\frac{dh_1}{dt}$	$\frac{dh_2}{dt}$	C	β
2D Single-mode	7.85	34.11	0.52	0.64
3D Single-mode	12.50	59.1	0.90	1.09
2D Multi-mode		11.65	0.17	
3D Multi-mode		25.2	0.38	

4.2 Parametric Studies of Single-Mode RMI

Even though past studies have reported that the conditions at reshock are likely to be independent of interface conditions, the previous section shows that the interface condition changes the post-reshock growth rates. Therefore, parametric studies are performed to investigate the effect of initial perturbation shapes on the post-reshock growth rates. First the study conducts parametric studies in 2D to evaluate the sensitivity of RMI growth rates after reshock to the interface shapes at reshock (a_r

Table 6: Cases simulated for 2D and 3D single-mode RMI.

Case	Dim	Grid	Domain (cm)	a_0 (mm)	L (mm)	λ (mm)	M_1
S1	2D	2048×128	16.0×1.0	0.5	40	1.0	1.2
S2	2D	2048×128	16.0×1.0	0.5	80	1.0	1.2
S3	2D	8192×128	16.0×0.25	0.125	20	0.25	1.2
S4	2D	4096×128	16.0×0.5	0.25	40	0.5	1.2
S5	2D	1024×128	16.0×2.0	1.0	80	2.0	1.2
S6	2D	2048×128	16.0×1.0	0.5	80	1.0	1.1
S7	2D	2048×128	16.0×1.0	0.5	80	1.0	1.3
S8	2D	2048×128	16.0×1.0	0.5	80	1.0	1.4
3DS1	3D	1024×64 ²	16.0×1.0 ²	1.0	80	1.0	1.1
3DS2	3D	1024×64 ²	16.0×1.0 ²	1.0	80	1.0	1.2
3DS3	3D	1024×64 ²	16.0×1.0 ²	1.0	80	1.0	1.3
3DS4	3D	1024×64 ²	16.0×1.0 ²	1.0	80	1.0	1.4

and λ) and the incident Mach number, M_1 in both 2D and 3D. The description of each test case considered in this investigation are summarized in Table 6.

First, various initial geometries are tested (Case S1-S5) and are compared to analyze the effect of the interface geometry parameters such as a_r , λ and a_r/λ . Figure 12 predicts that all cases result in similar growth rates (i.e., the slope after reshock). Note that the distance to the wall is adjusted to obtain the linear post-reshock growth rate, but the number of the grid points per perturbation is kept 128 in the y -direction for all these cases. Table 7 summarizes the growth rates and coefficients obtained from the Mikaelian’s reshock formulation and Charakhch’an’s model, and the values of these coefficients are relatively close, even though λ and a_r are different for each of the cases. Thus, the results suggest that the post-reshock growth rate is not a strong function of wavelength as Charakhch’an suggested [14, 15], and that the reshock models are a function of wavelength. Note that Mikaelian’s potential model [62] and Brouillette & Sturtevant’s model [12] are inappropriate for predicting the growth rate for perturbation amplitudes as large as the ones considered in the current investigation.

The empirical reshock models show that the growth rate is independent of the

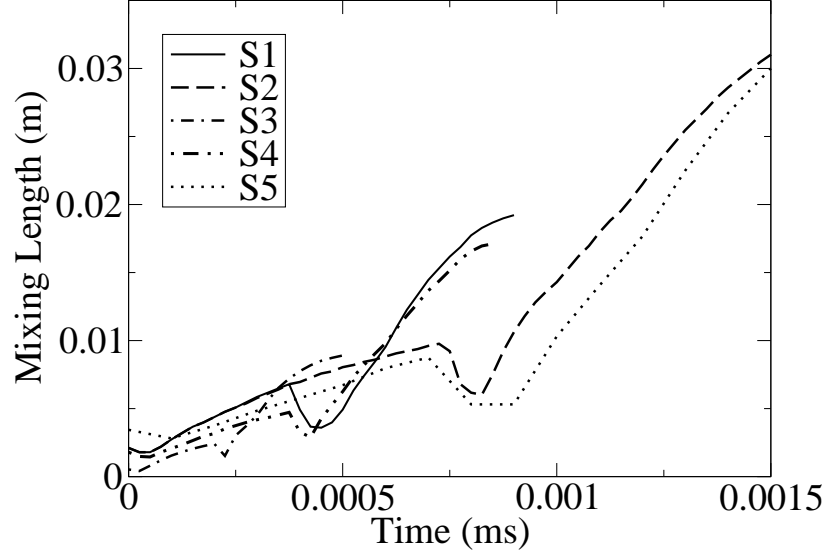


Figure 12: Mixing length growth with different initial geometries.

Table 7: 2D single-mode RMI for different a_r and λ .

Case	S1	S2	S3	S4	S5
$\frac{dh_1}{dt}$	12.50	7.85	7.42	7.81	10.15
$\frac{dh_2}{dt}$	42.50	34.11	33.83	39.84	40.15
a_r (mm)	6.48	9.77	2.42	4.72	8.75
λ (mm)	10.0	10.0	2.5	5.0	20.0
a_r/λ	0.648	0.977	0.968	0.944	0.438
β	0.84	0.64	0.63	0.73	0.77
C	0.65	0.52	0.52	0.61	0.61

interface shape at reshock, but ΔV_2 is predicted to be linearly correlated to the growth rates. The post-reshock growth rate with different ΔV_2 in 2D (Case S3, S9-11) and 3D (Case 3DS1-4) are measured by changing the incident Mach number, and the results of post-reshock growth rates are summarized in Table 8. The numerical results show higher growth rates for the cases with the higher incident Mach number, and the result is presented in Fig. 13. The linear correlation between the post-reshock growth rate and ΔV_2 in both 2D and 3D are found, as previously reported in the 3D RMI experiment with random perturbations [48], and is presented in Fig. 14 for 2D.

Table 8: 2D and 3D single-mode RMI with different incident Mach numbers.

Case	S6	S2	S7	S8	3DS1	3DS2	3DS3	3DS4
M_1	1.1	1.2	1.3	1.4	1.1	1.2	1.3	1.4
ΔV_1	45.9	68.5	99.2	127.5	45.9	68.5	99.2	127.5
ΔV_2	57.4	92.5	133.7	173.5	57.4	92.5	133.7	173.5
$\frac{dh_1}{dt}$	5.00	7.85	9.06	10.30	9.38	12.50	14.28	18.12
$\frac{dh_2}{dt}$	20.08	34.11	51.92	68.89	34.73	59.09	89.06	94.36
A^+	0.70	0.71	0.74	0.78	0.70	0.71	0.74	0.78
β	0.62	0.63	0.62	0.59	1.10	1.09	1.04	0.83
C	0.50	0.51	0.52	0.51	0.86	0.90	0.90	0.70

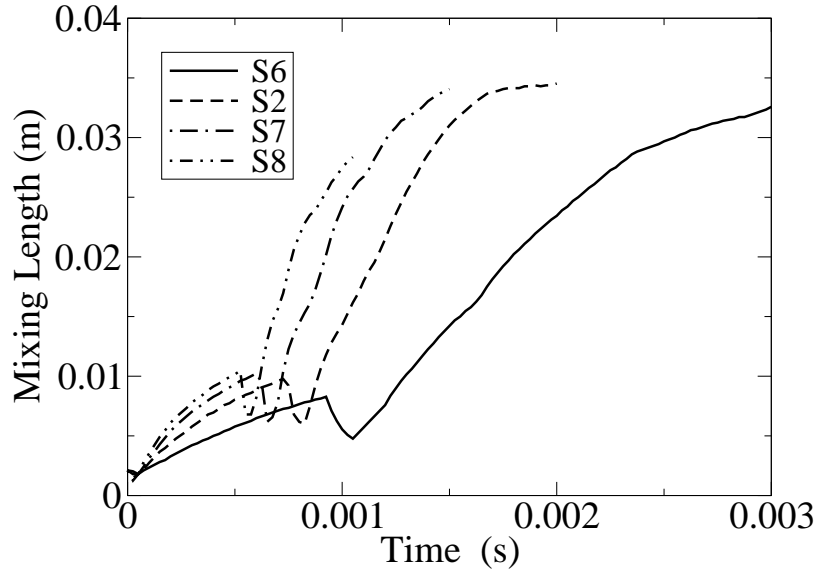


Figure 13: Amplitude of 2D RMI with different incident Mach numbers.

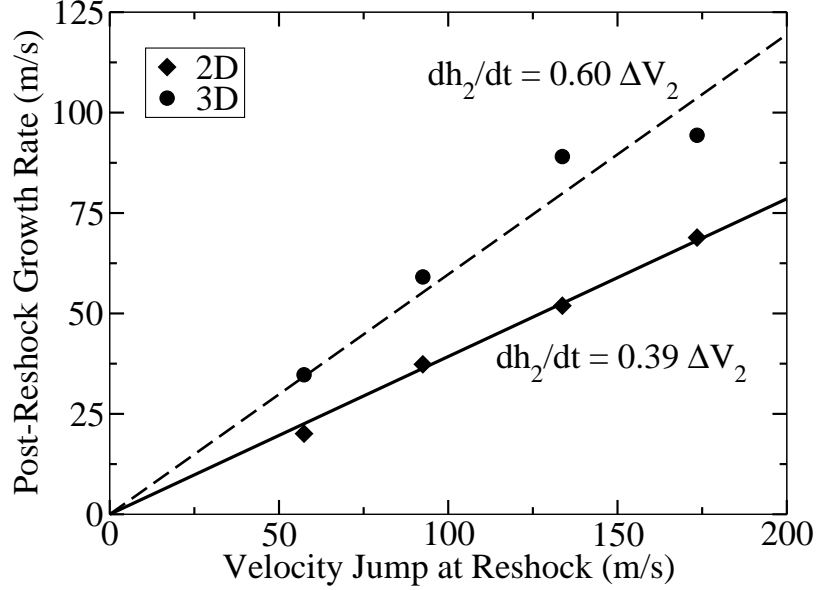


Figure 14: Correlation between mixing length growth rate and ΔV_2 . The regression line shows that the slope is 0.39 in 2D and 0.60 in 3D.

Comparisons to empirical models are performed. Using the formulation of Charakhch'an's model, which is appropriate for 2D single-mode RMI, the coefficient $\beta \approx 0.68$ within the range of $0.59 < \beta < 0.84$ is obtained in the current simulations. However, the original value proposed by Charakhch'an is nearly four times larger ($\beta \approx 2.5$ with the range of $1.06 < \beta < 3.0$). The difference is presumably from either the numerical scheme or the choice of species (Deuterium/Aluminum, but $A^+ = 0.69$ is in the same order as the present study) used in his study. Assuming a correlation similar to Mikaelian reshock model, the numerical study reveals $C \approx 0.56$ for 2D and $C \approx 0.84$ for 3D, that are larger than the originally proposed value. There is no experimental data available for validation yet. Schilling et al. [84] performed numerical analysis of 2D single-mode RMI with reshock and found similar correlations, $C \approx 0.56$ (however, the value of the slope identified in the title of their Fig. 9 [84] differs from the actual slope in their figure by a factor of two). Thus, both empirical models can be applied to the reshock models with proper coefficients.

The differences in the evolution of 2D (Case S2) and 3D (Case 3DS2) are presented

in Figs. 15 16 and 17. At 0.7 ms, the species interface creates the typical mushroom shape of the interface. The 3D case shows roll-ups for both bubble and spike fronts, instead of both bubbles and spikes sharing the same roll-up as in 2D. The difference is because that 2D RMI generates vortex lines, whereas 3D RMI create vortex rings around both bubbles and spikes. When the reshock hits the perturbation, the interface is distorted (0.8 ms), and the inversion of bubble and spike occurs as seen in Fig. 2 (0.9 ms) and show rapid growth at later times. Similar RMI evolution has been reported in past studies as well [13, 19, 42, 46, 53, 84].

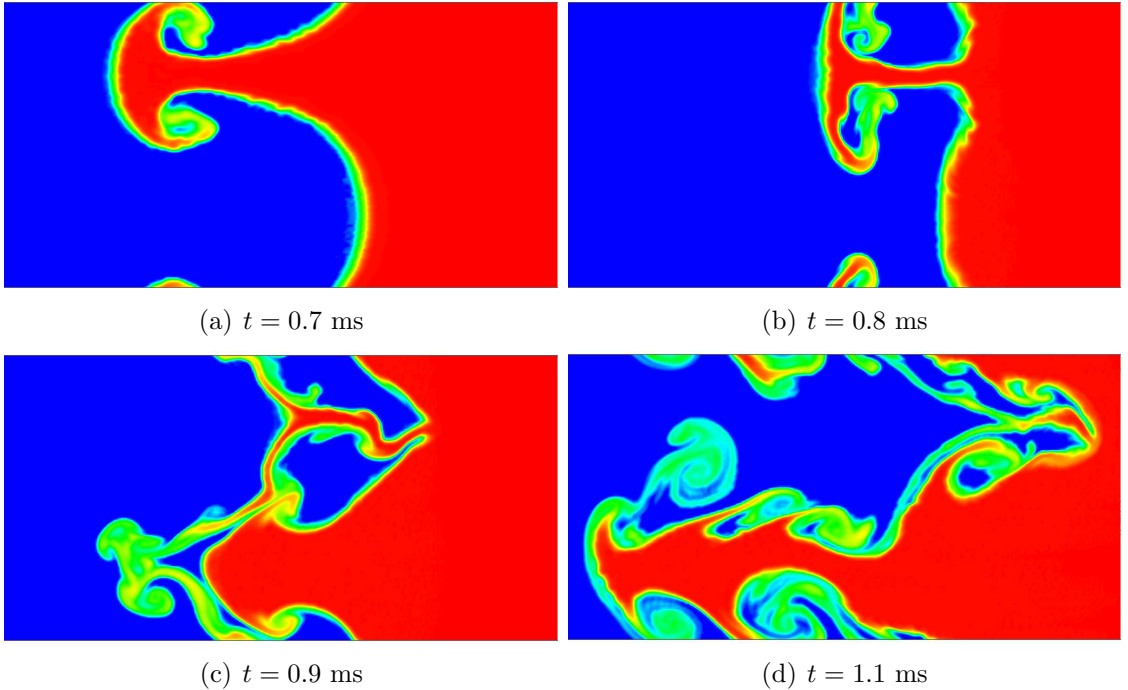


Figure 15: RMI interface shape colored by mass fraction of SF_6 (Case S2).

Even though the shape of RMI perturbation at reshock does not influence the post-reshock growth rate, the dimensionality of perturbation is an important factor as often discussed in classical reshock models [13, 71]. 3D single-mode results show $C \approx 0.84$ and $\beta \approx 1.02$, which are about 1.6 times larger than the values obtained from the 2D single-mode studies ($C \approx 0.52$ and $\beta \approx 0.63$). Although the differences in the post-reshock growth in 2D and 3D have not been analytically obtained, a couple

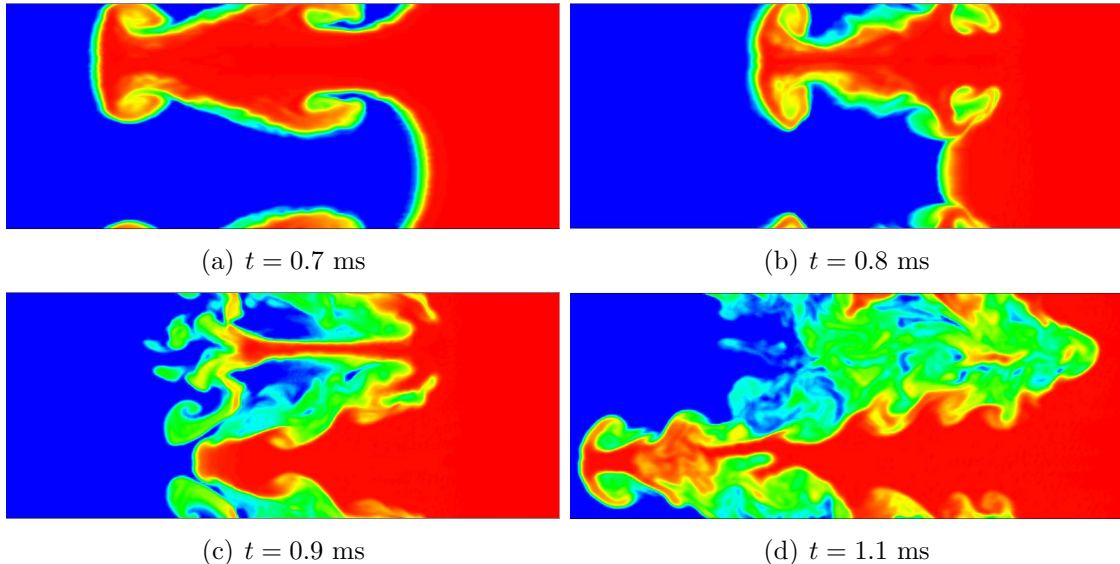


Figure 16: RMI interface shapes colored by mass fraction of SF_6 .

of possible reasons are briefly discussed here. First, the vortex stretching term in Eqn. (1) is activated in 3D flow, whereas this term is zero in 2D; this vortex stretching term can possibly strengthen the vorticity if the vortex rings are stretched in 3D. The other possible reason is due to the geometry of the perturbation. The 3D RMI will have a point contact to the shock at the bubble and spike fronts, whereas 2D RMI will have a line contact to the shock. Thus, it is possible for 3D RMI to have larger vorticities at fronts that can cause larger growth rates.

In summary, the parametric study of single-mode RMI shows that the post-reshock growth rate is independent of the wavelength and amplitude at reshock, and linearly correlated with ΔV_2 . However, the dimension of the perturbation is important and 3D cases result in 1.6 times larger growth rates than their counterpart 2D cases.

4.3 Parametric Studies of Multi-Mode RMI

Since single-mode RMI studies show that the growth rate is not a strong function of the interface geometry, the same reshock growth model should ideally be applicable to multi-mode RMI. In fact, Charakhch'an [14, 15] analyzed the post-reshock growth rates of the interface which consists of three segments of lines instead of a sinusoidal

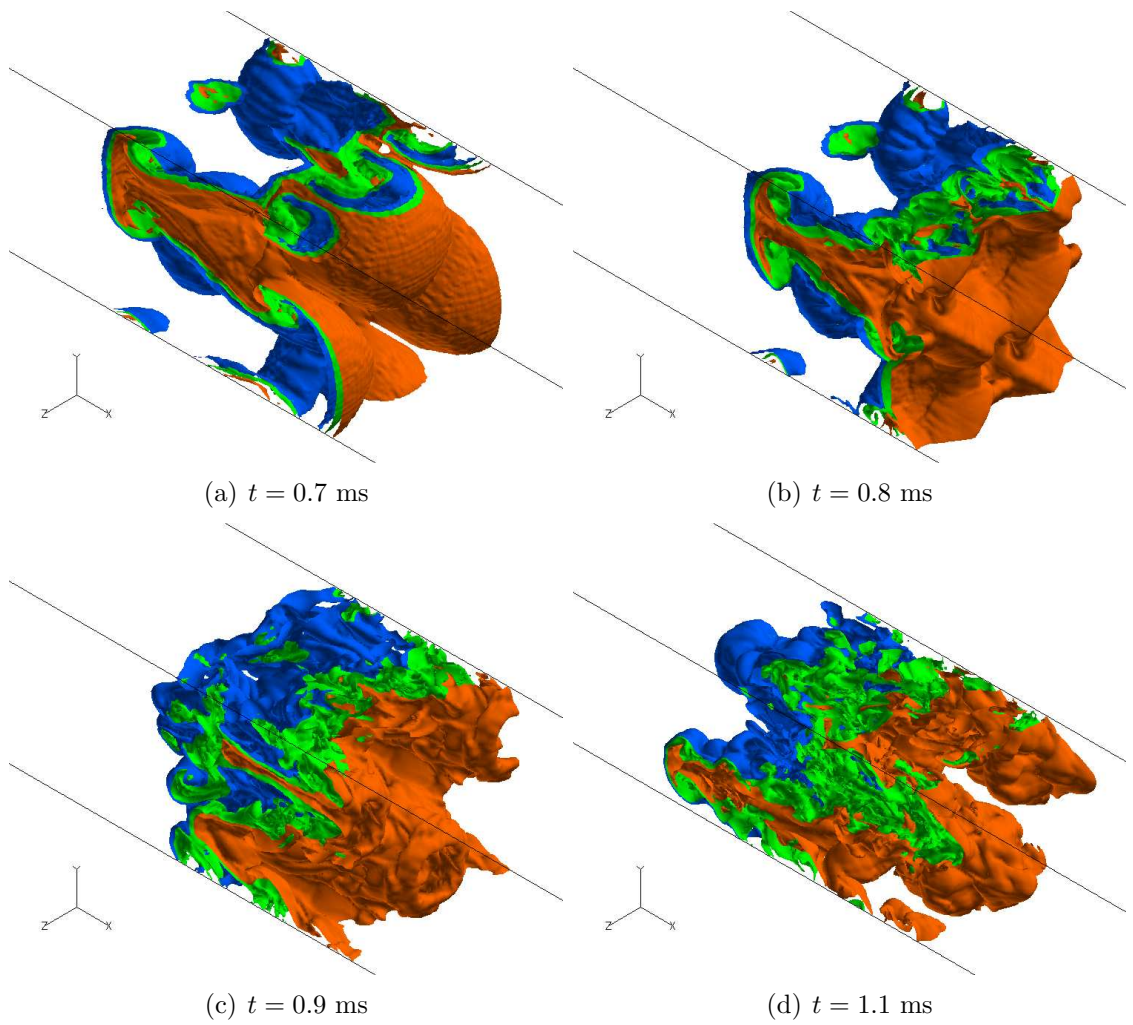


Figure 17: Iso-surfaces of species interface with different mass fractions of SF_6 (Blue-10%, Green-50%, Orange-90%).

wave, and demonstrated that his model was applicable to the case. However, the post-reshock growth rates of multi-mode RMI are smaller than single-mode cases in 2D and 3D, as shown in Sec. 4.1. Therefore, the growth rate is expected to depend also on the randomness of the initial perturbation. Here, the present study investigates the growth rate of multi-mode RMI in 2D and 3D with different initial amplitudes and wavenumbers. The values of $\frac{dh_2}{dt}$ and C obtained for each case are presented in Table 9.

Table 9: List of initial conditions and results for the 2D and 3D multi-mode RMI.

Case	Dimension	k_{max}	a_0 (mm)	R	Grid Size	$\frac{dh_2}{dt}$	C
M1	2D	2	2.0	0.4	2048×128	35.60	0.53
M2	2D	4	2.0	0.8	2048×128	11.98	0.18
M3	2D	8	2.0	1.6	2048×128	11.65	0.17
M4	2D	4	0.5	0.2	2048×128	32.50	0.49
M5	2D	4	1.0	0.4	2048×128	20.62	0.31
M6	2D	4	4.0	0.8	2048×128	13.28	0.20
M7	2D	4	8.0	1.6	2048×128	15.82	0.23
3DM1	3D	2	1.0	0.1	1024×64 ²	61.2	0.93
3DM2	3D	2	2.0	0.2	1024×64 ²	54.5	0.83
3DM3	3D	2	4.0	0.4	1024×64 ²	20.2	0.31
3DM4	3D	2	8.0	0.8	1024×64 ²	23.6	0.36
3DM5	3D	4	1.0	0.2	1024×64 ²	53.1	0.81
3DM6	3D	4	2.0	0.4	1024×64 ²	25.2	0.38
3DM7	3D	4	4.0	0.8	1024×64 ²	26.9	0.41
3DM8	3D	4	8.0	1.6	1024×64 ²	27.5	0.42

Analyzing the results, the post-reshock growth rates of multi-mode RMI show two different sets of solution based on the initial interface shapes. The first type of the solution is “rapid growth”, which is the post-reshock growth rate close to the single-mode RMI. For 2D multi-mode RMI study, small k_{max} and amplitude cases such as Case M1 and M4 show that the large post-reshock growth rate ($C \approx 0.52$) is comparable to the single-mode 2D RMI ($C \approx 0.56$). Similarly, the 3D cases show rapid growth with small amplitudes and wavenumbers (Case 3DM1, 3DM2 and 3DM5) with growth rate constant, $0.81 < C < 0.93$, comparable to the single-mode

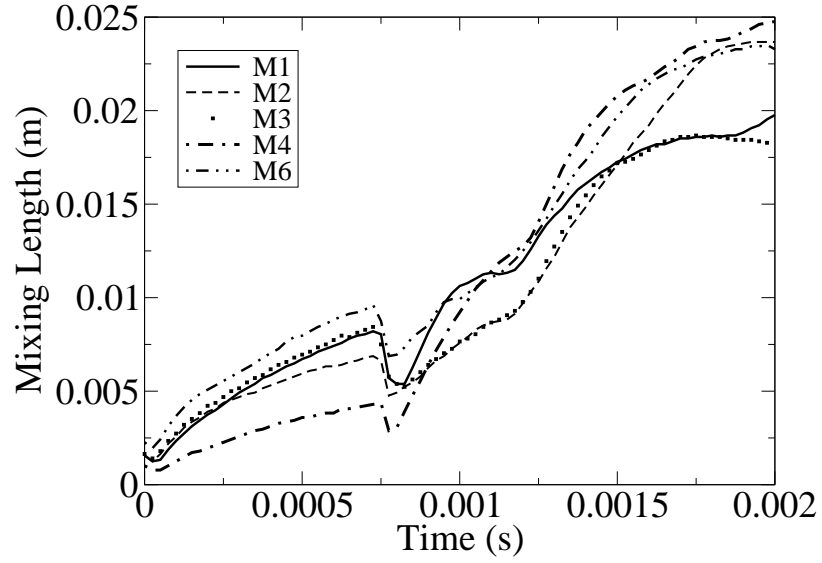
solution ($C \approx 0.90$). On the other hand, “slow growth” is seen when the initial interface shape is more random (larger a_0 and k_{max}). 2D cases result in $C \approx 0.2$ as seen in Cases M2, M3, M6 and M7, and 3D RMI cases show $0.31 < C < 0.42$. Thus, the slow-growth cases seem to have a value of C only about 40 % of the rapid-growth in both 2D and 3D studies, presented in Fig. 18. We define the randomness factor as:

$$R = \frac{a_0 k_{max}}{L_y}, \quad (101)$$

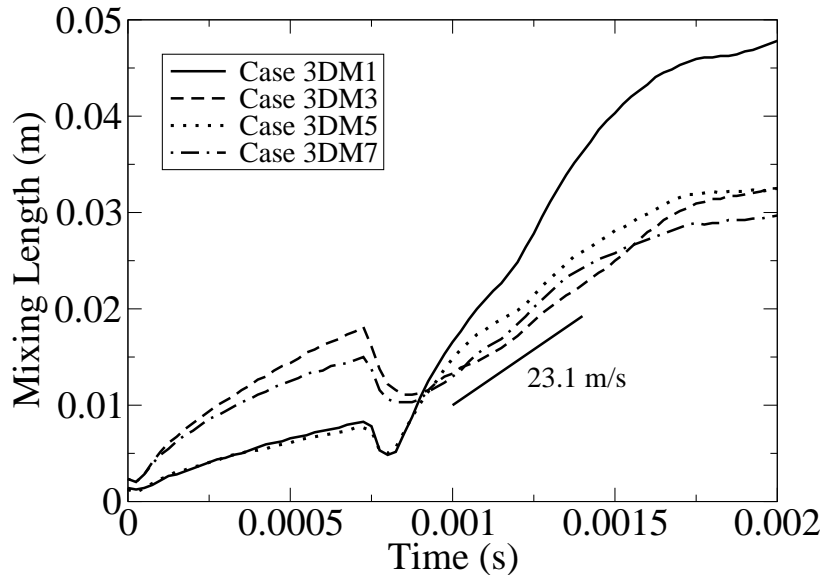
to quantify the initial perturbation. When R is small, the growth rates follow single-mode cases. In this study, for example, rapid-growth is likely to happen when $R \leq 0.4$ for 2D and $R \leq 0.2$ for 3D in the given domain configurations.

A fundamental question is to quantify the differences between rapid and slow growths. Past experiments [48] obtained the range of C as $0.33 < C < 0.44$ that agrees well with slow growth data sets ($0.31 < C < 0.42$) obtained from the numerical prediction. 2D simulations also show slower reshock growth rates in multi-mode, as also reported in a recent numerical study [37].

The time series of RMI evolution of rapid growth (Case M4) and slow growth (Case M2) are shown in Fig. 19. Since Case M4 has very small amplitude to begin with, the interface shape is still resolved at reshock, whereas Case M2 shows a well mixed interface. Thus, bubbles and spikes after reshock happen to grow as fast as the single-mode case, similar to the predictions of Charakhch’an [14, 15]. However, Case M2 shows complex mixing at the time of reshock, and bubbles and spikes carry lateral motion that cease the growth of the mixing length in the longitudinal direction but enhances the mixing of species. Similar behaviors of bubbles and spikes are seen in 3D as well, and are presented in Fig. 20. Thus, even though past experimental studies [26, 48, 93] have shown that the interface conditions do not influence the reshock, the randomness of the interface can play a significant role in the post-reshock growth



(a)



(b)

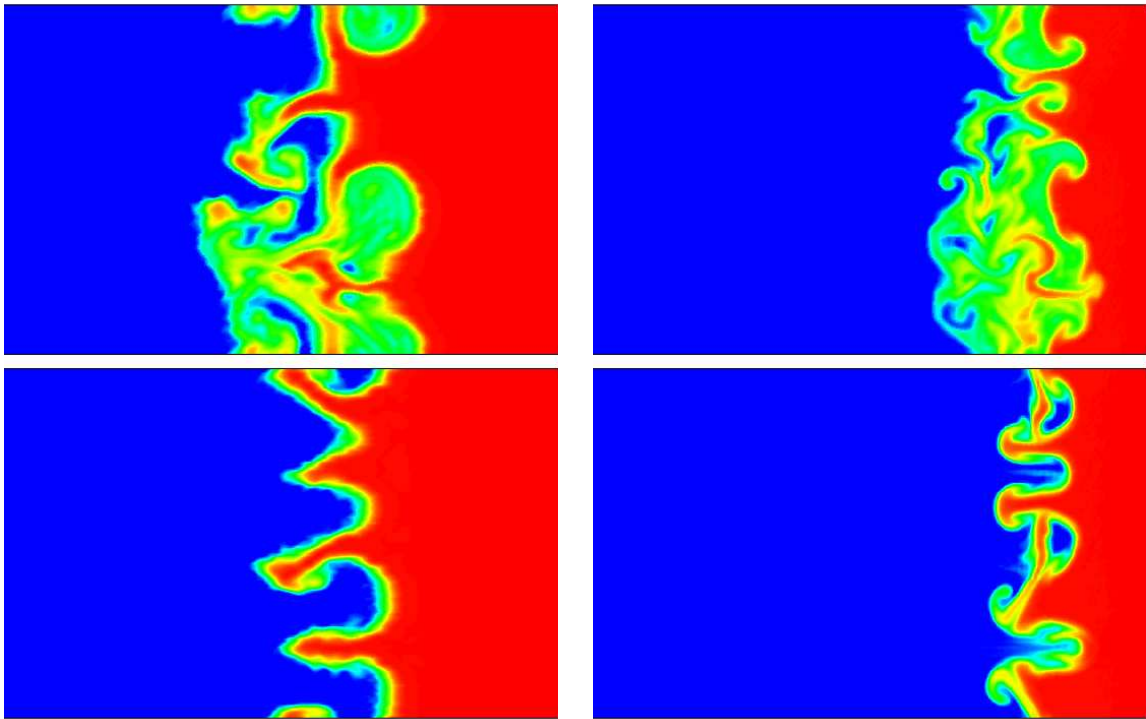
Figure 18: Mixing length growth of 2D (a) and 3D (b) multi-mode RMI with different initial conditions.

rates. When an experiment is performed with a flat-membrane, the real interface is inevitably random, and so the randomness criterion is usually satisfied.

The main reason for the differences in the growth rates between single- and multi-mode RMI is found to be the nature of the randomness of RMI. If a random interface is present at the time of reshock, the growth rate becomes very small due to the tangential motion of bubbles and spikes. However, if the interface shapes are sharp (small R), then, when reshock occurs, the growth rates are in the same order as the single-mode RMI.

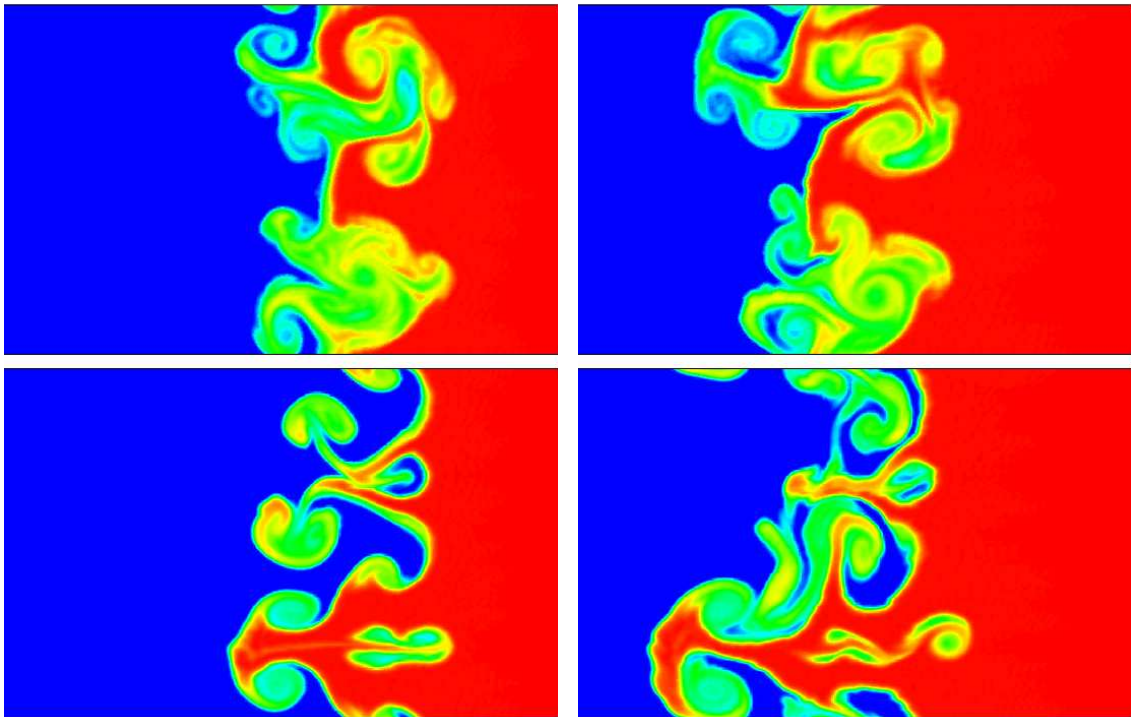
4.4 Conclusions of Reshocked RMI studies

In this chapter, the reshocked Richtmyer-Meshkov instabilities for four different classes of interface shapes are numerically studied. The initial domain configurations follow past shock tube experiments with air/ SF_6 species combinations, and the growth rates after the reshock are examined. The parametric studies of 2D/3D single-/multi-mode RMI are performed to investigate the effect of the initial conditions on the late time growth patterns. Single-mode RMI with different wavelengths and wall distances are analyzed to study the sensitivity of interface shapes at reshock, and it is found that growth rates after reshock are a weak function of the interface geometry. Linear correlations of the growth rates to ΔV_2 are found in both 2D and 3D, with higher growth rates for 3D. The value of the coefficient for Charakhch'an's formulation found in this study is about a quarter of the originally proposed value. Finally, parametric studies of multi-mode interfaces are performed. The post-reshock growth rates are in the same order as the single-mode RMI (so called "rapid growth") when the interface is not very random. As the initial amplitude and k_{max} increase, "slow growth" is observed. Furthermore, 3D RMI results in larger growth rates than 2D in multi-mode study as well, and are in agreement with previous experimental data [48]. Key results of the post-reshock growth rate studies can be summarized as:



(a) $t = 0.7$ ms

(b) $t = 0.8$ ms



(c) $t = 0.9$ ms

(d) $t = 1.0$ ms

Figure 19: Side view of interface evolution. Top - Case M2, Bottom - Case M4.

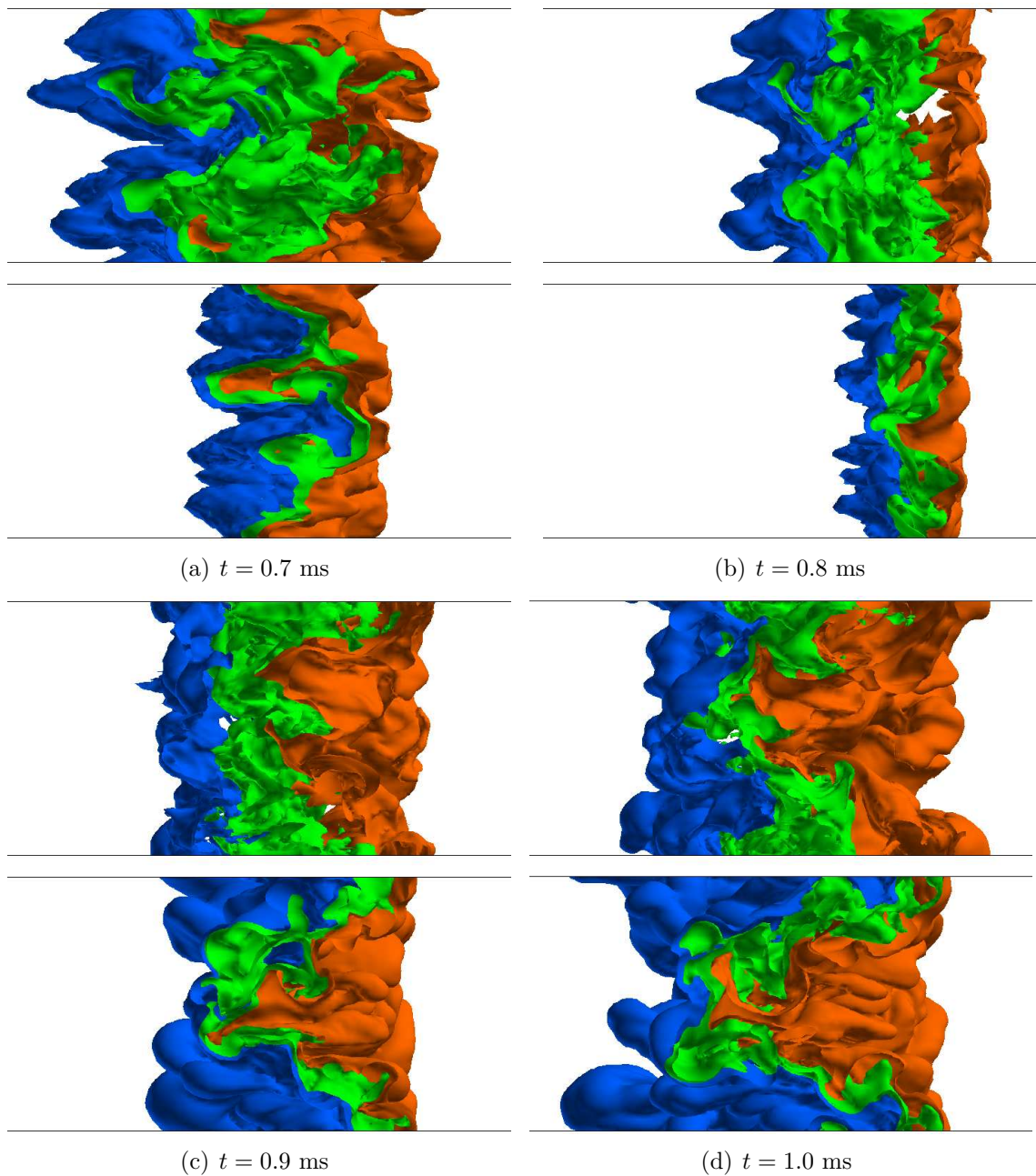


Figure 20: Side view of interface with different mass fraction of SF_6 (Blue-10%, Green-50%, Orange-90%). Top - Case 3DM7, Bottom - Case 3DM5.

- The numerical prediction of of 3D multi-mode experiment agrees with the past experimental results [48].
- The post-reshock growth rates of single-mode RMI in 2D and 3D are not a function of the perturbation geometry parameters such as a_r , λ and a/λ
- The post-reshock growth rate is linearly proportional to ΔV_2
- The post-reshock growth rates of multi-mode RMI shows rapid-growth if the interface remains sharp at reshock, and slow growth is observed if interface is mixed
- Reshock growth rate in 3D is about 1.6~1.9 times larger than 2D in both single- and multi-mode RMI.

This study suggests that the growth rates of each RMI configuration can be simply characterized by the Mikaelian’s reshock model (Eqn. 5) with different values of coefficient obtained by parametric studies shown in Table 10.

Table 10: The empirical values for the Mikaelian’s reshock model (C) extended for different interface configurations. Note that original model used $C = 0.28$ [62], and recent experimental study showed $C = 0.38$ for 3D multi-mode RMI [48]

	2D	3D
single-mode & multi-mode (sharp interface)	0.55	0.84
multi-mode (mixed interface)	0.20	0.38

CHAPTER V

MULTIPHASE RICHTMYER-MESHKOV INSTABILITY

This Chapter first discusses the derivation of the growth model of the multiphase RMI. Then, the model is compared against the numerical predictions under two types of configurations.

5.1 Amplitude Growth Model of Multiphase RMI

A growth model for two-phase RMI is obtained by following a similar approach but by employing the dusty-gas formulation [81] that assumes the volume fraction of particles are very small, and that the interaction between particles is neglected. The linear perturbation analysis is first used to obtain the growth rate of two-phase RTI following a past KHI study [60], and then the two-phase RMI growth rates are evaluated by the impulsive method [79].

The dusty gas equations for a mixture of gas and a pseudo-fluid of small particles can be written as:

$$\rho \left[\frac{\partial \mathbf{u}}{\partial t} + (\mathbf{u} \cdot \nabla) \mathbf{u} \right] = -\nabla p + \mu \nabla^2 \mathbf{u} + \kappa N (\mathbf{v} - \mathbf{u}) + \rho g \nabla z, \quad (102)$$

$$\nabla \cdot \mathbf{u} = 0, \quad (103)$$

$$mN \left[\frac{\partial \mathbf{v}}{\partial t} + (\mathbf{v} \cdot \nabla) \mathbf{v} \right] = \kappa N (\mathbf{u} - \mathbf{v}) + mg \nabla (Nz), \quad (104)$$

$$\frac{\partial N}{\partial t} + \nabla \cdot N \mathbf{v} = 0, \quad (105)$$

where \mathbf{u} is the gas velocity, \mathbf{v} is the velocity of the particles, p is the gas pressure, μ is the gas viscosity, ρ is the gas density, κ is the drag term, N is the number density of the particles, m is the mass of the particle, z is the height, and g is the driving

acceleration. Assuming the particles are spherical, $\kappa = 6\pi r_p \mu$ is used from Stokes' law [81], where r_p is the radius of particle. Note that the drag law used for the theoretical analysis is simpler than that used in the numerical simulation (Eqn. 27) in order to maintain linearity of the theoretical formulation.

Also, the pseudo-fluid formulation is incompressible since it is assumed that once the shock wave passes the interface, the flow is incompressible, as also assumed by Richtmyer [79]. First, the growth rate of the perturbation is studied in the configuration of Rayleigh-Taylor instability as shown in Fig. 21.

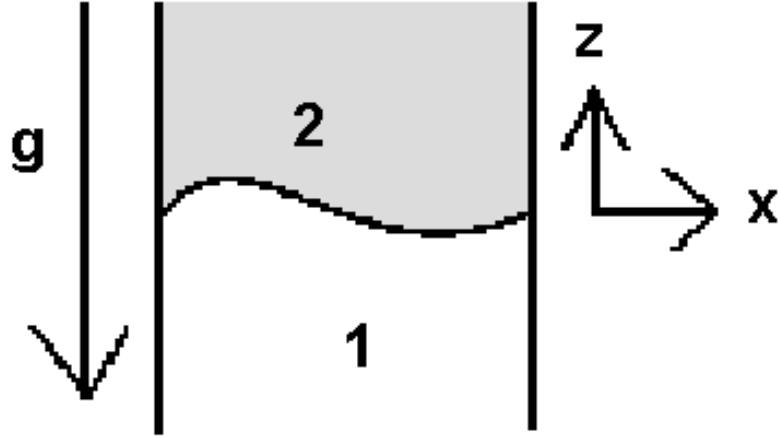


Figure 21: Initial configuration of Rayleigh-Taylor instability. Specie 2 (heavy gas) is on the top of species 1 (light gas) to initiate the instability

The equations are linearized by considering a small perturbation as follows:

$$\begin{aligned} \mathbf{u} &= \mathbf{U}_0 + \mathbf{u}', \mathbf{v} = \mathbf{U}_0 + \mathbf{v}', N = N_0 + N', \\ p &= p_0 + p', z = z_0 + a, \end{aligned} \tag{106}$$

Here \mathbf{U}_0 , N_0 , p_0 and z_0 are, respectively, the mean velocity, the number density, the pressure and the particle position. Note that \mathbf{U}_0 is the mean velocity only in the x-direction, and the mean particle velocity is equated to the gas velocity, U_0 as also assumed in the original papers [81, 60]. Also, z_0 is the reference height chosen

to be zero. \mathbf{u}' , \mathbf{v}' , N' and p' are the corresponding fluctuation of each parameter, and a is the amplitude of the perturbation. Each disturbance is represented by a wave of the form in 2D: $[\mathbf{u}'(x, z, t), \mathbf{v}'(x, z, t), N'(x, z, t), p'(x, z, t), a(x, t)] = [\hat{\mathbf{u}}(z), \hat{\mathbf{v}}(z), \hat{N}(z), \hat{p}(z), \hat{a}]e^{ik(x-ct)}$ [60, 81]. Here, all variables $\hat{\psi}$ are the complex amplitudes, k is the streamwise wavenumber and c is the complex phase velocity. Assuming small perturbations and inviscid conditions [23], Eqns. (102) and (104) are linearized as follows:

$$ik(U_0 - c)\hat{\mathbf{u}} = -ik\hat{p}/\rho + s(\hat{\mathbf{v}} - \hat{\mathbf{u}}) + ikg\hat{a}, \quad (107)$$

$$ik(U_0 - c)\hat{\mathbf{v}} = (\hat{\mathbf{u}} - \hat{\mathbf{v}})/\tau + ikg\hat{a}. \quad (108)$$

Here, $s = \kappa N_0/\rho$ and $\tau = m/\kappa$. Note that s has a unit of frequency, τ is the particle response time with the unit of time.

In Eqn. (109), \hat{p} is obtained by a function of $\hat{\mathbf{u}}$ by combining Eqns. (107) and (108) [60, 81]:

$$(U_0 - c) \left[1 + \frac{\tau s}{1 + ik\tau(U_0 - c)} \right] \hat{\mathbf{u}} = -\hat{p}/\rho + \left[1 + \frac{\tau s}{1 + ik\tau(U_0 - c)} \right] g\hat{a}. \quad (109)$$

Here, the velocity potential is defined as $\nabla\phi = U_0 + \nabla\phi'$, where the perturbed velocity is $\nabla\phi' = \mathbf{u}'$. Since ϕ' can also be represented by a disturbance of the form $\phi'(\mathbf{x}, t) = \hat{\phi}(z)e^{ik(x-ct)}$, the expression for \hat{p} is found as:

$$\hat{p} = \rho \left[1 + \frac{\tau s}{1 + ik\tau(U_0 - c)} \right] [g\hat{a} - ik(U_0 - c)\hat{\phi}]. \quad (110)$$

The boundary conditions are taken at the far field and species interface. First, the velocity potentials in each species are defined as:

$$\phi' = \begin{cases} \phi'_2 & z > a \\ \phi'_1 & z < a \end{cases}, \quad (111)$$

Here, subscripts 1 and 2 correspond to the light and heavy gases, respectively. At the far field, the disturbance is zero, so that the following far field conditions are taken:

$$\begin{aligned}\phi'_2(\infty) &= 0, \\ \phi'_1(-\infty) &= 0.\end{aligned}\tag{112}$$

Since $\Delta\phi'_j = 0$ (where the subscript j indicates the specie 1 or 2), ϕ'_j are found as:

$$\begin{aligned}\phi'_2 &= \beta e^{kz}, \\ \phi'_1 &= \alpha e^{-kz}.\end{aligned}\tag{113}$$

Two boundary conditions at the interface are enforced [23, 60]. First, the fluid motion at the interface is given as:

$$\frac{\partial\phi'_j}{\partial z} = \frac{\partial a}{\partial t} + U_j \frac{\partial a}{\partial x}.\tag{114}$$

From Eqns. (112) - (114), α and β are found:

$$\begin{aligned}\beta &= i(U_2 - c)a, \\ \alpha &= -i(U_1 - c)a.\end{aligned}\tag{115}$$

Also, the pressure at the species interface is continuous (i.e. $\hat{p}_1(a) = \hat{p}_2(a)$):

$$\begin{aligned}\hat{p} &= \rho_1 \left[1 + \frac{\tau_1 s_1}{1 + ik\tau_1(U_1 - c)} \right] [g\hat{a} - ik(U_1 - c)\hat{\phi}_1] \\ &= \rho_2 \left[1 + \frac{\tau_2 s_2}{1 + ik\tau_2(U_2 - c)} \right] [g\hat{a} - ik(U_2 - c)\hat{\phi}_2].\end{aligned}\tag{116}$$

Combining Eqns. (115) and (116), and approximate $\hat{\phi}$ on the interface by first order (i.e. $e^{ka} \approx 1.0$; $e^{-ka} \approx 1.0$):

$$\begin{aligned}\rho_1 \left[1 + \frac{\tau_1 s_1}{1 + ik\tau_1(U_1 - c)} \right] [g - k(U_1 - c)^2] &= \\ \rho_2 \left[1 + \frac{\tau_2 s_2}{1 + ik\tau_2(U_2 - c)} \right] [g + k(U_2 - c)^2],\end{aligned}\tag{117}$$

which is a general expression for instability applicable for KHI, RTI and RMI. Note that Eqn. (117) becomes the same expression derived by Michael [60] if $\rho_1 = \rho_2$ and

$g = 0$. Since flow in RTI and RMI is initially at rest, $U_1 = U_2 = 0$ is applicable in Eqn. (117), and the following equation is obtained for a two-phase RTI or RMI:

$$\rho_1 \left[1 + \frac{f_1}{1 - ik\tau_1 c} \right] (g - kc^2) = \rho_2 \left[1 + \frac{f_2}{1 - ik\tau_2 c} \right] (g + kc^2), \quad (118)$$

where f_1 and f_2 are respectively, the mass loading in light and heavy gases given by $f_i = mN_0/\rho_i = \tau_i s_i$. Since the analytical expression presented in Eqn. (118) is difficult to solve, the small $k\tau c$ limit ($|k\tau c| \ll 1.0$) is assumed to simplify Eqn. (118) to:

$$\rho_1 [1 + f_1] (g - kc^2) = \rho_2 [1 + f_2] (g + kc^2). \quad (119)$$

Then, the wave speed is obtained as:

$$c^2 = \frac{g \rho_1 (1 + f_1) - \rho_2 (1 + f_2)}{k \rho_1 (1 + f_1) + \rho_2 (1 + f_2)} = -\frac{g}{k} A_m, \quad (120)$$

where the multiphase Atwood number, A_m is defined as:

$$A_m = \frac{\rho_2 (1 + f_2) - \rho_1 (1 + f_1)}{\rho_2 (1 + f_2) + \rho_1 (1 + f_1)}. \quad (121)$$

Note that the real part of c is found to be zero from Eqn. (120), as also seen in the Rayleigh-Taylor instability analysis [23]. Also, A_m becomes identical to the Atwood number used in the original model if there are no particles (i.e. $f_1 = f_2 = 0$). The impulsive model [79] assumes that the fluid interface for RMI is accelerated impulsively as:

$$\int g(t) dt = \Delta V. \quad (122)$$

Here, the impulsive model assumes that the particles and the local fluid obtain the same amount of the velocity change, ΔV . A useful parameter to verify this assumption is the Stokes number, St which is the ratio of the particle response time and the

flow time [51]. Here, the flow time scale of RMI is chosen based on the initial growth rate, and St is defined as:

$$St = \frac{\tau}{\tau_{RMI}}. \quad (123)$$

The time scale for RMI is defined as $\tau_{RMI} = a_0/v$, where a_0 is the initial amplitude of the perturbation and v is the initial RMI growth rate. When $St \ll 1.0$, the particles can catch up with the local velocity very quickly and so that the assumption of the impulsive model is valid, whereas particles do not respond while the RMI is evolving if $St \gg 1.0$ [51]. The acceleration of the interface motion can be described by the following differential equation [79]:

$$\frac{d^2 a(t)}{dt^2} = -a(t)k^2 c^2. \quad (124)$$

If the small $k\tau c$ assumption is invoked, c^2 in Eqn. (124) can be substituted by Eqn. (120) resulting in:

$$\frac{d^2 a(t)}{dt^2} = a(t)g(t)kA_m. \quad (125)$$

Applying the impulsive model and integrating in time, the following linear growth model for multiphase RMI is obtained:

$$\left. \frac{da(t)}{dt} \right|_{t=0} = -ikca_0 = v_{0,m}, \quad (126)$$

$$a(t) = v_{0,m}t + a_0, \quad (127)$$

where $v_{0,m} = a_0 k A_m \Delta V$ is the multiphase Richtmyer velocity. Note that if there are no particles ($f_1 = f_2 = 0$), this formulation reduces to the original Richtmyer's model (Eqn. 2). The wave speed, c is obtained as $c = -v_{0,m}/(ika_0)$, so that small $k\tau c$ limit can be described as:

$$-ik\tau c = \frac{\tau}{a_0/v_{0,m}} = \frac{\tau}{\tau_{RMI}} = St. \quad (128)$$

Thus, the model indicates that the initial multiphase RMI growth can be described by only two extra parameters for multiphase flow: f and St , i.e., particle loading, and how soon the particles can respond to the flow.

In summary, the two-phase RMI growth model asymptotes to the classical RMI model in the absence of particles. In the presence of particles, to obtain a modified growth model, following assumptions are necessary:

1. Volume fraction of particles is small, so collision effects are neglected (dusty gas formulation);
2. The particle shape is spherical and Re_d is small; thus the drag law is approximated simply by Stokes' law;
3. $St \ll 1.0$ to apply the impulsive model and to simplify Eqn. (118).

5.2 *Results*

First, the case with shock driven RMI on an air/ SF_6 interface surrounded by particles is discussed, followed by studies of a shock interaction with a perturbed cloud of solid particles. Since the multiphase growth model and the numerical scheme treat the particle phase differently, the numerical setup is chosen to satisfy the assumptions of the dusty-gas formulation to enable direct comparisons. Thus, dilute mono-dispersed particle distribution is used in the following numerical studies.

5.2.1 **Results for Air/ SF_6 interface surrounded by particles**

Here, the 2D single-mode air/ SF_6 RMI surrounded by a large number of particles is analyzed. The domain configuration similar to the reshock study used in the previous section is chosen and is shown in Fig. 22. The streamwise length is $L_x = 16$ cm, and the transverse length is 1 cm. The shock, the dusty gas front, and the perturbed species interface are located at 13 cm, 9 cm and 8 cm, respectively, from the end wall. The incident Mach number is 1.2, and SF_6 and air characterize the initial species

interface with a 2D single-mode perturbation as Eqn. 97 [19] with $a_0 = 0.5$ mm, and λ is equal to the domain height. Spherical particles with a density of 780 kg/m^3 are uniformly distributed along computational cells in the grey region shown in Fig. 22. The amplitude of the perturbation is measured as the half length of the iso-contour of the mass fraction at the species interface [12, 91].

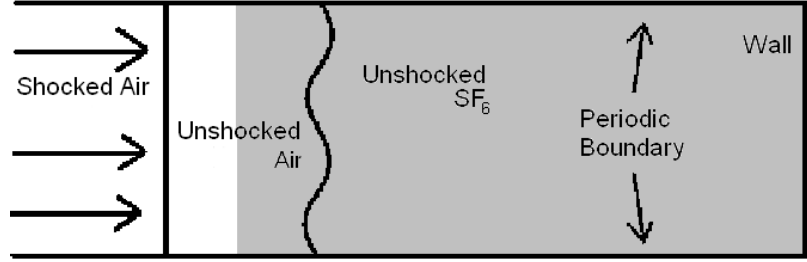


Figure 22: Initial configuration of RMI in a perturbed species interface surrounded by a cloud of solid particles. The grey region denotes the region filled with the gas-particle mixture.

Parametric studies of RMI particle interactions with different values of f_1 , f_2 , τ_1 and τ_2 are analyzed by changing the particle sizes and number density. Eight different particle sizes corresponding to four different mass loadings are simulated. The parameters of different cases, the predictions by the original RMI growth model, the multiphase RMI growth model, and the numerical predictions are in Tables. 11 and 12. Note that τ is computed from the properties after the incident shock passes the interface, and f is computed by also considering the compression of number density of particles due to the incident shock.

The effects of grid resolution and parcel distribution are presented in Fig. 23. The amplitudes without particles are numerically obtained using two different grid sizes (1024×64 and 2048×128), and they show good agreement. Thus, the 1024×64 grid is used for the remainder of this study. Also, the number of parcels required per cell (and the number of particles per parcel to be assigned) has been investigated. For example, two distributions of parcels with the condition of Case 0.5-1 are compared, and this represents the baseline case. In one case, 64 parcels in the y -direction are distributed

Table 11: List of parameters for the first study.

Case	r_p (μm)	f_1	f_2	τ_1 (s)	τ_2 (s)
0.5-1	0.5	0.88	0.17	2.09×10^{-6}	2.79×10^{-6}
0.5-2	0.5	1.75	0.34	2.09×10^{-6}	2.79×10^{-6}
0.5-3	0.5	4.34	0.84	2.09×10^{-6}	2.79×10^{-6}
0.5-4	0.5	8.69	1.71	2.09×10^{-6}	2.79×10^{-6}
1.0-1	1.0	0.70	0.14	8.37×10^{-6}	1.11×10^{-5}
1.0-2	1.0	1.41	0.27	8.37×10^{-6}	1.11×10^{-5}
1.0-3	1.0	3.53	0.68	8.37×10^{-6}	1.11×10^{-5}
1.0-4	1.0	6.95	1.38	8.37×10^{-6}	1.11×10^{-5}
2.0-1	2.0	0.61	0.11	3.35×10^{-5}	4.47×10^{-5}
2.0-2	2.0	1.21	0.22	3.35×10^{-5}	4.47×10^{-5}
2.0-3	2.0	2.94	0.54	3.35×10^{-5}	4.47×10^{-5}
2.0-4	2.0	5.65	1.08	3.35×10^{-5}	4.47×10^{-5}
4.0-1	4.0	0.52	0.09	1.34×10^{-4}	1.79×10^{-4}
4.0-2	4.0	1.04	0.18	1.34×10^{-4}	1.79×10^{-4}
4.0-3	4.0	2.51	0.45	1.34×10^{-4}	1.79×10^{-4}
4.0-4	4.0	4.57	0.91	1.34×10^{-4}	1.79×10^{-4}
8.0-1	8.0	0.22	0.07	5.36×10^{-4}	7.16×10^{-4}
8.0-2	8.0	0.44	0.14	5.36×10^{-4}	7.16×10^{-4}
8.0-3	8.0	1.13	0.34	5.36×10^{-4}	7.16×10^{-4}
8.0-4	8.0	2.27	0.69	5.36×10^{-4}	7.16×10^{-4}
16.0-1	16.0	1.99	0.50	2.14×10^{-3}	2.86×10^{-3}
16.0-2	16.0	4.04	1.01	2.14×10^{-3}	2.86×10^{-3}
16.0-3	16.0	10.33	2.59	2.14×10^{-3}	2.86×10^{-3}
16.0-4	16.0	20.90	4.88	2.14×10^{-3}	2.86×10^{-3}
32.0-1	32.0	1.97	0.44	8.58×10^{-3}	1.14×10^{-2}
32.0-2	32.0	4.01	0.90	8.58×10^{-3}	1.14×10^{-2}
32.0-3	32.0	10.33	2.30	8.58×10^{-3}	1.14×10^{-2}
32.0-4	32.0	21.41	4.84	8.58×10^{-3}	1.14×10^{-2}
64.0-1	64.0	2.16	0.38	3.43×10^{-2}	4.58×10^{-2}
64.0-2	64.0	4.31	0.76	3.43×10^{-2}	4.58×10^{-2}
64.0-3	64.0	10.97	1.97	3.43×10^{-2}	4.58×10^{-2}
64.0-4	64.0	22.32	4.07	3.43×10^{-2}	4.58×10^{-2}

Table 12: Results of growth rate obtained from the numerical simulation and theoretical models. Stokes number, St is computed based on the initial growth rate obtained from the numerical results, $v_{0,num}$. Thus, $St_1 = kv_{0,num}\tau_1$.

Case	ΔV	$v_{0,num}$	A	v_0	$\frac{v_{0,num}}{v_0}$	A_m	$v_{0,m}$	$\frac{v_{0,num}}{v_{0,m}}$	St_1
No particle	68.5	10.46	0.71	12.15	0.86				
0.5-1	65	8.00	0.71	11.53	0.69	0.57	9.24	0.87	4.19×10^{-2}
0.5-2	62	6.28	0.71	10.99	0.57	0.48	7.44	0.84	3.29×10^{-2}
0.5-3	55	3.53	0.71	9.21	0.38	0.34	4.40	0.80	1.97×10^{-2}
0.5-4	47	1.88	0.71	7.36	0.26	0.25	2.58	0.73	1.13×10^{-2}
1.0-1	66	8.82	0.70	11.66	0.76	0.59	9.72	0.91	0.18
1.0-2	63	7.33	0.71	11.17	0.66	0.51	8.05	0.91	0.15
1.0-3	57	4.27	0.71	10.16	0.42	0.37	5.33	0.80	8.95×10^{-2}
1.0-4	51	2.31	0.71	8.87	0.26	0.28	3.44	0.67	4.96×10^{-2}
2.0-1	66	8.90	0.70	12.13	0.73	0.60	10.3	0.86	0.72
2.0-2	64	7.48	0.71	12.77	0.59	0.52	9.47	0.79	0.56
2.0-3	59	4.51	0.71	12.08	0.37	0.39	6.69	0.67	0.33
2.0-4	53	2.38	0.71	10.65	0.22	0.30	4.47	0.53	0.18
4.0-1	67	9.45	0.70	11.83	0.80	0.61	10.25	0.92	3.17
4.0-2	65	8.42	0.70	11.48	0.73	0.54	8.77	0.96	2.82
4.0-3	61	5.60	0.70	10.77	0.52	0.41	6.22	0.90	1.88
4.0-4	55	3.68	0.70	9.71	0.38	0.32	4.47	0.82	1.23
8.0-1	67	9.94	0.70	11.83	0.84	0.67	11.22	0.89	13.3
8.0-2	66	9.31	0.70	11.65	0.80	0.64	10.58	0.88	12.4
8.0-3	62	7.96	0.70	10.97	0.73	0.57	8.85	0.90	10.6
8.0-4	57	6.46	0.70	10.07	0.64	0.49	7.09	0.91	8.66
16.0-1	60	8.65	0.70	10.53	0.82	0.48	7.17	1.21	46.3
16.0-2	54	7.11	0.70	9.44	0.75	0.38	5.17	1.38	38.1
16.0-3	43	4.84	0.70	7.53	0.64	0.28	3.00	1.61	25.9
16.0-4	34	2.77	0.69	5.86	0.47	0.18	1.53	1.80	14.8
32.0-1	67	9.76	0.70	11.75	0.83	0.46	7.78	1.25	209
32.0-2	65	8.95	0.70	11.39	0.79	0.36	5.86	1.53	191
32.0-3	61	7.25	0.69	10.59	0.68	0.23	3.52	2.06	155
32.0-4	54	5.51	0.69	9.27	0.59	0.16	2.18	2.52	118
64.0-1	67	10.27	0.70	11.81	0.87	0.43	7.18	1.43	881
64.0-2	65	9.98	0.70	11.42	0.87	0.30	4.97	2.01	856
64.0-3	58	9.01	0.70	10.14	0.89	0.16	2.34	3.86	773
64.0-4	56	7.90	0.69	9.74	0.81	0.09	1.24	6.39	677

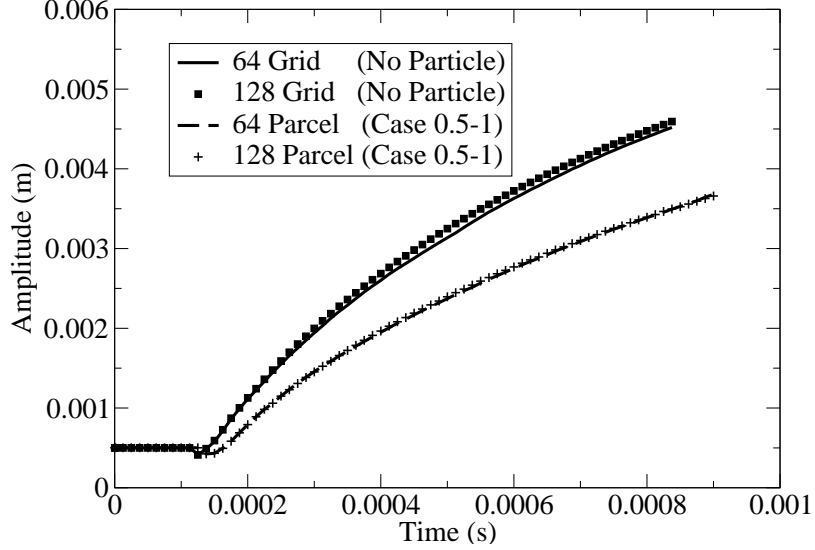


Figure 23: Comparison of the effect of the assigned number of parcels to the amplitude growth. ‘64 Grid’ and ‘128 Grid’ corresponds to the grid size in the y -direction. The legend ‘64 Parcel’ indicates the case with 64 parcels initialized in the y -direction (i.e., initially one parcel per cell), and ‘128 Parcel’ uses 128 parcels in the y -direction, with the distance between parcels being half of the ‘64 Parcel’ case (i.e., 128 corresponds to four parcels per cell initially.)

evenly in the x -direction; therefore, one parcel is allocated per cell. The other case uses 128 parcels in the y -direction, with equal inter-particle spacing maintained also in the x -direction; this case corresponds to four parcels initially allocated per cell. As evident from Fig. 23, both these cases show nearly identical growth rates, thereby exemplifying that 64 parcels suffice in the y -direction for the chosen dimensions. Thus, for the rest of this study, 64 parcels are initialized in the y -direction, and the same inter-particle spacing in the x -direction are also used.

The flow visualizations of different sizes of particles around RMI interfaces are presented in Fig. 24, with Case 0.5-1 in the first row, Case 4.0-1 in the second row, and Case 64.0-1 in the third row. All the three cases show very different particle distributions at later times, and can be characterized by Stokes number. In general, past studies have shown that particles cluster at regions with low vorticity [28, 85] if $St \approx 1.0$. On the other hand, if St is very large, particles do not easily respond to the fluid motion, whereas small St results in particles following the fluid motion

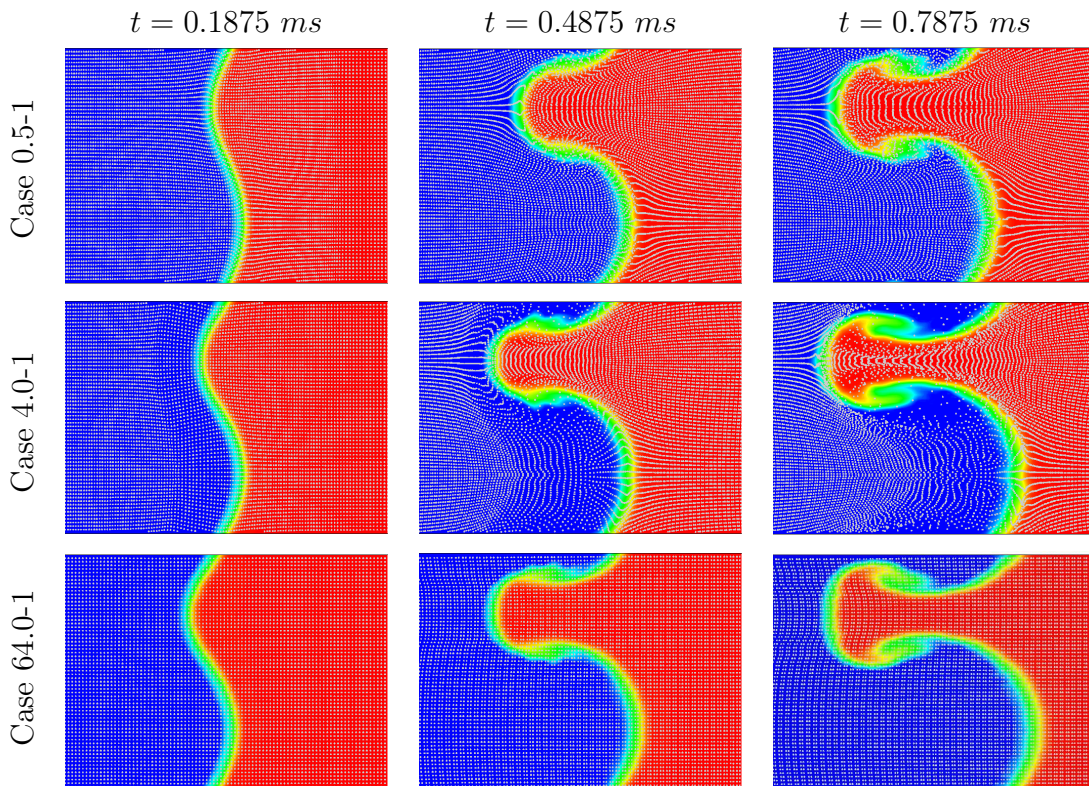


Figure 24: Contour of mass fraction of SF_6 with particle distribution (white dots). The first row corresponds to $St \ll 1.0$ (Case 0.5-1), the second row to $St \approx 1.0$ (Case 4.0-1), and the third row to $St \gg 1.0$ (Case 64.0-1).

very closely; hence, preferential concentration of particles does not occur in either of these cases [51]. Case 4.0-1 shows that the particles avoid the hydrodynamic roll-ups, and particle clustering is seen in the spikes since the Stokes number for this case is the order of 1.0 ($St \approx 3.0$). However, the Case 0.5-1 shows that the particles distribute even within the roll-ups, since Stokes number is very low ($St \approx 0.04$) and the particles inevitably follow the flow. On the other hand, Case 64.0-1 shows that the particles barely disperse since the Stokes number is very large ($St \approx 880$). These observations are similar to the findings of Ling et al. [51], who investigated particle cloud interaction with temporal mixing layers.

In Table 12, both single-phase and multiphase RMI growth models are compared with the numerical predictions. The growth rate without particles (denoted as ‘No particle’) obtained from the numerical simulation, $v_{0,num}$ is slightly smaller than the classical Richtmyer velocity, v_0 ($v_{0,num}/v_0 = 0.86$) due to the Richtmyer’s model over-predicting the growth rate, as also reported by Latini et al. [46] The numerical prediction of Case 0.5-X (where X denotes 1, 2, 3 and 4) shows good agreement with the multiphase Richtmyer velocity (Eqn. 127) since the particle response time is very small and the model assumptions are valid (e.g. $St \ll 1.0$).

The growth rate of the series of Case 0.5-X and the ‘No particle’ cases are examined in Fig. 25. As the particle loading increases, the initial growth rate decreases since both A_m and ΔV decrease as the mass loading increases. In Fig. 26, the same amplitude is normalized and presented (note that the multiphase Richtmyer velocity is used). The normalized growth rate shows good agreement in the early stage; for example, Case 0.5-1 follows nearly exactly up to $kv_{0,m}t < 1$, but starts to depart from the ‘No particle’ case eventually (Fig. 26). The reason for the different late-time growth may be the non-uniform distributions of particles, which occurs when the perturbations grow larger at late times. Due to the non-uniform distribution of particles around the hydrodynamic structures as shown in Fig. 24, the late time

growth rate of the perturbation will be different from the ‘No particle’ case.

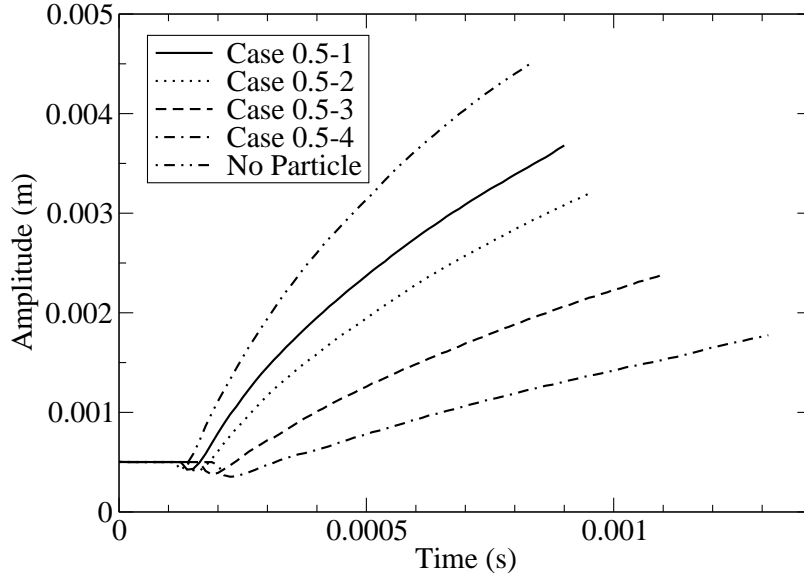


Figure 25: Amplitude growth for small particles with different mass loadings (Case 0.5-X) and the ‘No particle’ case.

The multiphase RMI model also shows a better prediction than the original Richtmyer model up to Case 8.0-X ($r_p \leq 8.0 \mu m$). It is unexpected to see that Case 4.0-X and Case 8.0-X follow the multiphase RMI model well since $St > 1.0$ for these cases and the assumptions of the multiphase RMI are not valid. However, numerical predictions show very good agreement with the multiphase RMI model. It could presumably be due to non-linear fluid-particle interactions, but more general theoretical models could be developed in the future to explain the phenomena more precisely. However, for much larger particles ($r_p \geq 16.0 \mu m$, $St \gg 1.0$) the two-phase model is inapplicable, and the original Richtmyer velocity shows better predictions. This makes sense since the original RMI is for single-phase flow. In fact, Case 64.0-X follows the original Richtmyer velocity very closely since the particles are not significantly influenced during the RMI growth process. Owing to their higher inertia, these particles have $St \approx 800$. Furthermore, changing the mass loading does not influence the growth rate as much as the small particle cases shown in Fig. 27, since inter-phase

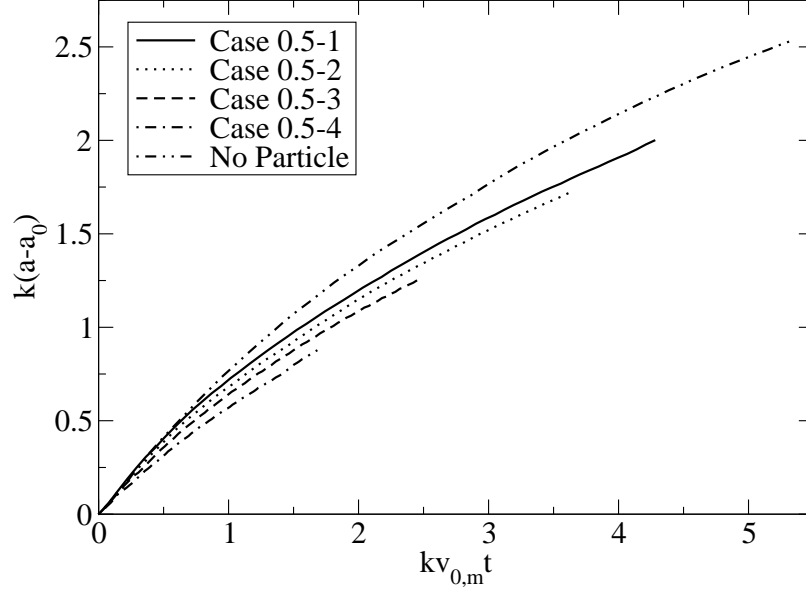


Figure 26: Normalized amplitudes for Case 0.5-X and the ‘No particle’ cases. The x -axis is normalized by the multiphase Richtmyer velocity.

momentum exchange is not very significant. The growth profiles normalized by the original Richtmyer velocity are nearly identical up to $kv_0t = 2.0$ including the ‘No particle’ case as shown in Fig. 28, indicating that the presence of particles does not influence the perturbation growth when $St \gg 1.0$.

In summary, results for a RMI surrounded by a uniform distribution of particles suggest that when the particle response time is relatively small ($St \ll 1.0$), the growth rates agree very well with the multiphase Richtmyer velocity. However, when the particle response time is very large ($St \gg 1.0$), the particles are not influenced by the fluid, and the amplitude growth follows the original Richtmyer velocity. Thus, the particle response time is a very important factor to control the applicability of both the current multiphase growth model as well as the original Richtmyer’s growth model. In the next section, the second RMI problem involving the perturbed shape particle cloud in air is analyzed.

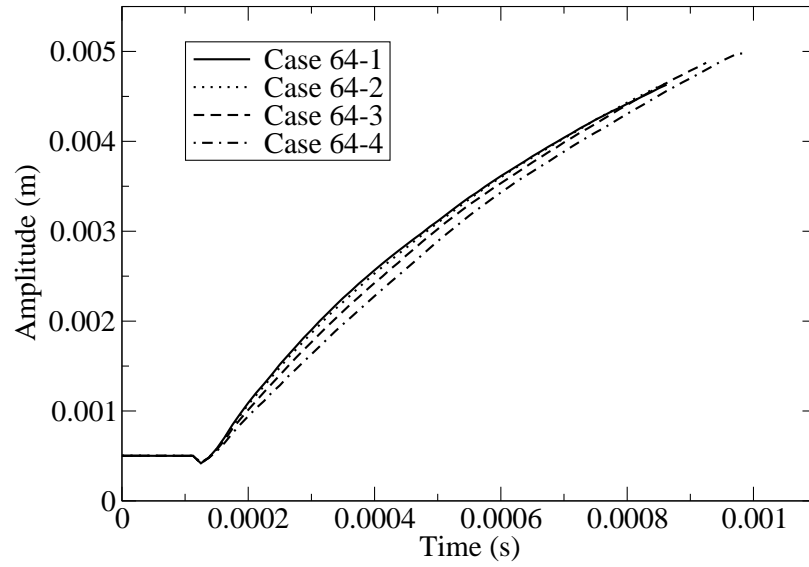


Figure 27: Amplitude growth for large particles with different mass loadings (Case 64.0-X).

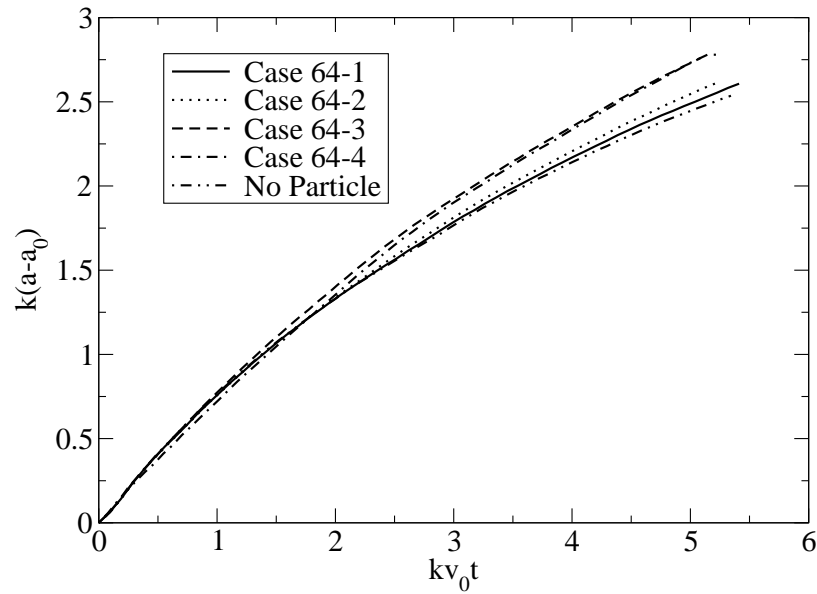


Figure 28: Normalized amplitudes for Case 64.0-X and the 'No particle' cases. The x -axis is normalized by the singlephase Richtmyer velocity.

5.2.2 Results for perturbed shape particle cloud

In this section, the RMI is investigated for a shock wave interaction with a cloud of solid particles with a perturbed shape in air instead of a heavy gas (such as SF_6). A schematic of the setup is presented in Fig. 29. The dusty gas front and the shock front are placed 8 and 9 cm from the end wall, respectively, and the initial amplitude of the perturbation of the dusty gas is 0.5 mm. The same domain size (16×1 cm) and grid resolution (1024×64) of the first study are used here. The incident Mach number is 1.2 as well, and the domain is filled with air only. The amplitude of the perturbed particle cloud is defined as half of the length of the dispersion in the x -direction of the particles that are initially placed in the front row. Five different particle sizes with four different mass loadings are studied, and Table 13 summarizes the parameters and the results of each case. Here, the multiphase RMI growth model and numerical predictions are compared.

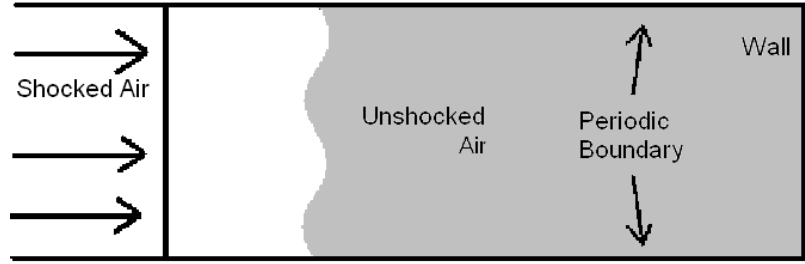


Figure 29: Initial configuration of RMI of the perturbed shape particle clouds. The grey region denotes the region filled with the gas-particle mixture.

In order to ascertain the choice of the number of parcels to represent the particle cloud for the simulations, three different parcel distributions are simulated for Case P0.5-1 and presented in Fig. 30. The case with 64 parcels slightly overpredicts the growth at late times whereas 128 and 256 parcel cases show very good agreement. Thus, 128 parcels in the y -directions are used for the rest of this section.

Figure 31 compares the evolution of the perturbation of a particle cloud for different Stokes numbers, for the cases P-0.5-4 and P2.0-4. For Case P0.5-4, narrow

Table 13: Parameters and results of each case for the second kind of multiphase RMI. The results of Case P4.0-X and P8.0-X are not listed because the acceleration of the particles for these cases is not impulsive due to the high inertia of the particles, and ΔV could not be determined for the same reason.

Case	r_p (μm)	f_2	τ_2 (s)	ΔV	$v_{0,num}$	A_m	$v_{0,m}$	$\frac{v_{0,num}}{v_{0,m}}$	St_2
P0.5-1	0.5	0.86	2.05×10^{-6}	88	5.81	0.30	6.71	0.84	2.90×10^{-2}
P0.5-2	0.5	1.77	2.05×10^{-6}	78	8.13	0.46	9.21	0.80	3.78×10^{-2}
P0.5-3	0.5	4.37	2.05×10^{-6}	62	9.44	0.68	10.84	0.75	4.13×10^{-2}
P0.5-4	0.5	8.73	2.05×10^{-6}	50	9.85	0.81	10.41	0.79	4.18×10^{-2}
P1.0-1	1.0	0.69	8.22×10^{-6}	90	4.77	0.25	5.82	0.80	9.52×10^{-2}
P1.0-2	1.0	1.41	8.22×10^{-6}	81	6.98	0.40	8.36	0.79	0.134
P1.0-3	1.0	3.47	8.22×10^{-6}	66	9.44	0.63	10.65	0.79	0.172
P1.0-4	1.0	6.94	8.22×10^{-6}	53.5	10.02	0.77	10.61	0.81	0.175
P2.0-1	2.0	0.56	3.28×10^{-5}	92	3.1	0.21	5.03	0.62	0.253
P2.0-2	2.0	1.12	3.28×10^{-5}	84	4.75	0.35	7.52	0.63	0.388
P2.0-3	2.0	2.78	3.28×10^{-5}	70	7.59	0.57	10.32	0.74	0.621
P2.0-4	2.0	5.55	3.28×10^{-5}	57.5	9.08	0.73	10.78	0.84	0.743
P4.0-1	4.0	0.35	1.31×10^{-4}						
P4.0-2	4.0	0.89	1.31×10^{-4}						
P4.0-3	4.0	2.31	1.31×10^{-4}						
P4.0-4	4.0	4.47	1.31×10^{-4}						
P8.0-1	8.0	1.03	5.26×10^{-4}						
P8.0-2	8.0	2.04	5.26×10^{-4}						
P8.0-3	8.0	2.94	5.26×10^{-4}						
P8.0-4	8.0	3.82	5.26×10^{-4}						

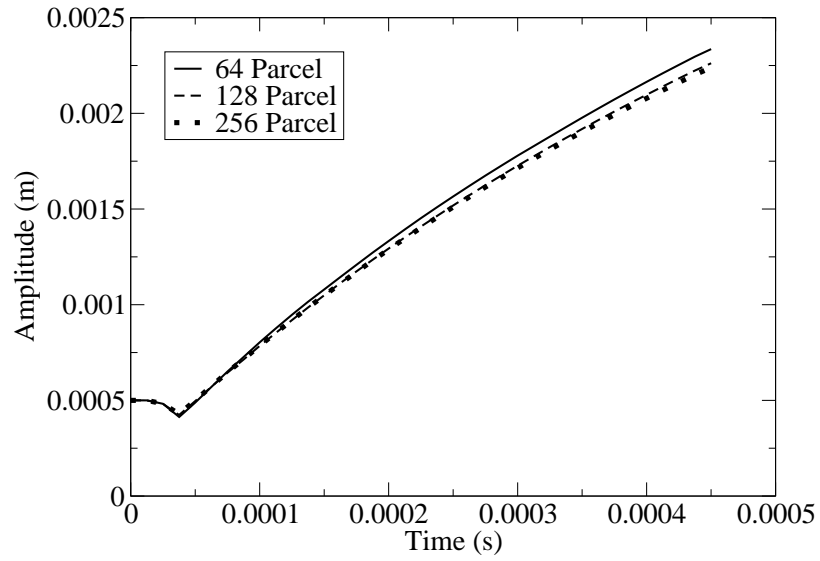


Figure 30: Comparison of the effect of number of parcels to the amplitude growth for the second kind of RMI under study for Case P0.5-1. In the legend, ‘64 Parcel’, ‘128 Parcel’ and ‘256 Parcel’ denote the number of parcels used in the y -direction, respectively, with the corresponding inter-parcel distance applied also in the x -direction.

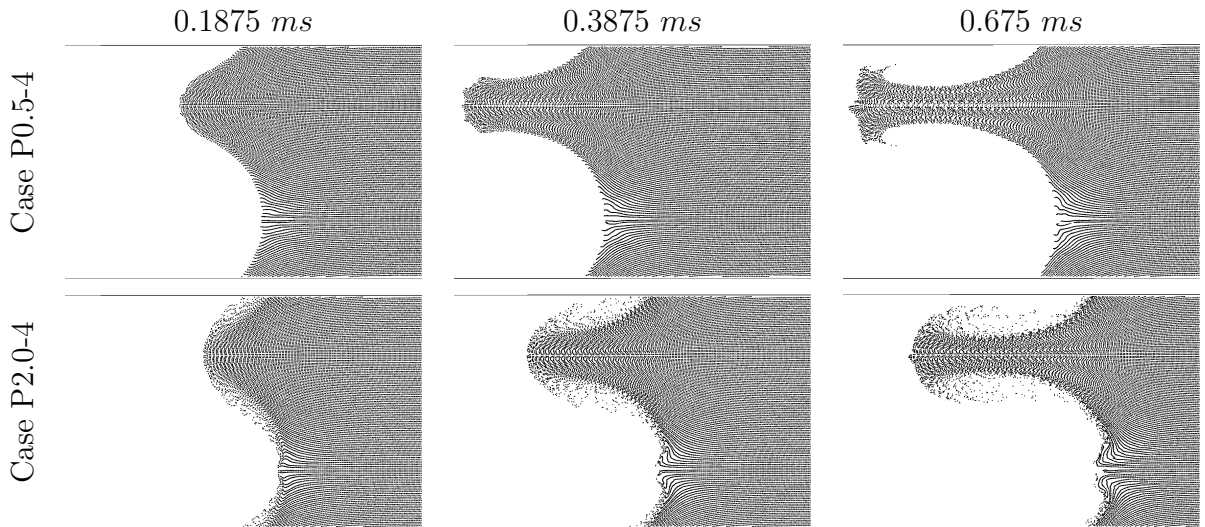


Figure 31: Growth of particle perturbation at different times for the second kind of RMI.

spikes are observed and the particles undergo less transverse dispersion *vis-à-vis* the P2.0-4 case; due to this, the particle cloud interfaces are sharper for P0.5-4. However, Case P2.0-4 shows wider spikes that result in the dispersion of particles around the spike at late times, clearly demonstrating that different particle dispersion is due to differences in the Stokes number. As Uchiyama & Yagami [90] pointed out, when a vortex ring interacts with a particle cloud, it can cause particles to move outside the vortex ring due to a centrifugal force, as a result, the particles are distributed over a wider region around the vortex ring. However, the Stokes number for the particles in Case P0.5-4 is very small, $St \approx 0.04$, due to which the particles follow the fluid motion rather than being dispersed by the vortex rings.

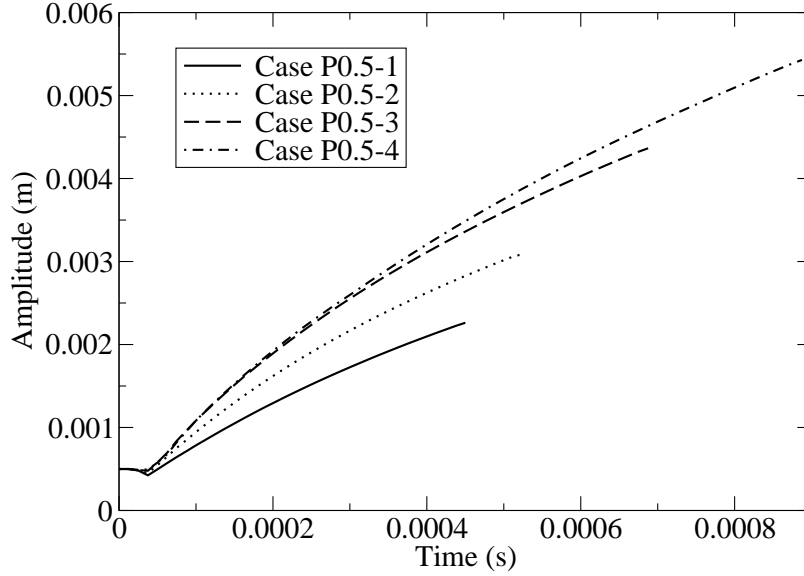


Figure 32: Amplitude growth of perturbed shape particle clouds with different initial particle mass loading for Case P0.5- X ($X = 1, 2, 3$ & 4).

The numerical prediction of the growth rate of small particles cases (Case P0.5- X & Case P1.0- X) are close to the multiphase RMI model ($v_{0,num}/v_{0,m} \approx 0.8$) as seen in the previous section (Table 11). The growth of the dusty gas perturbation is shown in Fig. 32; unlike the earlier result, the cases corresponding to a higher mass loading tend to have higher growth rates since it generates a higher A_m . However, a higher

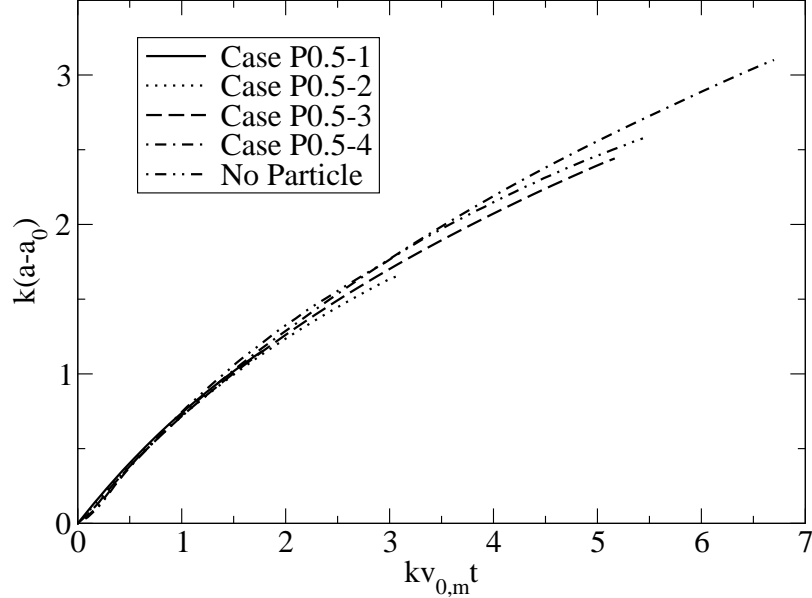


Figure 33: Normalized amplitude of perturbed shape particle clouds for Cases P0.5-X ($X = 1, 2, 3$ & 4).

mass loading leads to slower ΔV , and therefore results in smaller $v_{0,m}$. In fact, from Table 13, the model prediction of $v_{0,m}$ in Case P0.5-3 is larger than Case P0.5-4 even though the numerical results are opposite. The normalized growth rates indicate that the growth of the dusty gas perturbation is even comparable to the single-phase RMI, especially up to $kv_0t < 2.0$, as presented in Fig. 33. Thus, the results indicate that the dispersion of perturbed shape particle clouds can be explained by multiphase RMI growth models, even though it is hitherto not treated as a RMI problem in literature.

However, the growth of the perturbation follows RMI only for small St . If larger particles are used, they rather experience continuous acceleration until the particles and the gas attain equilibrium (in terms of velocity). Therefore, the amplitude growth rate of the heavier particle accelerates in the initial stage as presented in Fig. 34, and shows exponential growth instead of linear growth as seen in the Rayleigh-Taylor instability at early times [64].

In summary, the amplitude growth of perturbed shape particle cloud in air is investigated for a range of conditions by using numerical simulations and compared

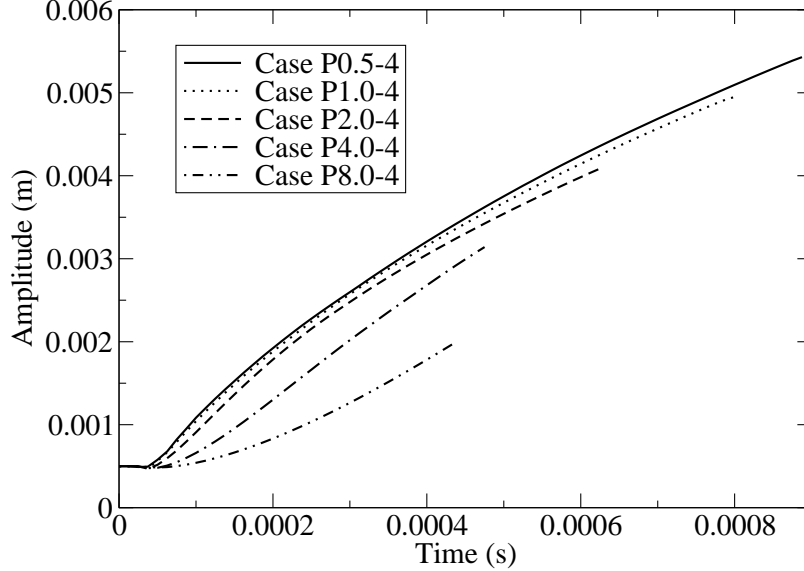


Figure 34: Changes in the behavior of the amplitude growth for different particle sizes.

with the developed multiphase RMI model. The results show that the growth rates of the simulations are predicted well by the multiphase RMI growth model, and the normalized amplitude growth rates are in accordance with the gas phase RMI. Therefore, this study suggests that dilute particle cloud dispersion by a shock wave can be treated as a RMI as long as the particle response time is small. However, if the particle response time is large, the particles experience continuous acceleration, and the growth of the interface shows exponential growth similar to RTI.

5.3 Conclusions of Multiphase RMI studies

This section derives the growth model of multiphase RMI by using dusty-gas assumptions, and analyzes two kinds of Richtmyer-Meshkov instabilities (RMI) in gas-particle mixtures. For a RMI involving an air/ SF_6 interface surrounded by a uniformly distributed particle cloud, it is found that the multiphase RMI model predicts the numerical simulation growth rates better than the original RMI model when the particle response time, $St < 10.0$. However, when the particle response time is larger, the growth rates follow the original Richtmyer's model since the particles do not follow

the fluid motion and the RMI process is entirely based on the gas phase. When the Stokes number is on the order of unity, preferential concentration of particles is found. However, when the Stokes number is small ($St \approx 0.04$), relatively uniform particle distribution is observed including in the high vorticity region. For large Stokes number ($St \approx 880$), on the other hand, the particles are not influenced by the fluid motion. The second type of multiphase RMI involves the multiphase growth of the perturbed particle cloud by a shock wave. Here, too, the multiphase RMI growth model shows good agreement with the numerical results, and the normalized growth rate of each case corresponds to the single-phase RMI even at late times. However, requirements on the particle response time is stricter, and the impulsive acceleration is found only when $St \ll 1.0$. If the particles response time is large, particles experience continuous acceleration after the shock, which results in an RTI-like exponential growth rate at early times.

CHAPTER VI

CONCLUSIONS AND RECOMMENDATIONS

6.1 Conclusion

The main purpose of this thesis is to study the growth rate of RMI with non-classical initial conditions. Two objectives are addressed and identified earlier in Sec. 1.3.

To meet the first objective, four different types of air/ SF_6 interface shapes are investigated in a shock tube configuration, and the predicted post-reshock growth rates are compared with available empirical models of Mikaelian's [62] and Charakhch'an's [14]. The simulation of 3D multi-mode RMI shows good agreement with a past experimental study, but other interface types (2D single-mode, 2D multi-mode and 3D single-mode) result in different growth rates after reshock. Parametric studies are therefore performed to investigate the sensitivities of the post-reshock growth rates to model the empirical parameters. For single-mode RMI configurations, the interface shape is found to be only a weak function of the post-reshock growth rate, as also predicted by previous reshock models. The post-reshock growth rate shows a linear correlation to the velocity jump due to reshock; however, it is only about a quarter of the prediction of Charakhch'an's model even though the growth before reshock compares well with pre-reshock models. The 3D single-mode post-reshock RMI growth rate is nearly 1.6 times larger than the 2D single-mode RMI. The parametric studies of multi-mode RMI show two distinctly different growth rates depending on the mixing conditions at reshock. If the interface remains sharp at the time of reshock, the post-reshock growth rate is as large as the single-mode cases. However, if the interface is mixed due to non-linear interactions of bubbles and spikes, the growth rates becomes slow and independent of the interface shapes. Thus, this study provides

new insights into the flow features of reshocked RMI for different initial perturbation types.

The second half of study derives the analytical growth model of multiphase RMI and compares it against the numerical predictions in order to meet the second objective. The linear amplitude growth of multiphase RMI is derived by applying past dusty-gas formulations assuming Stokes number, $St \ll 1.0$, and it is shown that the problem can be characterized by a mass fraction, f and St . The model is tested and compared with numerical predictions under two circumstances, i.e., a shock wave hitting (1) a perturbed species interface of air and SF_6 surrounded by uniformly distributed particles, and (2) a perturbed shape particle cloud in uniform air. In the first type, the interactions between the instabilities of the species perturbation and the particles are investigated. The multiphase growth model accurately predicts the growth rates when $St \ll 1.0$, and the amplitude growth normalized by the multiphase RMI velocity shows good agreement with the single-phase RMI growth rate as well. Furthermore, the multiphase model is in accordance with the growth rates obtained from the simulations even for cases corresponding to $St \approx 10$. Thus, it is shown that the multiphase is surely applicable for $St \ll 1.0$ and valid to relatively large Stokes number ($St \approx 10$) as well. When $St \gg 10$, particles do not follow the RMI motion, so that the RMI growth is only based on the fluid dynamics, and the growth rates agree with the original Richtmyer's model [79]. Preferential concentration of particles are observed around the RMI roll-ups at late times when St is of order unity, whereas when $St \ll 1.0$, the particles respond rapidly to the flow, causing them to distribute within the roll-ups; and particles hardly respond to the RMI motion if $St \gg 1.0$.

In the second problem, the multiphase RMI growth model is extended to study whether a perturbed dusty gas front shows RMI-like growth due to a shock wave. When $St \ll 1.0$, good agreement with the multiphase model is again seen. Moreover, the normalized growth rates are very close to the single-phase RMI growth even at late

times, so that the multiphase growth model is successfully applicable to the perturbed shape particle clouds as well. However, the requirement of Stokes number is more stringent than the first study since particles themselves characterize the interface. When St is close to unity, the particles do not experience impulsive acceleration but rather a continuous one, which results in exponential growth rates as seen in a Rayleigh-Taylor instability.

6.2 Recommendations for future work

This thesis provides basic understandings of the growth rate of reshocked RMI and multiphase RMI. However, the analysis of the physics involved is still in infancy and more investigations are recommended for future studies. The key recommendations for the future work are summarized here:

- The post-reshock growth rates depend on the interface conditions, and the different coefficients for the model are found. However, these coefficients are from the numerical and experimental studies, and no theoretical model has developed yet. Thus, it is important to establish theoretical understandings of how the dimension and interface shapes influence the post-reshock growth rates.
- The multiphase RMI growth model is first derived in this study, but it is still primitive and theoretical analysis towards more general model that deals with large St is necessary. Also, the theory should be extended to late times where the growth rate becomes non-linear. In addition, particle interactions with 3D RMI should be analyzed.
- The multiphase RMI under complex interface shapes should be studied. For example, multi-mode RMI generates bubbles and spikes with different Stokes number, so the particle concentration will be more complex. Also, since 3D RMI causes the vortex-rings, the particle distribution becomes different from 2D RMI.

- Reshock studies performed in the present work can be extended for the multiphase RMI as well. It would be interesting to study multiphase RMI with reshock since the particle distributions around RMI structures are non-uniform.
- The present study mainly focus on the large scale structures (e.g. perturbation growth), but the small scales generated by RMI is also important. RMI-induced turbulence has been studied recently, but it is not known whether it follows the classical Kolmogorov turbulence or not. Further numerical and theoretical investigations are necessary.

REFERENCES

- [1] ALON, U., HECHT, J., OFER, D., MULAMEL, D., and SHVARTS, D., “Scale invariant mixing rates of hydrodynamically unstable interface,” *Physical Review Letters*, vol. 72, no. 18, pp. 2867–2870, 1994.
- [2] ALON, U., HECHT, J., OFER, D., and SHVARTS, D., “Power laws and similarity of Rayleigh-Taylor and Richtmyer-Meshkov mixing fronts at all density ratio,” *Physical Review Letters*, vol. 74, no. 4, pp. 534–537, 1995.
- [3] ANDRONOV, V. A., BAKHRAKH, S. M., MESHKOV, E. E., MOKHOV, V. N., PEVNITSKII, V. V., and TOLSHMYAKOV, A. I., “Turbulent mixing at contact surface accelerated by shock waves,” *Journal of Experimental and Theoretical Physics*, vol. 44, p. 424, 1976.
- [4] ARNETT, D., “The role of mixing in astrophysics,” *Astrophysical Journal Supplement Series*, vol. 127, pp. 213–217, 2000.
- [5] BALACHANDAR, S., “A scaling analysis for point-particle approaches to turbulent multiphase flow,” *International Journal of Multiphase Flow*, vol. 35, pp. 801–810, 2009.
- [6] BALAKRISHNAN, K., GÉNIN, F., NANCE, D., and MENON, S., “Numerical study of blast characteristics from detonation of homogeneous explosives,” *Shock Waves*, vol. 20, no. 2, pp. 147–162, 2010.
- [7] BALAKRISHNAN, K. and MENON, S., “On the role of ambient reactive particles in the mixing and afterburn behind explosive blast waves,” *Combustion Science and Technology*, vol. 182, pp. 186–214, 2010.
- [8] BANERJEE, A. and ANDREWS, M. J., “3d simulation to investigate initial condition effects on the growth of Rayleigh-Taylor mixing,” *International Journal of Heat and Mass Transfer*, vol. 52, pp. 3906–3917, 2009.
- [9] BARENBLATT, G. I., “Self-similar turbulence propagation from an instantaneous plane source,” in *Nonlinear Dynamics and Turbulence* (BARENBLATT, G. I., LOOSS, G., and JOSEPF, D. D., eds.), pp. 48–60, Boston: PITMAN, 1983.
- [10] BOIKO, V. M., KISELEV, V. P., KISELEV, S., PAPYRIN, A., POPLAVSKY, S. V., and FOMIN, V. M., “Shock wave interaction with a cloud of particles,” *Shock Waves*, vol. 7, pp. 275–285, 1997.
- [11] BROUILLETTE, M., “The Richtmyer-Meshkov instability,” *Annual Review of Fluid Mechanics*, vol. 34, pp. 445–468, 2002.

- [12] BROUILLETTE, M. and STURTEVANT, B., “Experiments on the Richtmyer-Meshkov instability: single-scale perturbations on a continuous interface,” *Journal of Fluid Mechanics*, vol. 263, pp. 271–292, 1994.
- [13] CHAPMAN, P. R. and JACOBS, J. M., “Experiments on the three-dimensional incompressible Richtmyer-Meshkov instability,” *Physics of Fluids*, vol. 18, no. 7, p. 074101, 2006.
- [14] CHARAKHCH’YAN, A. A., “Richtmyer-Meshkov instability of an interface between two media due to passage of two successive shocks,” *Journal of Applied Mechanics and Technical Physics*, vol. 41, pp. 23–31, 2000.
- [15] CHARAKHCH’YAN, A. A., “Reshocking at the non-linear stage of Richtmyer-Meshkov instability,” *Plasma Physics and Control and Fusion*, vol. 43, pp. 1169–1179, 2001.
- [16] CLARK, T. T. and ZHOU, Y., “Growth rate exponents of Richtmyer-Meshkov mixing layers,” *Journal of Applied Mechanics*, vol. 73, pp. 461–468, 2006.
- [17] COHEN, R. C., DANNEVIK, W. P., DIMITS, A. M., ELIASON, D. E., MIRIN, A. A., ZHOU, Y., PORTER, D. H., and WOODWARD, P. R., “Three-dimensional simulation of a Richtmyer-Meshkov instability with a two-scale initial perturbation,” *Physics of Fluids*, vol. 14, no. 10, pp. 3692–3709, 2002.
- [18] COLELLA, P. and WOODWARD, P., “The piecewise-parabolic method for hydrodynamics,” *Journal of Computational Physics*, vol. 54, pp. 174–201, 1984.
- [19] COLLINS, B. D. and JACOBS, J. M., “PLIF flow visualization and measurements of the Richtmyer-Meshkov instability of an air/SF₆ interface,” *Journal of Fluid Mechanics*, vol. 464, pp. 113–136, 2002.
- [20] CROWE, C., SOMMERFELD, M., and TSUJI, Y., *Multiphase flows with droplets and particles*. CRC Press, 1998.
- [21] CUZZI, J. N., HOGAN, R. C., PAQUE, J. M., and DOBROVOLSKIS, A. R., “Size-selective concentration of chondrules and other small particles in protoplanetary nebula turbulence,” *The Astrophysical Journal*, vol. 546, pp. 496–508, 2001.
- [22] DIMONTE, G., “Nonlinear evolution of the Rayleigh-Taylor and Richtmyer-Meshkov instabilities,” *Physics of Plasma*, vol. 6, no. 5, pp. 2009–2015, 1999.
- [23] DRAZIN, P. G., *Introduction to Hydrodynamic Stability*. Cambridge Texts Applied Mathematics, 2002.
- [24] EINFELDT, B., “On Godunov-type methods for gas dynamics,” *SIAM Journal on Numerical Analysis*, vol. 25, no. 2, pp. 294–318, 1988.

- [25] EINFELDT, B., MUNZ, C. D., ROE, P. L., and SJOGREEN, B., “On Godunov-type methods near low densities,” *Journal of Computational Physics*, vol. 92, pp. 273–295, 1991.
- [26] EREZ, L., SADOT, O., ORON, D., EREZ, G., LEVIN, L. A., SHVARTS, D., and BEN-DOR, G., “Study of the membrane effect on turbulent mixing measurements in shock tubes,” *Shock Waves*, vol. 10, pp. 241–251, 2000.
- [27] FAETH, G., “Mixing transport and combustion in sprays,” *Progress in energy and combustion science*, vol. 13, pp. 293–345, 1987.
- [28] FESSLER, J. R., KULICK, J. D., and EATON, J. K., “Preferential concentration of heavy particles in a turbulent channel flow,” *Physics of Fluids*, vol. 6, no. 11, 1994.
- [29] FRYXELL, B. and MENON, S., “Simulation of turbulent flows containing strong shocks,” *Physica Scripta*, vol. T132, no. 014047, 2008.
- [30] GÉNIN, F., *Study of Compressible Turbulent Flows in Supersonic Environment by Large-Eddy Simulation*. PhD thesis, Georgia Institute of Technology, Jan. 2009.
- [31] GÉNIN, F. and MENON, S., “Simulation of turbulent mixing behind a strut injector in supersonic flow,” in *AIAA-2009-0132, 47th AIAA Aerospace Sciences Meeting*, (Orlando, FL), Jan. 2009.
- [32] GÉNIN, F. and MENON, S., “Dynamics of sonic jet injection into supersonic crossflow,” *Journal of Turbulence*, vol. 11, no. 4, pp. 1–30, 2010.
- [33] GÉNIN, F. and MENON, S., “Simulation of turbulent mixing behind a strut injector in supersonic flow,” *AIAA Journal*, vol. 48, no. 3, pp. 526–539, 2010.
- [34] GÉNIN, F. and MENON, S., “Studies of shock/turbulent shear layer interaction using Large-Eddy Simulation,” *Computers & Fluids*, vol. 39, no. 5, pp. 800–819, 2010.
- [35] GONCHAROV, V. N., “Analytical model of nonlinear, single-mode, classical Rayleigh-Taylor instability at arbitrary atwood number,” *Physical review letters*, vol. 88, no. 134502, 2002.
- [36] GOTTLIEB, D. and TURKEL, E., “Dissipative two-four methods for time-dependent problems,” *Mathematics of Computation*, vol. 30, no. 136, pp. 703–723, 1976.
- [37] GOWARDHAN, A. A., GRISTEIN, F. F., and WACTOR, A., “Three dimensional simulations of Richtmyer-Meshkov instability in shock-tube experiments,” in *AIAA-2010, 48th AIAA Aerospace Sciences Meeting*, (Orlando, FL), Jan. 2010.

- [38] HARTEN, A., LAX, P. D., and VAN LEER, B., “On upstream differencing and Godunov-type schemes for hyperbolic conservation laws,” *SIAM Review*, vol. 25, pp. 35–61, 1983.
- [39] HECHT, J., ALON, U., and SHVARTS, D., “Potential flow models of Rayleigh-Taylor and Richtmyer-Meshkov bubble fronts,” *Physics of Fluids*, vol. 6, no. 12, 1994.
- [40] HILL, D. J., PANTANO, C., and PULLIN, D. I., “Large-eddy simulation and multiscale modeling of Richtmyer-Meshkov instability with reshock,” *Journal of Fluid Mechanics*, vol. 557, pp. 29–61, 2006.
- [41] HOUAS, L. and CHEMOUNI, I., “Experimental investigation of Richtmyer-Meshkov instability in shock tube,” *Physics of Fluids*, vol. 8, no. 2, 1996.
- [42] JACOBS, J. M. and KRIVETS, V., “Experiments on the late-time development of single-mode Richtmyer-Meshkov instability,” *Physics of Fluids*, vol. 17, no. 3, p. 034105, 2005.
- [43] KISELEV, S., VOROZHTSOV, E. V., and FOMIN, V. M., *Foundations of Fluid Mechanics with Applications*. Birkhäuser, 1999.
- [44] KISELEV, V., KISELEV, S., and VOROZHTSOV, E., “Interaction of a shock wave with a particle cloud of finite size,” *Shock Waves*, vol. 16, pp. 53–64, 2006.
- [45] LATINI, M., SCHILLING, O., and DON, W. S., “Effects of WENO flux reconstruction order and spatial resolution on reshocked two-dimensional Richtmyer-Meshkov instability,” *Journal of Computational Physics*, vol. 221, pp. 805–836, 2007.
- [46] LATINI, M., SCHILLING, O., and DON, W. S., “High-resolution simulations and modeling of reshocked single-mode Richtmyer-Meshkov instability: Comparison to experimental data and to amplitude growth model predictions,” *Physics of Fluids*, vol. 19, no. 2, p. 024104, 2007.
- [47] LAYZER, D., “On the instability of superposed fluids in a gravitational field,” *The Astrophysical Journal*, vol. 122, no. 1, 1955.
- [48] LEINOV, E., MALAMUD, G., ELBAZ, Y., LEVIN, L. A., BEN-DOR, G., SHVARTS, D., and SADOT, O., “Experimental and numerical investigation of the Richtmyer-Meshkov instability under re-shock conditions,” *Journal of Fluid Mechanics*, vol. 626, pp. 449–475, 2009.
- [49] LEVEQUE, R. J., *Finite Volume Methods for Hyperbolic Problems*. Cambridge University Press, 2002.
- [50] LINDL, J. D., MCCRORY, R. L., and CAMPBELL, E. M., “Progress toward ignition and burn propagation in inertial confinement fusion,” *Physics Today*, vol. 45, pp. 32–40, 1992.

- [51] LING, W., CHUNG, J. N., TROUTT, T. R., and CROWE, C. T., “Direct numerical simulation of a three-dimensional temporal mixing layer with particle dispersion,” *Journal of Fluid Mechanics*, vol. 358, pp. 61–85, 1998.
- [52] LOMBARDINI, M. and PULLIN, D. I., “Small-amplitude perturbations in the three-dimensional cylindrical Richtmyer-Meshkov instability,” *Physics of Fluids*, vol. 21, p. 114103, 2009.
- [53] LONG, C. C., KRIVETS, V. V., GREENOUGH, J. A., and JACOBS, J. W., “Shock tube experiments and numerical simulation of the single-mode, three-dimensional Richtmyer-Meshkov instability,” *Physics of Fluids*, vol. 21, no. 11, p. 114104, 2009.
- [54] LOTH, E., “Numerical approaches for motion of dispersed particles, droplets and bubbles,” *Progress in energy and combustion science*, vol. 26, pp. 161–223, 2000.
- [55] MATSUOKA, C., NISHIHARA, K., and FUKUDA, Y., “Nonlinear evolution of an interface in Richtmyer-Meshkov instability,” *Physical Review E*, vol. 67, no. 036301, 2003.
- [56] MAXEY, M. R. and RILEY, J. J., “Equation of motion for a small rigid sphere in a nonuniform flow,” *Physics of Fluids*, vol. 26, no. 4, pp. 883–889, 1983.
- [57] MENON, S. and PATEL, N., “Subgrid modeling for simulation of spray combustion in large-scale combustors,” *AIAA JOURNAL*, vol. 44, pp. 709–723, 2006.
- [58] MESHKOV, J. D., “Instability of the interface of two gases accelerated by shock wave,” *Fluid Dynamics*, vol. 4, pp. 101–104, 1969.
- [59] MICHAEL, D. H., “The stability of plane Poiseuille flow of a dusty gas,” *Journal of Fluid Mechanics*, vol. 18, pp. 19–32, 1964.
- [60] MICHAEL, D. H., “Kelvin-Helmholtz instability of a dusty gas,” *Proc. Camb. Phil. Soc.*, vol. 61, pp. 569–571, 1965.
- [61] MIKAELIAN, K. O., “Richtmyer-Meshkov instabilities in stratified fluids,” *Physical Review A*, vol. 31, no. 1, pp. 410–419, 1985.
- [62] MIKAELIAN, K. O., “Turbulent mixing generated by Rayleigh-Taylor and Richtmyer-Meshkov instabilities,” *Physical Review A*, vol. 36, no. 3, pp. 343–347, 1989.
- [63] MIKAELIAN, K. O., “Analytic approach to nonlinear Rayleigh-Taylor and Richtmyer-Meshkov instabilities,” *Physical Review Letters*, vol. 80, no. 3, pp. 508–511, 1998.
- [64] MIKAELIAN, K. O., “Explicit expressions for the evolution of single mode Rayleigh-Taylor and Richtmyer-Meshkov instabilities at arbitrary atwood numbers,” *Physical Rev. E*, vol. 67, no. 026319, 2003.

- [65] MIKAELIAN, K. O., “Richtmyer-Meshkov instabilities of arbitrary shapes,” *Physical Rev. E*, vol. 17, no. 034101, 2005.
- [66] MÜGLER, C. and GAUTHIER, S., “Two-dimensional Navier-Stokes simulations of gaseous mixtures induced by Richtmyer-Meshkov instability,” *Physics of Fluids*, vol. 12, pp. 1783–1798, 2000.
- [67] NELSON, C. C., *Simulations of spatially evolving compressible turbulence using a local dynamic subgrid model*. PhD thesis, Georgia Institute of Technology, Atlanta, GA, December 1997.
- [68] NELSON, C. C. and MENON, S., “Unsteady simulations of compressible spatial mixing layers,” *AIAA paper 98-0786*, 1998.
- [69] NIEDERAUS, C. E. and JACOBS, J. M., “Experimental study of the Richtmyer-Meshkov instability of incompressible fluids,” *Journal of Fluid Mechanics*, vol. 485, pp. 243–277, 2003.
- [70] ORAN, E. S. and GAMEZO, V. N., “Origins of the deflagration-to-detonation transition in gas-phase combustion,” *Combustion and Flame*, vol. 148, pp. 4–47, 2007.
- [71] ORON, D., ARAZI, L., KARTOON, D., RIKANATI, A., ALON, U., and SHVARTS, D., “Dimensionality dependence of the Rayleigh-Taylor and Richtmyer Meshkov instability late-time scaling laws,” *Physics of Plasma*, vol. 8, no. 6, pp. 2883–2889, 2001.
- [72] OTA, O. A., BARTON, C. J., and HOLDER, D. A., “Shock tube experiment: half-height dense gas region,” *Physica Scripta*, vol. T132, no. 014015, 2008.
- [73] PAI, S. I., MENON, S., and FAN, Z. Q., “Similarity solutions of a strong shock wave propagation in a mixture of a gas and dusty particles,” *Int. J. Engng Sci.*, vol. 18, pp. 1365–1373, 1980.
- [74] PATANKAR, N. A. and JOSEPH, D. D., “Lagrangian numerical simulation of particle flows,” *International Journal of Multiphase Flow*, vol. 27, pp. 1685–1706, 2001.
- [75] POGGI, F., THOREMBEY, M. H., and RODRIGUEZ, G., “Velocity measurements in turbulent gaseous mixtures induced Richtmyer-Meshkov instability,” *Physics of Fluids*, vol. 10, no. 11, pp. 2698–2700, 1998.
- [76] POINSOT, T. and VEYNANTE, D., *Theoretical and Numerical Combustion*. Edwards, 2005.
- [77] POLING, B. E., PRAUSNITZ, J. M., and O’CONNELL, J. P., *The properties of gases and liquids*. McGraw-Hill, 2000.

- [78] READ, K. I., “Experimental investigation of turbulent mixing by Rayleigh-Taylor instability,” *Physica D*, vol. 12, pp. 45–58, 1984.
- [79] RICHTMYER, R. D., “Taylor instability in shock acceleration of compressible fluids,” *Communications on Pure and Applied Mathematics*, vol. 13, no. 297, 1960.
- [80] SADOT, O., EREZ, L., ALON, U., ORON, D., LEVIN, L. A., EREZ, G., and G. BEN-DOR, D. S., “Study of nonlinear evolution of single-mode and two-bubble interaction under Richtmyer-Meshkov instability,” *Physical Review Letters*, vol. 80, no. 8, pp. 1654–1657, 1998.
- [81] SAFFMAN, P. G., “On the stability of laminar flow of a dusty gas,” *Journal of Fluid Mechanics*, vol. 13, pp. 120–128, 1961.
- [82] SANKARAN, V., *Sub-grid Combustion Modeling for Compressible Two-Phase Reacting Flows*. PhD thesis, Georgia Institute of Technology, 2003.
- [83] SCHILLING, O. and LATINI, M., “High-order WENO simulations of three-dimensional reshocked Richtmyer-Meshkov instability to late times: Dynamics, dependence on initial conditions, and comparisons to experimental data,” *Acta Mathematica Scientia*, vol. 30B, no. 2, pp. 595–620, 2010.
- [84] SCHILLING, O., LATINI, M., and DON, W. S., “Physics of reshock and mixing in single-mode Richtmyer-Meshkov instability,” *Physical Review E*, vol. 76, no. 2, p. 026319, 2007.
- [85] SIMONIN, O., FÉVRIER, P., and LAVIÉVILLE, J., “On the spatial distribution of heavy-particle velocities in turbulent flow: from continuous field to particulate chaos,” *Journal of Turbulence*, vol. 3, no. 40, 2002.
- [86] SNIDER, D. M., “An incompressible three-dimensional multiphase particle-in-cell model for dense particle flows,” *Journal of Computational Physics*, vol. 170, pp. 523–549, 2001.
- [87] SOHN, S., “Simple potential-flow model of Rayleigh-Taylor and Richtmyer-Meshkov instabilities for all density ratio,” *Physical Review E*, vol. 67, no. 026301, 2003.
- [88] TAYLOR, G. I., “The instability of liquid surfaces when accelerated in a direction perpendicular to their plane. I,” *Proc. Roy Soc., J. Lond. ser. A*, vol. 201, no. 1065, 1950.
- [89] TORO, E. F., SPRUCE, M., and SPEARES, W., “Restoration of the contact surface in the HLL Riemann solver,” *Shock Waves*, vol. 4, pp. 25–34, 1994.
- [90] UCHIYAMA, T. and YAGAMI, H., “Numerical simulation for the collision between a vortex ring and solid particles,” *Powder Technology*, vol. 188, pp. 73–80, 2008.

- [91] UKAI, S., BALAKRISHNAN, K., and MENON, S., “Growth rate of single-mode Richtmyer-Meshkov instability with reshock,” *Submitted to Shock Waves*, 2010.
- [92] VANDENBOOMGAERDE, M., GAUTHIER, B., and MÜGLER, C., “Nonlinear regime of a multimode Richtmyer-Meshkov instability: A simplified perturbation theory,” *Physics of Fluids*, vol. 14, no. 3, 2002.
- [93] VETTER, M. and STURTEVANT, B., “Experiments on the Richtmyer-Meshkov instability,” *Shock Waves*, vol. 4, pp. 247–252, 1995.
- [94] WILKE, C. R., “A viscosity equation for gas mixtures,” *J. Chem. Phys.*, vol. 18, no. 4, pp. 517–519, 1950.
- [95] YANG, J., KUBOTA, T., and ZUKOSKI, E. E., “Applications of shock-induced mixing to supersonic combustion,” *AIAA Journal*, vol. 31, no. 5, pp. 854–862, 1993.
- [96] ZABUSKY, N. J., “Vortex paradigm for accelerated inhomogeneous flows: Visio-metrics for the Rayleigh-Taylor and Richtmyer-Meshkov environments,” *Annual Review of Fluid Mechanics*, vol. 31, pp. 495–536, 1999.
- [97] ZHANG, Q., “Analytical solutions of Layzer-type approach to unstable interfacial fluid mixing,” *Physics Review Letter*, vol. 81, no. 16, pp. 1106–1124, 1998.
- [98] ZHANG, Q. and SOHN, S., “Nonlinear theory of unstable fluid mixing driven by shock wave,” *Physics of Fluids*, vol. 9, pp. 1106–1124, 1996.